SUPERCONDUCTIVITY, INCLUDING HIGH-TEMPERATURE SUPERCONDUCTIVITY

Influence of a boron oxide admixture on the superconducting properties of the bismuth-containing 2212 phase

V. V. Zhgamadze,* N. G. Margiani, I. A. Mzhavanadze, N. G. Sabashvili, G. A. Tsintsadze, and G. A. Shurgaya

Institute of Cybernetics, Georgian Academy of Sciences, ul. S. Éuli 5, Tbilisi 380086, Georgia
(Submitted March 29, 2004; revised April 22, 2004)
Fiz. Nizk. Temp. **30**, 1247–1251 (December 2004)

The effect of an admixture of boron oxide B_2O_3 on the superconducting properties of the bismuth-containing 2212 phase is investigated. It is found that boron doping improves the superconducting transition characteristics of $Bi_2Sr_2Ca_1Cu_2O_y$ and $Bi_{1.8}Pb_{0.2}Sr_2Ca_1Cu_2O_y$ samples slowly cooled in a furnace. As the boron content in quenched samples of the 2212 phase increases, T_c and the relative volume of the superconducting fraction are observed to decrease monotonically. Boron doping of the 2212 phase decreases the lattice parameter c. © *2004 American Institute of Physics.* [DOI: 10.1063/1.1820031]

1. INTRODUCTION

The bismuth-containing superconducting system Bi–Sr–Ca–Cu–O, nominally pure or doped with different elements, can be regarded as a model system for investigating the appearance of a superconducting state in metal-oxide high-temperature superconductors (HTSCs). Three HTSC phases with the generalized formula $Bi_2Sr_2Ca_{n-1}Cu_nO_{2n+4}$, $n=1$, 2, and 3, have been observed and structurally identified in this system.[1–4] Investigators are especially interested in the low-temperature 2212 phase ($T_c \approx 80$ K) with $n=2$ and the 2223 phase with $n=3$, which has the highest superconducting (SC) transition temperature ($T_c \approx 110$ K). The formation and the superconducting properties of the 2223 and 2212 phases are very sensitive to any variations of the many conditions under which they are synthesized, the composition of the initial mixture, and the introduction of various admixtures into the system. This is due to, first and foremost, the complexity of the bismuth system, where intertransformations of the SC phases are observed in a quite narrow temperature range.[5–7]

There is an enormous literature on the influence of various impurity elements on the properties of bismuth-containing ceramic. An important physical-technical result is that the partial substitution of lead for bismuth stimulates the formation and increases the volume fraction of the high-temperature 2223 phase over a wide range of nominal compositions of the samples,[8] though it is impossible to eliminate completely the 2212 phase in the synthesized material. In Ref. 9 it is reported that the partial substitution of lithium and fluorine for copper and oxygen, respectively, in lithium fluoride doped samples of the 2212 phase increases the critical temperature and the relative volume of the SC fraction.

The influence of boron on phase formation and the SC properties of bismuth-containing ceramic has still not been investigated. Since the ionic radius of boron is small, boron can be introduced into the bismuth system as an admixture and not as an element which replaces the structural constituents of the samples of the 2223 and 2212 phases. In contrast to different variants of isomorphic substitutions in these phases, for example, yttrium or other rare-earth elements for calcium, resulting in the suppression of superconductivity,[10–12] it has not been ruled out that some boron ions occupy interstitial positions in the layered structures of bismuth-containing SC phases.

Our preliminary data[13] attest to a nonmonotonic dependence of the zero electric resistance temperature and the magnetic susceptibility on the boron content in samples of the high-temperature 2223 phase with the initial composition $Bi_{1.7}Pb_{0.3}Sr_2Ca_2Cu_4B_xO_y$ ($0 \leqslant x \leqslant 1$). The SC properties of boron-doped samples of the low-temperature 2212 phase are of no less interest.

In the present work the influence of a boron oxide admixture on the SC properties of the 2212 phase, including samples where lead is substituted for a portion of the bismuth (10 at.%), is investigated.

2. SAMPLES AND EXPERIMENTAL PROCEDURE

Ceramic samples with the nominal composition $Bi_2Sr_2Ca_1Cu_2B_xO_y$ and $Bi_{1.8}Pb_{0.2}Sr_2Ca_1Cu_2B_xO_y$, $x=0$, 0.25, 0.5, and 0.75, were synthesized in air, using the standard solid-phase technology, from the oxides and carbonates of the corresponding elements: Bi_2O_3, PbO, $SrCO_3$, $CaCO_3$, CuO, and B_2O_3. The powder was preannealed for 17 h at 810 °C. Tabletized samples were heat-treated for 15 h at 855–860 °C. After annealing was completed, the synthesized compositions were cooled from the synthesis temperature by two methods: 1) slow cooling in air with the electric furnace switched off and 2) rapid cooling (quenching) in liquid nitrogen. The resistivity ρ was measured on $\sim 0.5 \times 3 \times 9$ mm bars cut from the tablets. Silver paste was burned in to form electric contacts. The standard four-contact method was used to measure the temperature dependence $\rho(T)$. The lowest temperature at which the resistivity measurements were performed in a regime with evacuation of

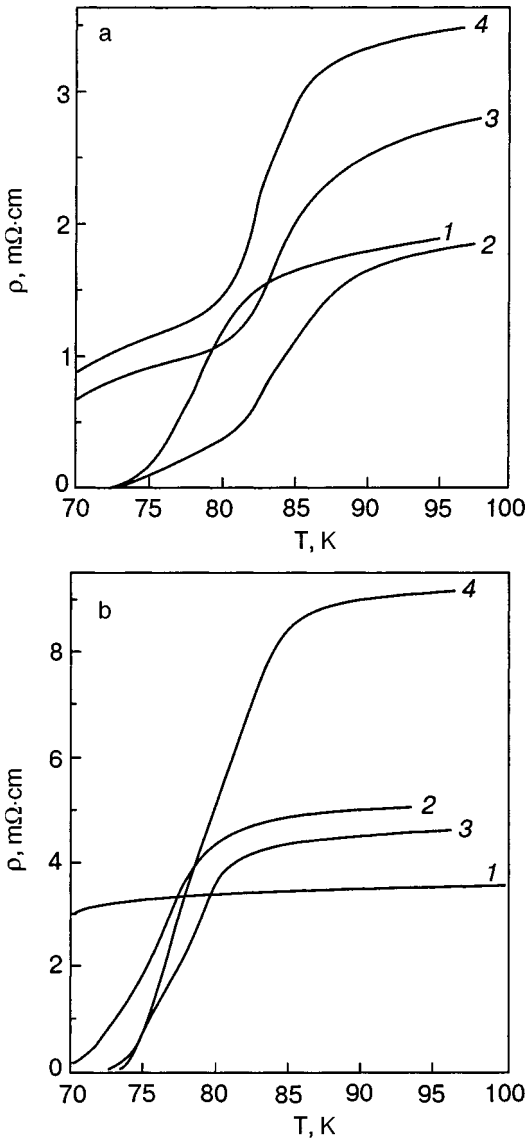

FIG. 1. $\rho(T)$ for slowly cooled $Bi_2Sr_2Ca_1Cu_2B_xO_y$ (a) and $Bi_{1.8}Pb_{0.2}Sr_2Ca_1Cu_2B_xO_y$ (b) samples with $x=0$ *(1)*, 0.25 *(2)*, 0.5 *(3)*, and 0.75 *(4)*.

nitrogen vapor was about 70 K. The inductive method was used to determine the temperature dependence of the magnetic susceptibility $\chi(T)$ of the quenched samples, and the SC transition temperature and the change in the content of the SC fraction in the samples were determined from the magnetic measurements. X-Ray phase analysis (XPA) was performed with a DRON-1,5 diffractometer (CuK_α radiation), and the unit-cell parameters of nominally-pure and boron-doped samples of the 2212 phase were determined.

3. RESULTS AND DISCUSSION

The XPA data show that most peaks in the diffraction patterns are due to the 2212 phase, which is the dominant phase for the measured compositions. Aside from the main 2212 phase, the impurity 2201 phase ($Bi_2Sr_2CuO_y$) with $T_c \approx 10$ K is present in the $Bi_2Sr_2Ca_1Cu_2B_xO_y$ and $Bi_{1.8}Pb_{0.2}Sr_2Ca_1Cu_2B_xO_y$ samples with $x>y$.

Figure 1a shows the temperature dependences of the resistivity $\rho(T)$ of slowly-cooled $Bi_2Sr_2Ca_1Cu_2B_xO_y$ ($0 \leqslant x \leqslant 0.75$) samples. It is evident that admixing B_2O_3 to the system substantially decreases the onset temperature T_c^{on} of the SC transition, determined by the point where the function $\rho(T)$ deviates from linearity. The end-point temperatures T_c^{off} of the SC transition in nominally-pure and doped ($x=0.25$) samples are 72 K. At the same time, for $x>0.25$ a long tail is observed in the curves $\rho(T)$ below 75 K. This tail is due to the presence of the impurity 2201 phase. Figure 1b shows the curves $\rho(T)$ for slowly-cooled $Bi_{1.8}Pb_{0.2}Sr_2Ca_1Cu_2B_xO_y$ ($0 \leqslant x \leqslant 0.75$) samples in which lead was substituted for a portion of the bismuth. The deviation of the function $\rho(T)$ from linearity for a boron-free sample starts only at ~ 75 K. As shown in Ref. 14, the Pb-doped 2212 sample is characterized by zero-resistivity temperature $T_c^{off} \simeq 60$ K. According to published data[6,15,16] the bismuth-containing 2212 phase, synthesized and slowly cooled in air or oxygen, possesses superstoichiometric oxygen, i.e. extra holes. It is natural to suppose that the partial heterovalent substitution of divalent Pb^{2+} for trivalent Bi^{3+} in Bi–O layers further increases the number of extra charge carriers and degrades the SC properties of the Pb-containing 2212 phase. In Fig. 1b it is evident that admixing B_2O_3 sharply improves the characteristics of the SC transition of slowly cooled 2212 samples containing lead. Thus $T_c^{off}=73$ K at $x=0.25$, though at higher boron concentrations residual resistivity appears at 70 K as a result of the presence of the impurity 2201 phase in the sample with $x=75$. The observed improvement in the SC characteristics of slowly-cooled boron-doped samples from both concentration series could be due to, among other factors, filling of some extra holes by additional electrons from trivalent boron.

Figure 2a displays the curves $\rho(T)$ for quenched $Bi_2Sr_2Ca_1Cu_2B_xO_y$ samples. The value of T_c^{off} for the nominally pure sample increases to 83 K and the value of T_c^{on} to 100 K. Quenching in liquid nitrogen has virtually no effect on the SC transition in the sample with $x=0.25$, while at a higher boron content $x=0.75$ semiconductor behavior of $\rho(T)$ with substantial residual resistivity at 70 K is observed. As noted in Ref. 17, the properties of the 2201 phase are more sensitive to the oxygen content as compared with the 2212 phase and semiconductor conductivity is observed after quenching. On the basis of these data the semiconductor behavior and the high resistivity can be explained by the presence of the impurity 2201 phase in the 2212 sample with boron content $x=0.75$. The temperature dependences $\rho(T)$ for quenched $Bi_{1.8}Pb_{0.2}Sr_2Ca_1Cu_2B_xO_y$ ($0 \leqslant x \leqslant 0.75$) samples are shown in Fig. 2b. It is evident that quenching the sample with $x=0$ increases the value of T_c^{off} sharply to 90 K and appreciably narrows the width of the resistance transition. The characteristics of the SC transition for $x=0.25$ and 0.5 are less sensitive to the cooling regime: the zero-resistivity temperature for these samples increases from 78 and 74 K, respectively. For a still higher boron content $x=0.75$ the temperature dependence $\rho(T)$ acquires the semiconductor character observed for the same impurity concentration in the lead-free sample. Evidently, quenching in liquid nitrogen optimizes the hole concentration for the superconductivity mechanism by decreasing the oxygen content in the samples from both series (with and without lead) with $x<0.75$. Comparing the curves $\rho(T)$ gives a basis for con-

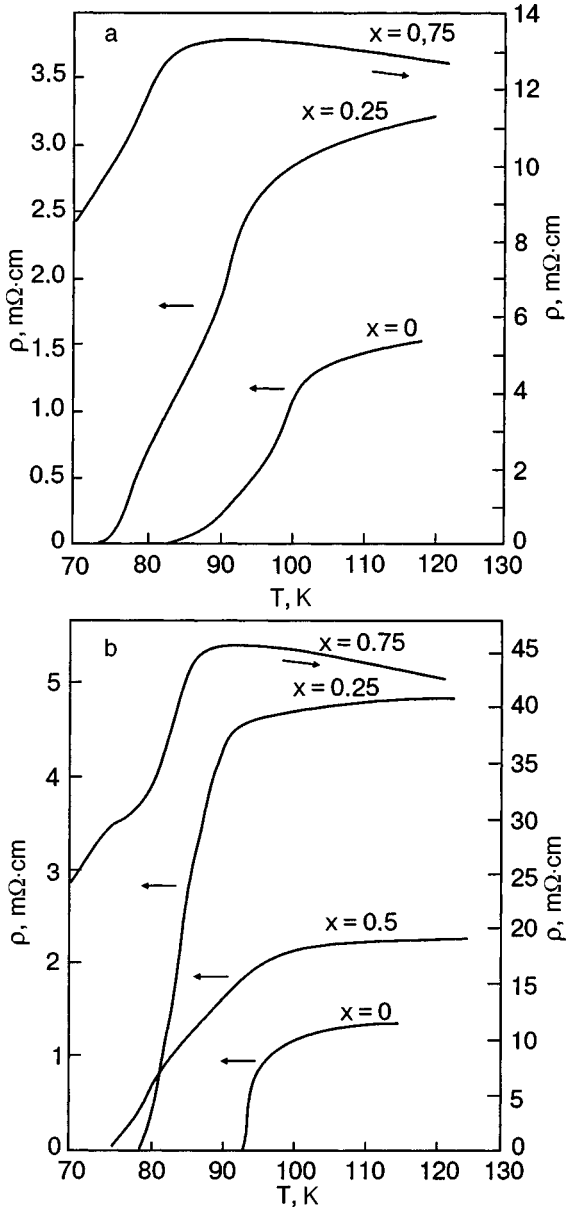

FIG. 2. $\rho(T)$ for quenched $Bi_2Sr_2Ca_1Cu_2B_xO_y$ (a) and $Bi_{1.8}Pb_{0.2}Sr_2Ca_1Cu_2B_xO_y$ samples (b).

cluding that the quenched $Bi_{1.8}Pb_{0.2}Sr_2Ca_1Cu_2B_xO_y$ samples with boron concentration ranging from $x=0$ to 0.25 possess the best SC transition characteristics. The increase of T_c^{off} and decrease of the SC transition width for quenched $Bi_{1.8}Pb_{0.2}Sr_2Ca_1Cu_2B_xO_y$ ($x=0$ and 0.25) samples as compared with the same parameters of $Bi_2Sr_2Ca_1Cu_2B_xO_y$ ($x=0$ and 0.25) samples could be due to various factors. As noted in Ref. 18, the lead-free 2212 phase possesses a substantially larger number of stacking faults (intergrowths of the 2201 phase, which ordinary phase analysis does not show) than in the case where lead is substituted for some of the bismuth. Improvement of intergrain bonds as a result of introducing lead into the 2212 phase, as supposed in Ref. 19 for the 2223 phase, has also not been ruled out.

The temperature dependences $\chi(T)$, presented in Fig. 3, for quenched 2212 phase samples agree with the resistivity measurements. It is evident that the relative content of the SC fraction is highest in $Bi_{1.8}Pb_{0.2}Sr_2Ca_1Cu_2B_xO_y$ and de-

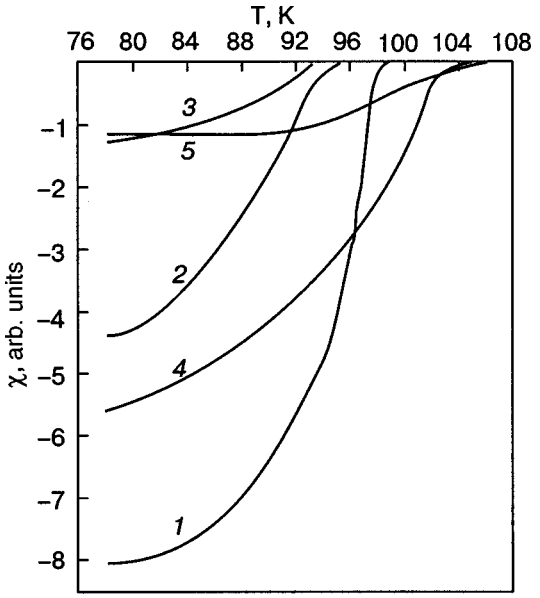

FIG. 3. $\rho(T)$ for quenched $Bi_{1.8}Pb_{0.2}Sr_2Ca_1Cu_2B_xO_y$ samples with $x=0$ (1), 0.25 (2), and 0.5 (3) and $Bi_2Sr_2Ca_1Cu_2B_xO_y$ samples with $x=0$ (4) and 0.25 (5).

creases sharply in both series when B_2O_3 is introduced into the SC system. The unit-cell parameters of the 2212 phase are given in Table I. The decrease in the parameter c in the boron oxide doped samples can be tentatively attributed to boron ions occupying interstices in the lattice as a result of their smaller ionic radius, though the question of the structural role of boron requires further investigation. Interstitial cations are a donor impurity, decreasing the concentration of charge carriers (holes),[20] which if extra holes are present, improves the SC properties.

In summary, analyzing the curves $\rho(T)$ for the experimental samples it can be concluded that admixing B_2O_3 to the 2212 phase increases the onset temperature of the SC transition in a slowly cooled lead-free sample and results in the appearance of a SC transition with $T_c^{\text{off}}=73$ K in $Bi_{1.8}Pb_{0.2}Sr_2Ca_1Cu_2B_xO_y$ ($x=0.25$). Quenching in liquid nitrogen sharply improves the SC characteristics of the boron-free samples. At the same time a substantially smaller in-

TABLE I. The lattice parameters a and c of samples of the 2212 phase.

Nominal sample composition	x	a, Å	c, Å
$Bi_2Sr_2Ca_1Cu_2O_y$ (s)	0	5.40	30.83
$Bi_2Sr_2Ca_1Cu_2B_xO_y$ (s)	0.25	5.39	30.73
$Bi_2Sr_2Ca_1Cu_2B_xO_y$ (s)	0.75	5.40	30.69
$Bi_{1.8}Pb_{0.2}Sr_2Ca_1Cu_2O_y$ (s)	0	5.39	30.82
$Bi_{1.8}Pb_{0.2}Sr_2Ca_1Cu_2B_xO_y$ (s)	0.5	5.40	30.75
$Bi_2Sr_2Ca_1Cu_2O_y$ (q)	0	5.41	30.89
$Bi_2Sr_2Ca_1Cu_2B_xO_y$ (q)	0.25	5.41	30.85
$Bi_{1.8}Pb_{0.2}Sr_2Ca_1Cu_2O_y$ (q)	0	5.40	30.87
$Bi_{1.8}Pb_{0.2}Sr_2Ca_1Cu_2B_xO_y$ (q)	0.5	5.40	30.77

Note: (s)—slowly cooled samples; (q)—quenched samples

crease in T_c^{off} is observed in boron-doped samples with $x < 0.75$. Comparing the temperature dependences $\rho(T)$ and taking into account the decrease of the lattice parameter c with increasing boron content in the samples, it can be conjectured that boron ions occupy interstices in the lattice as a donor impurity. The degradation of the SC properties and the high resistivity in the normal state of boron-doped samples $Bi_2Sr_2Ca_1Cu_2B_xO_y$ and $Bi_{1.8}Pb_{0.2}Sr_2Ca_1Cu_2B_xO_y$ with $x > 0.25$ are explained by the appearance of the 2201 impurity phase, which gives rise to the semiconductor temperature dependence $\rho(T)$ in the quenched samples with $x = 0.75$.

*E-Mail: vakhtang7@rambler.ru

[1] C. Michel, M. Hervieu, M. M. Borel, A. Grandin, F. Deslandes, J. Provost, and B. Raveau, Z. Phys. B **68**, 421 (1987).
[2] H. Meada, Y. Tanaka, M. Fukutomi, and T. Asano, Jpn. J. Appl. Phys. **27**, L209 (1988).
[3] M. A. Subramanian, C. C. Torardi, J. C. Calabrese, J. Gopalakrishnan, K. J. Morrissey, T. R. Askew, R. B. Flippen, U. Chowdhry, and A. W. Sleight, Science **239**, 1015 (1988).
[4] J. L. Tallon, R. G. Bukley, P. W. Gilberd, M. R. Presland, L. W. M. Brown, M. E. Bowden, L. A. Christian, and R. Goquel, Nature (London) **333**, 153 (1988).
[5] N. Kijima, H. Endo, J. Tsuchiya, A. Sumiyama, H. Mizuno, and Y. Oguri, Jpn. J. Appl. Phys. **27**, L1852 (1988).
[6] J. L. Tallon, R. G. Bukley, P. W. Gilberd, and M. R. Presland, Physica C **158**, 247 (1989).
[7] G. Kh. Rozenberg, L. A. Kvichko, R. Yu. Itskovich, P. V. Mateĭchenko, R. F. Rimakaeva, T. S. Teplitskaya, and G. N. Belousov, Sverkhprovodimost: Fiz., Khim., Tekh. **6**, 635 (1993).
[8] M. Takano, J. Takada, K. Oda, H. Kitaguchi, Y. Miura, Y. Ikeda, Y. Tomii, and H. Mazaki, Jpn. J. Appl. Phys. **27**, L1041 (1988).
[9] I. V. Ol'khovik, E. D. Politov, S. G. Prutchenko, and Yu. V. Yurchenko, Sverkhprovodimost: Fiz., Khim., Tekh. **6**, 627 (1993).
[10] N. Fukushima, H. Niu, and K. Ando, Jpn. J. Appl. Phys. **27**, L1432 (1988).
[11] H. Furukava, H. Enomoto, T. Kishimoto, J. Shin, Y. Takano, N. Mori, and H. Ozaki, J. Appl. Phys. **30**, L346 (1991).
[12] A. I. Egorov, G. I. Karazhanova, Yu. P. Smirnov, A. E. Sovestnov, A. V. Tyunis, and V. A. Shaburov, Sverkhprovodimost: Fiz., Khim., Tekh. **6**, 327 (1993).
[13] V. V. Zhgamadze, R. G. Kokhreidze, N. G. Margiani, A. N. Mestvirishvili, S. V. Odenov, N. A. Papunashvili, G. A. Tsintsadze, and G. A. Shurgaya, Fiz. Nizk. Temp. **29**, 1363 (2003) [Low Temp. Phys. **29**, 1036 (2003)].
[14] V. É. Gasumyants, S. A. Kaz'min, V. I. Kaĭdanov, S. A. Lykov, V. A. Polyakov, and S. E. Khabarov, Sverkhprovodimost: Fiz., Khim., Tekh. **4**, 586 (1991) [Superconductivity **4**, 504 (1991)].
[15] T. E. Os'kina, Yu. D. Tret'yakov, and Yu. V. Badun, Sverkhprovodimost: Fiz., Khim., Tekh. **3**, 2249 (1991) [Superconductivity **3**, 1680 (1991)].
[16] J. B. Schlenoff, W. J. Rink, and L. Seger, Physica C **180**, 387 (1991).
[17] P. G. Vasilev, M. Mikhov, D. Kovacheva, and K. Petrov, Sverkhprovodimost' (KIAE) **3**, 1075 (1990) [*sic*].
[18] M. G. Zemlyanov, A. V. Irodova, I. V. Krylov, P. P. Parshin, N. S. Tolmacheva, L. D. Shustov, P. I. Soldatov, and S. Kh. Suleĭmanov, Sverkhprovodimost: Fiz., Khim., Tekh. **6**, 556 (1993).
[19] A. A. Zhukov and V. V. Moshchalkov, Sverkhprovodimost: Fiz., Khim., Tekh. **4**, 850 (1991) [Superconductivity **4**, 759 (1991)].
[20] V. N. Konev, T. B. Popova, and N. B. Petrukhovskaya, Sverkhprovodimost: Fiz., Khim., Tekh. **6**, 412 (1993).

Translated by M. E. Alferieff

LOW-TEMPERATURE MAGNETISM

Energy dissipation of a 180° domain wall in a defect field. Influence of film thickness

Yu. I. Dzhezherya and M. V. Sorokin*

Institute of Magnetism, Ukrainian National Academy of Sciences and MON, bul. Vernadskogo 36-b, Kiev 03142, Ukraine

(Submitted January 16, 2004; revised June 4, 2004)
Fiz. Nizk. Temp. **30**, 1252–1260 (December 2004)

An effective equation of motion for a 180° domain wall, taking account of energy losses due to the excitation of flexural waves of the wall when it interacts with point defects, is derived for a ferromagnetic film of arbitrary thickness. The domain wall is studied in the potential well produced by a nonuniform magnetic field. The influence of defects on the motion of a wall with constant velocity and small forced oscillations of the wall are investigated on the basis of exact particular solutions of the equation derived. © *2004 American Institute of Physics.*
[DOI: 10.1063/1.1820032]

Any ferromagnetic material contains defects which influence the motion of domain walls (DWs).

Ordinarily, the coercivity of a ferromagnet (FM) is attributed to the presence of defects. It appears as a result of pinning of DWs in the potential relief produced by defects.[1]

In addition, the interaction of a DW with defects results in energy losses by the wall.[2–12] These losses are due to either the irreversible transfer of the energy of a DW to spin waves (SWs) in an interaction process[3–5,7–12] or the excitation of the internal degrees of freedom of the defects.[2,6]

Previous works investigating the energy losses and braking of a solitary DW on defects with no internal degrees of freedom have shown that for stationary motion of the DW in a thick ferromagnetic film the contribution of defects to friction tends to a constant value as the velocity v of the DW tends to zero,[4,5,8,9] and in a thin film this contribution grows without limit as $1/v$ (or $1/\sqrt{v}$).[9–12] The result is that the stationary motion of a DW in a thin film is unstable for low velocities ranging from zero up to a critical value v_{cr},[11,12] i.e. in the region where the friction force $F_f(v)$ decreases with increasing velocity, specifically, for $dF_f(v)/dv<0$ for $v \in [0,v_{cr}]$.

A solitary DW cannot exist in a real FM—the DW becomes unstable because of the magnetic-dipole interaction. The conventional method for stabilizing a wall by means of a nonuniform magnetic field (MF) is equivalent to the influence on the DW of a potential well whose presence results in the appearance of a gap in the SW spectrum. This makes the character of DW braking on defects in a potential well qualitatively different from the braking of a "free" DW.[4,5,8–12]

In the present paper these changes and the special features due to the influence of the thickness L of a ferromagnetic film on the character of the braking are investigated.

1. EFFECTIVE EQUATION OF MOTION OF DOMAIN WALLS IN A DEFECT FIELD

We shall consider the braking of DWs by defects on the basis of a model of randomly distributed point defects[7–12] (the linear dimensions of a defect are much smaller than the DW thickness l: $\Delta V^{1/3} \ll l$, where ΔV is the volume of the defect).

Since the excitation of magnons, which correspond to flexural spin waves,[4,7] makes the largest contribution to the DW dissipation due to energy transfer to the magnon thermostat, we shall study DW motion on the basis of an equation for the DW coordinate x_0 which describes the motion of the DW and the propagation of flexural SWs:[13]

$$m\frac{\partial^2 x_0}{\partial t^2}+\kappa\frac{\partial x_0}{\partial t}-\sigma\frac{\partial^2 x_0}{\partial \mathbf{r}_\perp^2}=F(r_\perp,t). \tag{1}$$

m is the effective mass of the DW, κ is the friction coefficient (corresponding to the Gilbert relaxation term in the Landau–Lifshitz equation), and σ is the surface energy density of the DW.

The motion of a DW can be described approximately on the basis of Eq. (1) for a wide class of magnets: materials with magnetic bubble domains, weak FMs, and so on. Since our goal is to obtain general results we shall not specify the values of m, κ and σ more precisely until we need to do so. However, at the stage of numerical calculations, where the magnetization distribution in a DW must be given, we shall assume a Bloch DW in a uniaxial FM (see, for example, Ref. 13). Then

$$m=1/2\,\pi g^2 l,\quad \kappa=2\alpha_G M/gl,\quad \sigma=2\sqrt{\alpha\beta}M^2,$$

g is the gyromagnetic ratio, M is the saturation magnetization, α_G is the Gilbert relaxation constant, α and β are the exchange interaction and uniaxial anisotropy constants, and $l=\sqrt{\alpha/\beta}$.

The equation (1) is written in a coordinate system where the Ox axis is oriented in the direction of the magnetization distribution in the DW, the Oz axis is perpendicular to the surface of the film (with respect to the thickness), and $\mathbf{r}_\perp=(y,z)$ is the radius vector in the plane of the DW.

The equation (1) must be solved together with boundary conditions which in the absence of pinning of the magnetic moment on the surface of the film have the form

$$\left.\frac{\partial x_0}{\partial z}\right|_{z=0} = \left.\frac{\partial x_0}{\partial z}\right|_{z=L} = 0.$$

The right-hand side of Eq. (1) is the effective force acting on the DW. It contains a contribution due to the external impelling magnetic field—$2MH(t)$, the contribution of defects, and the force exerted on the DW by a one-dimensional potential well. We shall choose it in a form which simplifies the calculations, making the assumption that when the position x_0 of the DW moves away from the center of the well there arises a restoring force which for small displacements can be described by a linear function Kx_0. For example, in a nonuniform MF with a constant gradient the restoring force will remain linear for any displacements of the DW.

It remains to determine the contribution of defects in Eq. (1) more accurately. As shown in Ref. 9, for a point defect with a δ-shaped localization potential the interaction force acting between the defect and a DW is independent of the nature of the defect (nonuniformity of the exchange interaction parameter, uniaxial anisotropy, saturation magnetization, and so on) and is determined entirely by the magnetization distribution.

Therefore, on the basis of everything said above concerning the forces acting on the DW, Eq. (1) for solving the problem formulated in this work becomes

$$m\frac{\partial^2 x_0}{\partial t^2} + \kappa\frac{\partial x_0}{\partial t} - \sigma\frac{\partial^2 x_0}{\partial \mathbf{r}_\perp^2} + Kx_0 = 2MH(t) + \varepsilon\sigma l\sum_n f\left(\frac{x_n - x_0}{l}\right)\delta(\mathbf{r}_\perp - \mathbf{r}_{\perp,n}), \quad (2)$$

where x_n and $\mathbf{r}_{\perp,n}$ are the coordinates of the nth defect and $\varepsilon \ll 1$ is the DW–defect interaction parameter. For a defect with uniaxial anisotropy of magnitude $\Delta\beta$, $\varepsilon = (\Delta\beta/2\beta)\times(\Delta V/l^3)$. The function $f(\ldots)$ describes the magnetization distribution inside the DW. For a Bloch DW $f(x) = -\sinh x/\cosh^3 x$.

It is convenient to write the equation for x_0 in a dimensionless form using the new variables $q = x_0/l$, $\xi_n = x_n/l$, $\tau = \omega_0 t$, $\boldsymbol{\rho} = (\eta,\zeta) = \mathbf{r}_\perp/\Lambda$, $\omega_0 = \sqrt{K/m}$, $\Lambda = \sqrt{\sigma/K}$, $2\lambda = \kappa/\sqrt{Km}$, and $h(\tau) = 2MH/Kl$:

$$\frac{\partial^2 q}{\partial \tau^2} + 2\lambda\frac{\partial q}{\partial \tau} - \frac{\partial^2 q}{\partial \boldsymbol{\rho}^2} + q = h(\tau) + \varepsilon\sum_n f(\xi_n - q)\,\delta(\boldsymbol{\rho} - \boldsymbol{\rho}_n). \quad (3)$$

We shall solve Eq. (3) by applying the method used in Refs. 3 and 8–12. Accordingly, we represent $q(\boldsymbol{\rho},\tau)$ in the form

$$q(\boldsymbol{\rho},\tau) = q_0(\tau) + \varepsilon u(\boldsymbol{\rho},\tau), \quad (4)$$

where the term $q_0(\tau)$ describes the motion of the DW and $u(\boldsymbol{\rho},\tau)$ describes the distortion of the shape of the DW, i.e. flexural SWs.

Substituting the expression (4) into Eq. (3) and separating terms we obtain the equations for the excitations

$$\left\{\frac{\partial^2}{\partial \tau^2} + 2\lambda\frac{\partial}{\partial \tau} - \frac{\partial^2}{\partial \boldsymbol{\rho}^2} + 1\right\}u = \sum_n f(\xi_n - q_0(\tau))\,\delta(\boldsymbol{\rho} - \boldsymbol{\rho}_n), \quad (5)$$

$$\partial u/\partial \varsigma|_{\varsigma=0} = \partial u/\partial \varsigma|_{\varsigma=L/\Lambda} = 0$$

and for the coordinate $q_0(\tau)$

$$\frac{\partial^2 q}{\partial \tau^2} + 2\lambda\frac{\partial q}{\partial \tau} + q = h(\tau) - \varepsilon^2\frac{\Lambda^2}{S}\left\langle\sum_n u(\boldsymbol{\rho}_n,\tau) f'(\xi_n - q_0(\tau))\right\rangle, \quad (6)$$

where S is the area of the DW, the brackets denote averaging over the plane of the DW and the position of the defects ($\langle u(\boldsymbol{\rho},\tau\rangle = 0$), and the prime indicates a derivative with respect to the argument of the function.

The equation for the excitations $u(\boldsymbol{\rho},\tau)$ must be solved in order to obtain a closed-form equation for $q_0(\tau)$. For this we represent $u(\boldsymbol{\rho},\tau)$ as a Fourier cosine series so that the boundary conditions are satisfied:

$$u(\boldsymbol{\rho},\tau) = \frac{2}{L/\Lambda}\sum_{p=0}^{\infty} u_p(\eta,\tau)\cos\left(\frac{\pi p}{L/\Lambda}\varsigma\right). \quad (7)$$

The solution of the equations for the Fourier components $u_p(\eta,\tau)$

$$\left(\frac{\partial^2}{\partial \tau^2} + 2\lambda\frac{\partial}{\partial \tau} - \frac{\partial^2}{\partial \eta^2} + 1 + \frac{\pi^2\rho^2}{L^2/\Lambda^2}\right)u_p = \sum_n f(\xi_n - q_0(\tau))\,\delta(\eta - \eta_n)\cos\left(\frac{\pi p}{L/\Lambda}\varsigma_n\right) \quad (8)$$

can be represented in terms of the corresponding Green's functions

$$G_p(\tau,\eta) = \frac{1}{2}\exp(-\lambda\tau)\Theta(\tau^2 - \eta^2) \times J_0\left[\sqrt{1 + \frac{\pi^2 p^2}{L^2/\Lambda^2} - \lambda^2}\,(\tau^2 - \eta^2)^{1/2}\right]. \quad (9)$$

Substituting $u(\boldsymbol{\rho},\tau)$ found in this manner into Eq. (6) yields

$$\frac{\partial^2 q_0}{\partial \tau^2} + 2\lambda\frac{\partial q_0}{\partial t} + q_0 = h(\tau) - \frac{2\varepsilon^2\Lambda^2}{LS}\left\langle\sum_{p=0}^{\infty}\sum_{n,m}\int_{-\infty}^{\infty} d\tau' G_p \times(\tau - \tau', \eta_n - \eta_m) f'(\xi_n - q_0(\tau)) \times f(\xi_m - q_0(\tau'))\cos\left(\frac{\pi p}{L/\Lambda}\varsigma_n\right)\cos\left(\frac{\pi p}{L/\Lambda}\varsigma_m\right)\right\rangle. \quad (10)$$

The averaging procedure

$$\left\langle\sum_{n,m}\ldots\right\rangle \to \left\langle\sum_n \ldots\right\rangle \to c(S/L)\Lambda l\int_0^{L/\Lambda} d\varsigma\int_{-\infty}^{\infty} d\xi, \quad (11)$$

where c is the defect concentration, simplifies the expression (10):

$$\frac{\partial^2 q_0}{\partial \tau^2}+2\lambda\frac{\partial q_0}{\partial \tau}+q_0+\frac{\gamma}{L/\Lambda}\sum_{p=0}^{\infty}\int_{-\infty}^{\infty}d\tau' G_p(\tau-\tau',0)\times g(q_0(\tau)-q_0(\tau'))=h(\tau), \tag{12}$$

where $\gamma=\varepsilon^2 c\Lambda^2 l$,

$$g(q_0(\tau)-q_0(\tau'))=\int_{-\infty}^{\infty}d\xi f'(\xi-q_0(\tau))f(\xi-q_0(\tau')).$$

For example, for a Bloch DW

$$g(x)=\frac{1}{4}\frac{d^3}{dx^3}\left(\int_{-\infty}^{\infty}d\xi\frac{1}{\cosh^2\xi\cosh^2(\xi-x)}\right)=\frac{d^3}{dx^3}\left(\frac{x\cosh x-\sinh x}{\sinh^3 x}\right). \tag{13}$$

The equation (12) describes the influence of defects on the motion of a DW in an arbitrary external MF. However, the solution of this equation cannot be found in a general form.

Consequently, we shall consider two particular cases where Eq. (12) can be solved analytically and which correspond to real experiments with DWs in a nonuniform MF (see, for example, Ref. 14): small oscillations of DWs and the motion of DWs with a constant velocity.

2. SMALL OSCILLATIONS OF DOMAIN WALLS

The problem of small oscillations in a periodic field $h(\tau)=\mathrm{Re}\,h_0\exp(i\Omega\tau)$ ($\Omega=\omega/\omega_0$, ω is the frequency of the external MF) corresponds to Eq. (12) linearized with respect to $q_0(\tau)$:

$$\frac{\partial^2 q_0}{\partial \tau^2}+2\lambda\frac{\partial q_0}{\partial \tau}+q_0+\frac{\gamma g'(0)}{L/\Lambda}\times\sum_{p=0}^{\infty}\int_{-\infty}^{\infty}d\tau' G_p(\tau-\tau',0)(q_0(\tau)-q_0(\tau'))=h(\tau) \tag{14}$$

(for a Bloch DW $g'(0)=16/21$).

The solution is

$$q_0(\tau)=A\cos(\Omega\tau+\delta), \tag{15}$$

where the amplitude A and the phase δ of the forced oscillations are given by the expressions

$$A=\frac{h_0}{\sqrt{[-\Omega^2+1+\Delta(\Omega)]^2+4\lambda_{\mathrm{eff}}^2\Omega^2}},\qquad \tan\delta=\frac{2\lambda_{\mathrm{eff}}\Omega}{\Omega^2-1-\Delta(\Omega)}, \tag{16}$$

and $\lambda_{\mathrm{eff}}=\lambda_{\mathrm{eff}}(\Omega)$ is an effective relaxation constant. This follows from the energy balance equation, which can be derived from Eq. (14):

$$\overline{h(\tau)\dot q_0(\tau)}=2\left[\lambda\overline{\dot q_0^2(\tau)}+\frac{\gamma g'(0)}{2L/\Lambda}\times\overline{\dot q_0(\tau)\int_{-\infty}^{\infty}d\tau' G(\tau-\tau',0)(q_0(\tau)-q_0(\tau'))}\right], \tag{17}$$

where the overbar denotes averaging over time. The left-hand side of Eq. (17) is, to within a constant factor, the average strength of the external force. It equals the energy losses determined by the expression on the right-hand side.

$$\lambda_{\mathrm{eff}}(\Omega)=\frac{\overline{h(\tau)\dot q_0(\tau)}}{2\overline{\dot q_0^2(\tau)}}=\lambda+\frac{\gamma g'(0)}{4L/\Lambda}\sum_{p=0}^{\infty}\int_0^{\infty}d\tau\,\mathrm{e}^{-\lambda\tau}J_0\times\left(\tau\sqrt{1+\frac{\pi^2p^2}{L^2/\Lambda^2}-\lambda}\right)\frac{\sin\Omega\tau}{\Omega}. \tag{18}$$

Performing the integration in Eq. (18)

$$\lambda_{\mathrm{eff}}(\Omega)=\lambda+\frac{\sqrt{2}\,\gamma g'(0)}{8L/\Lambda}\sum_{p=0}^{\infty}\sqrt{\Omega^2-1-\frac{\pi^2p^2}{L^2\Lambda^2}+\sqrt{\left(\Omega^2-1-\frac{\pi^2p^2}{L^2/\Lambda^2}\right)^2+4\Omega^2\lambda^2}}\,\Omega^{-1}\left[\left(\Omega^2-1-\frac{\pi^2p^2}{L^2/\Lambda^2}\right)^2+4\Omega^2\lambda^2\right]^{-1/2} \tag{19}$$

we obtain an infinite series which converges for any values of Ω, λ, and L/Λ [$\Delta(\Omega)$ is given by a complicated expression similar to Eq. (19)].

The plots constructed for $\lambda_{\mathrm{eff}}(\Omega)$ and $A(\Omega)$ confirm the conclusion that the influence of defects is stronger in thin FM films. They show an interesting feature of damping on defects with forced oscillations of DWs.

The function $\lambda_{\mathrm{eff}}(\Omega)$ (Fig. 1a) possesses maxima at the characteristic oscillation frequency of a DW in a potential well $\Omega\approx\Omega_0=1$ and at frequencies close to $\Omega_p=\sqrt{1+\pi^2p^2\Lambda^2/L^2}$, where $p=1,2,\ldots$. The appearance of each of these maxima is due to the resonance radiation of a definite mode of the flexural oscillations of the DW (uniform $p=0$ and nonuniform $p=1,2,\ldots$ over the film thickness), when the frequency of the external field reaches the values Ω_p. The thicker the film, the closer the peaks and their values are to one another. It is obvious that for some L the peaks will become essentially indistinguishable. The intensification of losses on defects is also reflected in the function $A(\Omega)$ (Fig. 1b): the amplitude of the forced oscillations has minima at the corresponding frequencies.

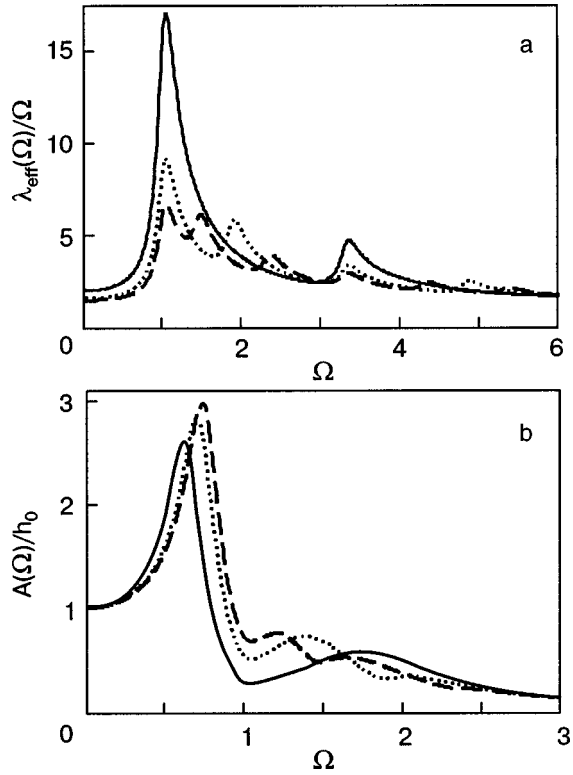

FIG. 1. Frequency dependences of the effective relaxation parameter (a) and amplitude of forced oscillations (b) for various film thicknesses, L/Λ: 1 (solid line), 2 (dotted line), 3 (dashed line), $\gamma=5$, $\lambda=0.1$.

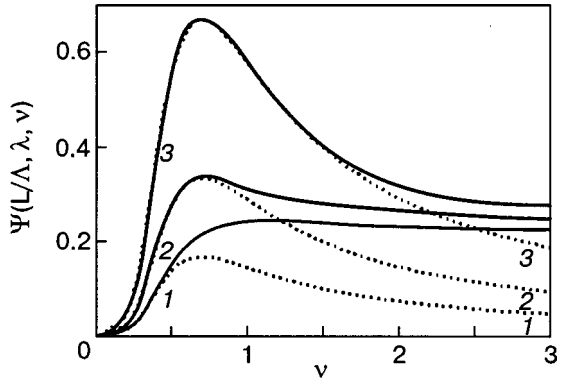

FIG. 2. Plots of the function $\Psi(L/\Lambda,\lambda,\nu)$, reflecting the velocity dependence of the friction force due to defects, for various film thicknesses, L/Λ: 0.5 (1), 1 (2), 2 (3). The dotted lines correspond to $\Psi_0(L/\Lambda,\lambda,\nu)$. $\lambda=0.1$.

3. STATIONARY MOTION OF DOMAIN WALLS

In materials with weak dissipative properties ($\lambda \ll 1$), defects of the magnetic structure can result in the appearance of qualitative features in the character of the braking of a DW moving with constant velocity.[10–12]

It follows from Eq. (12) that for a DW in a potential well such motion can occur in an external field increasing linearly as $h(\tau)=\dot{h}\tau$. In this case we have

$$q_0(\tau) = -\Delta q + \nu\tau, \tag{20}$$

where $\nu = v/\omega_0 l$ is the reduced velocity of the DW ($\nu = \sqrt{2\pi M^2/Kl}(v/v_W)$ for a Bloch DW). The value of ν can be easily obtained from the equation of motion: $\nu=\dot{h}$.

The quantity Δq is a "phase shift"—the lag, due to the "friction" force acting on the wall, of the change in the coordinate of the DW from the increasing external field:

$$\Delta q = \tilde{F}_f(\nu) = 2\lambda\nu + (1/2)\gamma\Psi(L/\Lambda,\lambda,\nu), \tag{21}$$

$\tilde{F}_f(\nu)=\tilde{F}_f(\nu)=F_f(v)/Kl$ is the real friction force $F_f(v)$ scaled to Kl, and the function $\Psi(L/\Lambda,\lambda,\nu) = \Sigma_{p=0}^{\infty}\Psi_p(L/\Lambda,\lambda,\nu)$ describes the braking of a DW on defects:

$$\Psi_p(L/\Lambda,\lambda,\nu) = \frac{1}{L/\Lambda}\int_0^{\infty} d\tau \exp(-\lambda\tau) J_0 \times\left(\tau\sqrt{1+\frac{\pi^2 p^2}{L^2/\Lambda^2}-\lambda^2}\right) g(\nu\tau). \tag{22}$$

Each pth term corresponds to the contribution due to the emission of a definite mode of flexural oscillations of DW over the thickness of the film when the wall interacts with defects.

A numerical calculation of the function $\Psi(L/\Lambda,\lambda,\nu)$ shows (Fig. 2) that as the velocity increases, the friction force acting on defects at first increases, reaches a maximum value, and then decreases, tending asymptotically to a constant value. The thinner the film, the greater the maximum value and the higher the velocity at which the friction force reaches its asymptotic value are.

According to Fig. 2, even with $L/\Lambda=2$ the plot of the friction force acting on defects is essentially identical to the curve $\Psi_0(L/\Lambda,\lambda,\nu)$ characterizing the braking on defects only as a result of the emission of excitations which are uniform over the film thickness. This simplifies the analysis of the influence of defects on the character of the braking of DWs in thin films.

A. Stationary motion of a domain wall in a thin film. Instability

Let us consider the braking of a DW in a thin film ($L \ll \Lambda$). In this case it can be assumed that only flexural oscillations which are uniform over the film thickness ("zeroth mode" $p=0$) contribute to the braking process. When calculating the friction force acting on defects we shall neglect the damping of the SWs, i.e. we set $\lambda=0$. This is admissable for small values of the relaxation constant $\lambda \ll 1$, since in this case damping affects only the asymptotic behavior of the friction force acting on defects in the limit $\nu\to 0$: $\lambda=0$, $(\tilde{F}_f - 2\lambda\nu) \sim \nu^{-11/2}\exp(-\pi/\nu)$; $\lambda\neq 0$, $(\tilde{F}_f - 2\lambda\nu)\sim\lambda\nu$.

On this basis we change notation and represent the friction force in the form

$$\tilde{F}_f(\nu) = 2\lambda\nu + (1/2)\gamma^*\Phi(\nu), \tag{23}$$

where $\gamma^* = \gamma\Lambda/L = \varepsilon^2 c\Lambda^3(l/L)$,

$$\Phi(\nu) = \int_0^{\infty} d\tau J_0(\tau) g(\nu\tau).$$

The function $\Phi(\nu)$ can be written in a different form, using a

Fourier integral expansion of the functions $1/\cosh^2\xi$ and $1/\cosh^2(\xi-x)$ in the integral representation $g(\nu\tau)$ (see Eq. (13)):

$$\Phi(\nu)=\frac{\pi}{4\nu^6}\int_1^\infty dk\,\frac{k^5}{\sqrt{k^2-1}\sinh^2(\pi k/2\nu)}.$$

The asymptotic behavior of the function $\Phi(\nu)$ at low velocities can be easily obtained from the latter expression. If $\nu \ll 1$, then $\Phi(\nu)$ is approximately determined by an integral whose value is[15]

$$\Phi(\nu)|_{\upsilon\ll 1}\approx\frac{\pi}{\nu^6}\int_1^\infty dk\,\frac{k^5}{\sqrt{k^2-1}}\exp(-\pi k/\nu)$$

$$=\frac{\pi}{\nu^6}\left(\frac{d^4}{dx^4}K_1(x)\right)_{x=\pi/\nu}\xrightarrow[\nu\to 0]{}\frac{\pi}{\sqrt{2}\,\nu^{11/2}}$$

$$\times\exp(-\pi/\nu),$$

where $K_1(x)$ is a modified Bessel function.

It is remarkable that the function $\tilde{F}_f(\nu)/2\lambda=\nu+4^{-1}(\gamma^*/\lambda)\Phi(\nu)$ is a universal function of the velocity, depending on the single parameter γ^*/λ determining the relaxation properties of the system.

The expression (23) can be used as a basis for determining the parameter γ^* experimentally. Once the lag Δq of the DW has been determined, for known values of λ and prescribed velocity ν, the quantity γ^* can be found from the relation

$$\gamma^*=2(\Delta q-2\lambda\nu)/\Phi(\nu). \tag{24}$$

If the constant γ^* is of the order of λ, then the defects of the magnetic structure make a large contribution to the force braking a DW.

Figure 3a shows a plot of the function $\tilde{F}_f(\nu)/2\lambda$ for different values of the parameter γ^*/λ. For comparison, the figure also shows the function for $\gamma^*/\lambda=0$, i.e. neglecting the contribution of defects.

The function $\Phi(\nu)$ depends strongly on the form of the function $g(\nu\tau)$. In turn the magnetization distribution inside a wall determines $g(\nu\tau)$ (the plots in Fig. 3 were constructed for a Bloch DW).

The asymptotic behavior of the function $\Phi(\nu)$ can be easily determined for a DW moving with velocity $\nu\gg 1$: $\Phi(\nu)=1/15\nu$, which corresponds exactly to the results obtained in previous investigations[7–12] for a "free" DW moving outside a potential well.

In summary, for velocities $\upsilon\gg\omega_0 l$ the friction force is independent of the depth of the potential well. The presence of a well is significant for the motion of DWs with velocities $\upsilon\sim\omega_0 l$. In this range (Fig. 3a) $\tilde{F}_f(\nu)$ depends strongly on the influence of defects, whose contribution is characterized quantitatively by the parameter γ^*/λ.

As γ^*/λ increases, two extrema appear in the function $\tilde{F}_f(\nu)$—at ν_1 and ν_2 (Fig. 3a, curve 3). On the section between ν_1 and ν_2 the behavior of the curve corresponds to a friction force decreasing with increasing DW velocity, indicating that the motion of the DW could be unstable in this velocity range according to the standard criterion $d\tilde{F}_f/d\nu<0$.

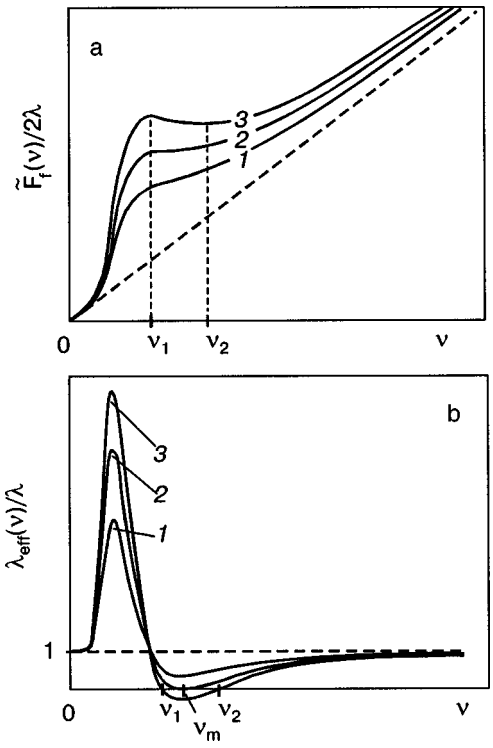

FIG. 3. Plots of the friction force $\tilde{F}_f(\nu)/2\lambda$ (a) and the effective relaxation parameter $\lambda_{eff}(\nu)/\lambda$ (b) versus the reduced velocity of a DW for various values of γ^*/λ: $\gamma_3^*/\lambda_3>\gamma_2^*/\lambda_2>\gamma_1^*/\lambda_1$. The dashed line corresponds to $\gamma^*=0$.

As a characteristic of $\tilde{F}_f(\nu)$ we introduce

$$\lambda_{\text{eff}}(\nu)=\frac{1}{2}\frac{d\tilde{F}_f(\nu)}{d\nu}=\lambda+\frac{1}{4}\gamma^*\frac{d\Phi(\nu)}{d\nu}$$

$$=\lambda+\frac{1}{4}\gamma^*\int_0^\infty d\tau J_0(\tau)\tau g'(\nu\tau). \tag{25}$$

In the absence of defects, for $\gamma^*=0$, we have $\lambda_{\text{eff}}(\nu)=\lambda$. Thus $\lambda_{\text{eff}}(\nu)$ can be regarded as an effective, dissipative, velocity-dependent constant.

Figure 3b shows the curves $\lambda_{\text{eff}}(\nu)/\lambda$ for various values of γ^*/λ. It can be concluded from their behavior that defects play a large role in the braking of DWs at low velocities.

The points where $\lambda_{\text{eff}}(\nu)$ vanish are identical to the critical velocities ν_1 and ν_2, which exist only for $\gamma^*/\lambda>4/|\Phi'(\nu_m)|\approx 15.27$ (where the argument ν_m is the value for which the derivative of the function $\Phi(\nu)$ has its minimum value).

Analysis of the function $\lambda_{\text{eff}}(\nu)$ shows how the values of the critical velocity behave if K—the coupling constant between the DW and the potential well—tends to zero.

For this we write the condition $\lambda_{\text{eff}}(\nu)=0$ in the form

$$\lambda/\gamma^*+4^{-1}d\Phi(\nu)/d\nu=0. \tag{26}$$

If $K\to 0$, then $\lambda/\gamma^*\to 0$ and the critical velocity ν_1 tends to the finite limit $\nu_0\approx 0.69$ (where ν_0 is the value of the argument for which the derivative of the function vanishes). On the other hand, $\upsilon_1=\nu_1 l\sqrt{K/m}\to 0$ following a square-root law.

It can be shown in exactly the same manner that the value of υ_2 tends to a finite limit. Indeed, $\nu_2\to\infty$ as λ/γ^*

$\to 0$, and for high DW velocities Eq. (26) can be written in the form $\lambda/\gamma^* - 1/15(\nu_2)^2 = 0$ or, using the initial notation,

$$v_2 = \sqrt{2/15}\varepsilon(cl^3\sigma^{3/2}/L\kappa\sqrt{m})^{1/2}. \tag{27}$$

The quantity (27) is identical, to within the notation, to a previous result obtained in an analysis of the motion of a "free" DW.[11,12] As the depth of the potential well tends to zero, the region with the anomalous velocity dependence of the friction force ($d\tilde{F}_f/d\nu = 0$) $\nu \in [\nu_1, \nu_2]$ is identical to the velocity interval $\nu \in [0, \nu_{cr}]$, where the stationary motion of a "free" DW is unstable. In other words, as $K \to 0$ the velocity dependence of the friction force has the form characteristic for a "free" DW.[9–12]

In conclusion, we note that even in the zone $\nu \in [\nu_1, \nu_2]$, where $d\tilde{F}_f/d\nu < 0$, the presence of a potential well can stabilize the stationary motion of a DW. To determine the criterion for the motion of a wall to be stable we shall investigate the solution (20) for stability with respect to small perturbations.

For this we write the solution as

$$q_0(\tau) = \nu\tau - \Delta q + \theta(\tau), \tag{28}$$

where $\theta(\tau)$ denotes a small deviation of the coordinate $q_0(\tau)$ from the value $\nu\tau - \Delta q$, describing the stationary motion of the DW.

The equation obtained for $\theta(\tau)$ by linearizing the equation of motion of a DW is

$$\frac{\partial^2\theta}{\partial\tau^2} + 2\lambda\frac{\partial\theta}{\partial\tau} + \theta + \gamma^*\int_{-\infty}^{\infty} d\tau' G(\tau - \tau', 0) g'(\nu(\tau - \tau')) \times (\theta(\tau) - \theta(\tau')) = 0. \tag{29}$$

We seek its solution in the form $\exp(\mu\tau)$. It is obvious that stationary motion is stable if the small correction $\theta(\tau)$ decays with time, i.e. the stability criterion is $\mathrm{Re}\,\mu < 0$. Substituting the expression for the perturbation in the form $\theta(\tau) = \theta_0 \exp(\mu\tau)$ into Eq. (29) we obtain the characteristic equation

$$\mu^2 + 2\lambda\mu + 1 + \frac{\gamma^*}{2}\int_{-\infty}^{\infty} d\tau J_0(\tau) g'(\nu\tau)(1 - \exp(\mu\tau)) = 0. \tag{30}$$

Since λ and $\gamma^* \ll 1$ we seek the solution of the transcendental equation (30) in the form

$$\mu = i + i\mu' - \mu'', \tag{31}$$

where μ' is a correction to the characteristic oscillation frequency of a moving DW, and μ'' is the damping constant for small perturbations $\theta(\tau)$. To within terms of first-order in λ and γ^* these quantities are

$$\mu' = \frac{\gamma^*}{4}\int_0^{\infty} d\tau J_0(\tau)(1 - \cos\tau) g'(\nu\tau),$$

$$\mu'' = \lambda + \frac{\gamma^*}{4}\int_0^{\infty} d\tau J_0(\tau)\sin\tau\, g'(\nu\tau). \tag{32}$$

If $\mu'' > 0$, then the perturbation $\theta(\tau)$ decays and the stationary motion of a DW will be stable.

Figure 4a shows $\mu''(\nu)/\lambda$ for various values of γ^*/λ. We note that in the presence of a potential well the criterion for stable uniform motion $\mu'' > 0$ is different from the criterion $\lambda_{\mathrm{eff}} > 0$. This follows from Fig. 4b which shows the values of $\mu''(\nu)$ and $\lambda_{\mathrm{eff}}(\nu)$ for $\gamma^*/\lambda = 40$. The hatch marks in the figure mark the region between ν_3 and ν_4 where the stationary motion of a DW is unstable.

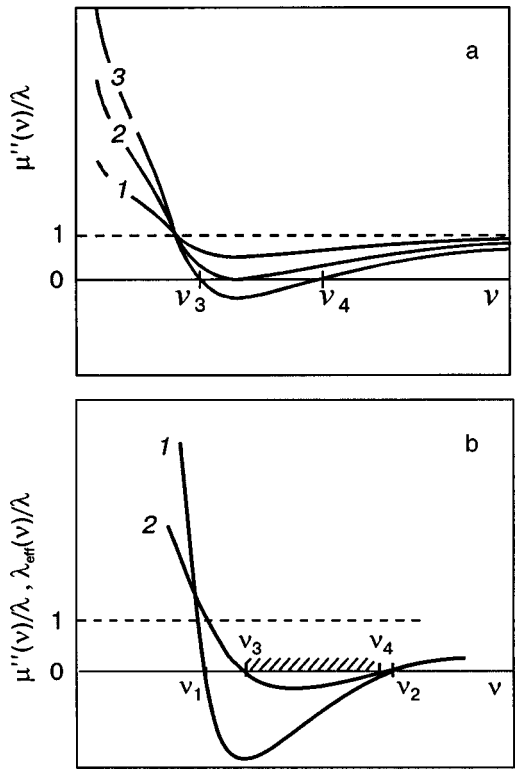

FIG. 4. Plots of the function $\mu''(\nu)/\lambda$ for various values of γ^*/λ: $\gamma_3^*/\lambda_3 > \gamma_2^*/\lambda_2 > \gamma_1^*/\lambda_1$ (a). Comparison of the functions $\lambda_{\mathrm{eff}}(\nu)/\lambda$ (curve *1*) and $\mu''(\nu)/\lambda$ (curve *2*), $\gamma^*/\lambda = 40$ (b).

The stabilizing effect of a potential well explains the fact that the region $[\nu_3, \nu_4]$ is different from the region $[\nu_1, \nu_2]$. As $K \to 0$, the region $[\nu_3, \nu_4] \to [\nu_1, \nu_2] \to [0, \nu_{cr}]$.

It follows from Eq. (32) that a zone of unstable motion of a DW, for which $\mu'' < 0$, appears if $\gamma^*/\lambda > 30.53$.

B. Stationary motion of a domain wall in a thick film. Coercivity

Analysis of the functions in Fig. 2 shows that if the film thickness is of the order of several Λ, then the friction force due to defects acting on a DW with $\nu \gg 1$ is close to a constant value $\tilde{F}_0$.

To estimate this quantity we shall examine the braking of a DW in a thick film ($L \gg \Lambda$). In this case the spectrum of flexural SWs over the thickness (z) changes from discrete to quasicontinuous and the boundary conditions on the surface of the film can be neglected, i.e. the problem actually reduces to the braking of a DW in an unbounded FM.

In this case, to solve Eq. (5) $u(\boldsymbol{\rho}, \tau)$ can be represented by, for example, a Fourier integral instead of a Fourier series:

$$u(\boldsymbol{\rho}, \tau) = (2\pi)^{-3}\int d\omega d\mathbf{k}\,\tilde{u}(\mathbf{k}, \omega)\exp[i(k\rho - \omega\tau)], \tag{33}$$

where $\tilde{u}(\mathbf{k}, \omega)$ is the Fourier transform of $u(\boldsymbol{\rho}, \tau)$.

Calculating $u(\boldsymbol{\rho},\tau)$, substituting the result into Eq. (6), and performing simple transformations we obtain the following expression for the friction force $\tilde{F}_f(\nu)$:

$$\tilde{F}_f(\nu)=2\lambda\nu+\frac{\gamma}{16}\int_0^\infty d\omega\,\frac{\omega^5}{\sinh^2(\pi\omega/2)}\times\left[\frac{\pi}{2}-\arctan\frac{1-\omega^2\nu^2}{2\lambda\omega\nu}\right]. \quad (34)$$

It is found that the friction force $\tilde{F}_f(\nu)-2\lambda\nu$ due to defects has the asymptotic value $\sim 0.12\lambda\gamma\nu$ as $\nu\to 0$, and for high velocities ($\nu\gg 1$) it tends to the constant value

$$\tilde{F}_0=\frac{\pi\gamma}{16}\int_0^\infty d\omega\,\frac{\omega^5}{\sinh^2(\pi\omega/2)}\approx 0.102\gamma. \quad (35)$$

Therefore the real friction force acting on a DW tends to the value $F_0=0.102\gamma Kl=0.102\varepsilon^2 c l^2\sigma$. It is obvious that this quantity is independent of the presence of a "magnetic trap" (the parameter K). It can be shown that the same value obtains for the friction force for braking of a "free" DW on defects in an unbounded FM.

In this case, equating the friction force to the impelling force $2MH$ makes it easy to understand the physical meaning of the quantity obtained:

$$F_f(v)=\kappa v+F_0=2MH. \quad (36)$$

Thus the DW velocity

$$v=2M(H-H_c)/\kappa \quad (37)$$

is directly proportional to the difference of the external MF and a quantity H_c—the dynamical coercivity field.[4,5,8,9] Correspondingly, F_0 is the dynamical coercive force acting on a DW.

$$H_c=0.051\varepsilon^2 c l^2\sigma/M. \quad (38)$$

4. CONCLUSIONS

In summary, in the simplified model (2) the braking of a DW (due to the emission of flexural SWs) on microscopic defects can be described on the basis of the effective equation (12) for the DW coordinate.

The influence of defects on the motion of a DW with constant velocity and the harmonic oscillations of the wall can be determined by analyzing this equation in two particular cases which admit an analytical solution.

For forced oscillations of a DW in a FM film with arbitrary thickness the energy losses due to defects are of a resonance character. If the frequency of the external field is close to the characteristic frequency ω_0 of the DW in a potential well or the frequencies of flexural excitations which are nonuniform over the film thickness $\omega_p=\omega_0\sqrt{1+\pi^2 p^2\Lambda^2/L^2}$ ($p=1,2,\ldots$), then resonance emission of surface SWs occurs and energy losses of the DW increase sharply (Fig. 1).

For stationary motion of a DW, the braking process due to defects in the presence of a potential well ($K\neq 0$) is different from the braking process for a "free" DW.[3–12] As $v\to 0$, the contribution of defects to the friction force tends to zero for a film of any thickness (Fig. 2). For thin films ($L\ll\Lambda$) defects engender an anomalous N-type velocity dependence of the total friction force (Fig. 3a) and instability of stationary motion (Figs. 3b and 4).

In general, the contribution of defects to the braking force depends strongly on the film thickness. As L increases, the functional dependence of the friction force due to defects on the DW velocity changes (Fig. 2). For large film thicknesses ($L\gg\Lambda$) the influence of defects reduces to a manifestation of dynamical coercivity, first described in Refs. 4–5 and 8–9.

We thank V. G. Bar'yakhtar and Yu. I. Gorobtsov for helpful suggestions and a fruitful discussion of the results obtained in this work.

*Email: sorockin@ukr.net

[1] S. V. Vonsovskiĭ, *Magnetism*, Nauka, Moscow (1971).
[2] J. F. Kanak, J. Appl. Phys. **34**, 3356 (1963).
[3] A. N. Averkin, Fiz. Tver. Tela (Leningrad) **23**, 1573 (1981) [Sov. Phys. Solid State **23**, 921 (1981)].
[4] A. V. Zuev and B. A. Ivanov, Zh. Éksp. Teor. Fiz. **82**, 1679 (1982) [JETP **55**, 971 (1982)].
[5] B. A. Ivanov and S. N. Lyakhimets, Fiz. Tver. Tela (Leningrad) **32**, 528 (1990) [Sov. Phys. Solid State **32**, 306 (1990)].
[6] B. A. Ivanov and S. N. Lyakhimets, J. Magn. Magn. Mater. **86**, 51 (1990).
[7] Yu. I. Gorobets, V. I. Finokhin, and Yu. I. Dzhezherya, Ukr. Fiz. Zh. **36**, 1215 (1991).
[8] B. A. Ivanov and S. N. Lyakhimets, J. Magn. Magn. Mater. **112**, 26 (1992).
[9] B. A. Ivanov and S. N. Lyakhimets, IEEE Trans. Magn. **30**, 824 (1994).
[10] Yu. I. Gorobets, Yu. I. Dzhezherya, and V. I. Finokhin, Fiz. Tver. Tela (St. Petersburg) **35**, 335 (1993) [Phys. Solid State **35**, 170 (1993)].
[11] Yu. I. Dzhezherya and M. V. Sorokin, Fiz. Tver. Tela (St. Petersburg) **41**, 1231 (1999) [Phys. Solid State **41**, 1121 (1999)].
[12] Yu. I. Dzhezherya and M. V. Sorokin, Fizika i tekhnika vysokikh davleniĭ **10**, 86 (2000).
[13] A. Malozemoff and J. C. Slonczewski, *Magnetic Domain Walls in Bubble Materials*, Academic Press, N. Y. (1979); Mir, Moscow (1982).
[14] V. T. Synogach, J. Magn. Magn. Mater. **124**, 175 (1993).
[15] A. P. Prudnikov, Yu. A. Brychkov, and O. I. Marichev, *Integrals and Series*, Nauka, Moscow (1981).

Translated by M. E. Alferieff

Influence of light on the antiferromagnetic-insulator—ferromagnetic-metal phase transition in $Pr_{0.6}La_{0.1}Ca_{0.3}MnO_3$ thin films

P. Aleshkevych, M. Baran, R. Szymczak, and H. Szymczak

Institute of Physics, Polish Academy of Sciences, Al. Lotnikow 32/46, 02-668, Warsaw, Poland

V. A. Bedarev, V. I. Gapon,* and S. L. Gnatchenko

B. I. Verkin Institute for Low Temperature Physics and Engineering, Ukrainian National Academy of Sciences, pr. Lenina 47, Kharkov 61103, Ukraine

O. Yu. Gorbenko and A. R. Kaul'

Moscow State University, Moscow 119899, Russia
(Submitted March 16, 2004; revised April 20, 2004)
Fiz. Nizk. Temp. **30**, 1261–1271 (December 2004)

The influence of photoillumination on the magnetic and transport properties of epitaxial thin films of the manganite $Pr_{0.6}La_{0.1}Ca_{0.3}MnO_3$ is investigated. It is found that illuminating films with He–Ne laser light increases their magnetization and decreases their electric resistance, stimulating an antiferromagnetic-insulator—ferromagnetic-metal phase transition, which is observed in this crystal in a magnetic field at low temperatures. It is shown that the phase-transition field is appreciably lower after the films are photoilluminated. It is concluded that photoillumination gives rise to the formation and growth of ferromagnetic metallic clusters inside an antiferromagnetic insulating phase. The mechanism of the effect of light on the magnetic and electric states of the manganite $Pr_{0.6}La_{0.1}Ca_{0.3}MnO_3$ could be related with photoinduced electron transfer from Mn^{3+} to Mn^{4+} ions, which results in melting of the charge ordering present in this manganite in the antiferromagnetic insulating state, and gives rise to a transition of the crystal into a ferromagnetic metallic phase. © *2004 American Institute of Physics.* [DOI: 10.1063/1.1820033]

1. INTRODUCTION

The observation of colossal magnetoresistance in manganites containing Mn^{3+} and Mn^{4+} ions has engendered in the last ten years enormous interest in these compounds from the standpoints of science and applications. The electric resistance of manganites can decrease by an order of magnitude in a magnetic field near the Curie temperature or during magnetic field induced phase transitions. Of special interest are manganites whose resistive properties or the insulator—metal phase transition observed in them can be affected by photoillumination.[1–4] Examples of such manganites are $(La_{0.3}Nd_{0.7})_{2/3}Ca_{1/3}MnO_3$, photoilluminating which decreases the electric resistance,[1] and $Pr_{0.7}Ca_{0.3}MnO_3$, where light gives rise to a phase transition from the insulating into the metallic state.[2–4]

The insulator—metal phase transition in a $Pr_{0.7}Ca_{0.3}MnO_3$ single crystal was induced by pulsed Nd–YAG laser light with wavelength $\lambda = 532$ nm (second harmonic) at temperature $T = 30$ K. The authors attribute this photoinduced phase transition to melting of the charge ordering of Mn^{3+} and Mn^{4+} ions and formation of ferromagnetic (FM) metallic clusters inside an insulating antiferromagnetic (AFM) phase during photoillumination. Since manganites are opaque for visible light, the photoinduced phase transition in a $Pr_{0.7}Ca_{0.3}MnO_3$ single crystal occurs in a surface layer whose thickness is close to the penetration depth of the inducing light. In this connection thin films, which are rather transparent for the inducing radiation, are best for investigating the influence of light on phase transitions in manganites.

We recently observed the influence of light on a magnetic field induced antiferromagnet—ferromagnet phase transition in a thin $Pr_{0.6}La_{0.1}Ca_{0.3}MnO_3$ manganite film, which is rather transparent to visible light, at temperatures $T < 50$ K.[5] Illuminating the film with He–Ne ($\lambda = 633$ nm) or Ar ($\lambda = 488$ nm) laser light increased the magnetization and stimulated a phase transition from the AFM into the FM state. It should be noted that our experimental data[5] differ substantially from the results described in previous investigations of a photoinduced dielectric–metal phase transition in $Pr_{0.7}Ca_{0.3}MnO_3$ single crystals.[2–4] For example, the light flux density in experiments with a $Pr_{0.6}La_{0.1}Ca_{0.3}MnO_3$ film[5] was five orders of magnitude lower than the threshold light flux density giving rise to a photoinduced transition in the manganite $Pr_{0.7}Ca_{0.3}MnO_3$.[2–4] In addition, the illumination dose needed to achieve saturation of the photoinduced effect was 8–9 orders of magnitude higher in our experiments.

The ratio of Mn^{3+} and Mn^{4+} ions in the manganites $Pr_{0.6}La_{0.1}Ca_{0.3}MnO_3$ and $Pr_{0.7}Ca_{0.3}MnO_3$ is the same, and the $H-T$ magnetic phase diagrams of these compounds are similar.[5] On this basis the magnetic field induced phase transition from the AFM into the FM state, observed during magnetic measurements in a $Pr_{0.6}La_{0.1}Ca_{0.3}MnO_3$ film,[5] should be accompanied by a substantial decrease of the electric resistance, i.e. a transition from the insulating into the metallic state. In this connection it is of definite interest to study the

influence of photoillumination on the magnetization and conductivity of a $Pr_{0.6}La_{0.1}Ca_{0.3}MnO_3$ film in a magnetic field.

In the present paper we present the results of comprehensive investigations of the resistance and magnetic properties of $Pr_{0.6}La_{0.1}Ca_{0.3}MnO_3$ films in a magnetic field and the results of an investigation of the influence of light on a field induced antiferromagnetic-insulator—ferromagnetic-metal phase transition.

2. SAMPLES AND EXPERIMENTAL PROCEDURE

The experimental samples of $Pr_{0.6}La_{0.1}Ca_{0.3}MnO_3$ consisted of thin films prepared by the MOCVD (Metal Organic Chemical Vapor Deposition) method. The films were deposited in inert gas from the initial vapors of volatile solutions at $T=860\,^{\circ}C$ on a substrate cut from $SrLaGaO_4$ or $SrTiO_3$ single crystals in the (001) plane. After deposition, the films obtained were annealed in oxygen gas for 0.5 h at the same temperature (the method is described in detail in Ref. 6). Secondary mass spectrometry was used to check the cationic composition and uniformity of the films. X-Ray investigations showed that the $Pr_{0.6}La_{0.1}Ca_{0.3}MnO_3$ films obtained are epitaxial and have no polycrystalline inclusions. The crystal lattice parameters obtained from the x-ray data are in good agreement with the parameters for the bulk materials with the same composition. The crystal structure of the films corresponds to the orthorhombic space group *Pnma*. The experimental films were about 350 nm thick and the substrate was about 0.5 mm thick. The film and substrate were rather transparent to visible light. Spectral investigations showed that the transmission of a film with a substrate for light with wavelength $\lambda=633$ nm is about 10% at low temperatures.

Two $Pr_{0.6}La_{0.1}Ca_{0.3}MnO_3$ films were investigated in the present work: film 1 deposited on a $SrLaGaO_4$ substrate and film 2 deposited on a $SrTiO_3$ substrate. The parameters of these films, specfically, their magnetization and electric conductivity, differ appreciably. Nonetheless, the temperature dependences of the magnetization and electric resistance and the dependences of these quantities on the external magnetic field are qualitatively the same. A magnetic field induced irreversible phase transition from an AFM-insulating into a FM-metallic state is observed in both films at temperatures $T<50$ K.

In the present work measurements of the magnetization and electric conductivity of two $Pr_{0.6}La_{0.1}Ca_{0.3}MnO_3$ films were performed in the absence of illumination and with the films illuminated by He–Ne laser light with wavelength $\lambda=633$ nm. The light flux density was about 0.1 W/cm^2. The magnetization of the films was measured using a MPMS-5 Quantum Design SQUID magnetometer with an optical insert (fiber-optic sample holder) for illuminating the sample during the measurements. A sample (film on a substrate) consisted of a disk approximately 3 mm in diameter. The magnetization measurements were performed in the temperature range $5\text{ K}<T<300$ K in fields up to 50 kOe. The magnetic field was oriented perpendicular to the surface of the film.

An optical helium cryostat was used to perform measurements of the temperature and field dependences of the electric resistance of the films. For film 1 the measurements were performed in the temperature range $25\text{ K}<T<300$ K in magnetic fields up to 30 kOe, oriented, just as in the magnetization measurements, perpendicular to the film surface. For film 2 the measurements were performed in the temperature range $25\text{ K}<T<250$ K in magnetic fields up to 10 kOe. In this case the field was oriented parallel to the film surface. The two-contact method was used to measure the resistance, since the resistance was quite high (ranging from 10^3 to 10^9 Ω). Two electrically conducting contacts consisting of silver paste and separated by 3 mm from one another were deposited on the film surface. The length of the contacts along the gap between them was also equal to 3 mm. A section of the sample lying between the electric contacts was illuminated to investigate the influence of light on the conductivity of the films.

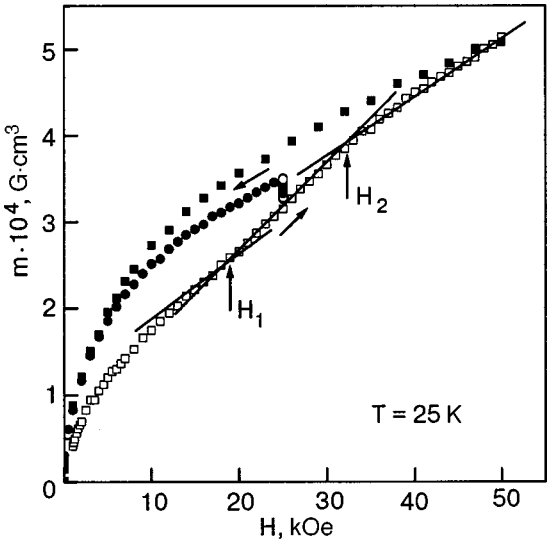

FIG. 1. Field dependences of the magnetization of film 1 at temperature $T=25$ K: in an unilluminated film (□ and ■); with illumination of the film in a constant external field $H=25$ kOe (○); in an illuminated film with the external field decreasing (●).

3. RESULTS OF THE MAGNETIC MEASUREMENTS

The measurements of the field dependences of the magnetization $m(H)$ in the absence of photoillumination showed that in $Pr_{0.6}La_{0.1}Ca_{0.3}MnO_3$ films a magnetic field induced phase transition from the AFM into the FM state is observed at temperatures $T<50$ K. The dependences $m(H)$ for films 1 and 2 are presented in Figs. 1 and 2, respectively. Figure 1 shows the function $m(H)$ (open squares) for film 1 at $T=25$ K; this curve was obtained after the sample was cooled from room temperature in the absence of a magnetic field (Zero-Field Cooling—ZFC). This first postcooling dependence was measured with the magnetic field increasing from 0 to 50 kOe. This curve, which is similar to the curve $m(H)$ obtained under the same conditions in a $Pr_{0.7}Ca_{0.3}MnO_3$ crystal,[7] is observed to have two breaks—one at $H_1\approx19$ kOe and one at $H_2\approx32$ kOe. The transition from the AFM into the FM state in film 1 occurs in the field range $19\text{ kOe}<H<32$ kOe. The function $m(H)$ measured with the magnetic field decreasing from 50 to 0 kOe (filled squares in Fig. 1) lies much higher on the plot and the reverse transition from the FM into the AFM state is not observed. When the field is subsequently increased from 0 to 50 kOe (with the magnetization of the film reversed beforehand to -50 kOe

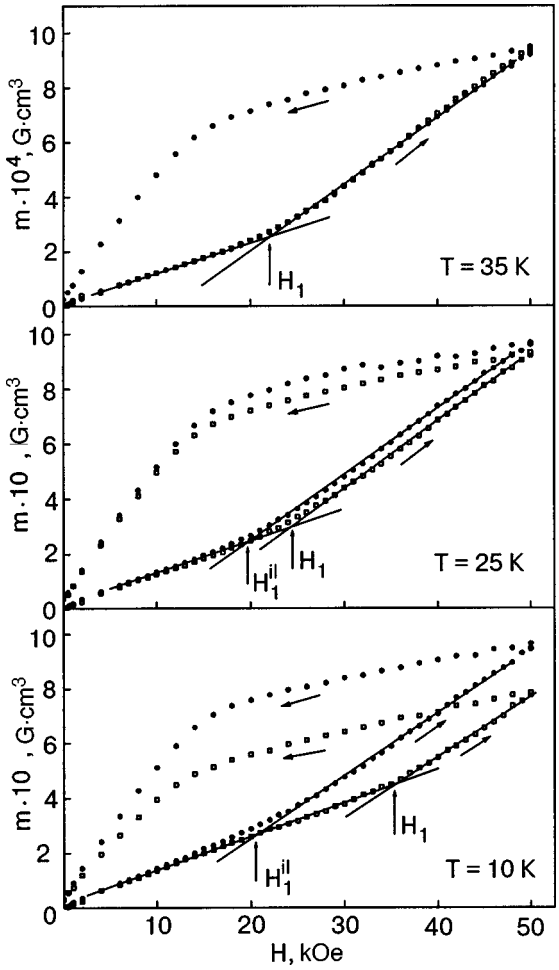

FIG. 2. Field dependences of the magnetization measured in film 2 at temperatures $T=10$, 25, and 35 K in unilluminated (□) and illuminated (●) films.

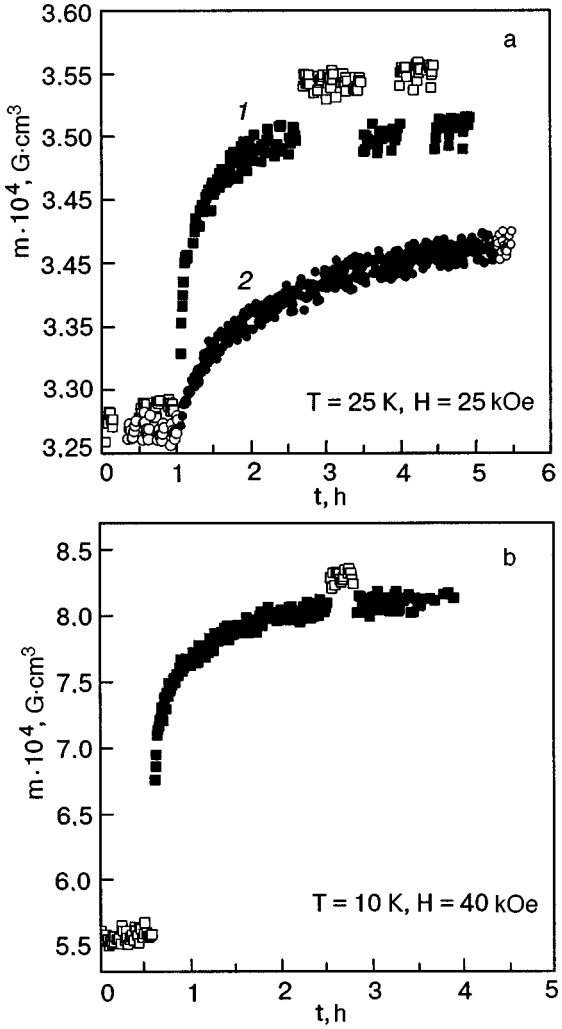

FIG. 3. Illumination time dependences of the magnetization of the films 1 (a) and 2 (b): open circles—without illumination, filled circles—with illumination. The dependences measured under illumination with linearly polarized (*1*) and unpolarized (*2*) light are shown for film 1.

or without magnetization reversal) the curve $m(H)$ is virtually identical to the curve obtained with the field decreasing from 50 to 0 kOe. Thus the magnetic field induced phase transition from the AFM into the FM state in the experimental $Pr_{0.6}La_{0.1}Ca_{0.3}MnO_3$ film is irreversible, just as in a $Pr_{0.7}Ca_{0.3}MnO_3$ crystal.[7,8]

The field dependences of the magnetization of film 2 are shown in Fig. 2. Just as in the case of film 1 a magnetic field induces in film 2 a phase transition from the AFM into the FM state when the magnetic field is applied for the first time after the sample is cooled in zero field from room temperature. However, the onset of the transition is observed in somewhat stronger magnetic fields. At $T=25$ K the break in the curve $m(H)$ corresponding to the field H_1 is observed at ≈ 25 kOe, while in film 1 at this temperature $H_1 \approx 19$ kOe. In addition, the completion of the transition (break in the function $m(H)$ at the field H_2) is not observed in film 2 right up to 50 kOe, i.e. the field interval $\Delta H = H_2 - H_2$ in this film was wider than in film 1. For the field decreasing from 50 to 0 kOe the curve $m(H)$, just as in the case of film 1, lies much higher and the curve $m(H)$ obtained with the field subsequently increasing from 0 to 50 kOe is virtually identical. Therefore the magnetic field induced transition from the AFM into the FM state is also irreversible even in the film 2.

Illuminating the experimental films with He–Ne laser radiation with wavelength $\lambda = 633$ nm in a magnetic field increased the magnetization and stimulated a phase transition from the AFM into the FM state. The experiments investigating the influence of light on the magnetization of the films and the phase transition from the AFM into the FM state were performed as follows. First, the film 1 was cooled in the absence of a magnetic field from room temperature to the temperature at which the measurements were performed (Fig. 1 shows the data for $T=25$ K). Next, the magnetic field was slowly increased to a value close to $(H_1+H_2)/2$ and the magnetization was measured as the field was increased. A 25 kOe external field (Fig. 1) corresponds to approximately the midpoint of the range H_1-H_2, where in film 1 a transition from the AFM into the FM state occurs at $T=25$ K. The sample was photoilluminated in this field. The magnetization of the film (open circles in Fig. 1) was observed to increase during illumination.

The kinetics of the photoinduced increase of the magnetization of film 1 is shown in Fig. 3a. As one can see from the dependence of the magnetization $m(H)$ on the illumination time, when the light is switched on ($t=1$ h) the magne-

tization of the film at first increases rapidly and then saturates. The influence of linearly polarized and unpolarized light on the magnetization of the experimental film was studied. The light flux density was the same in both cases. As one can see from Fig. 3a, in the first case the magnetization of the film as a function of the illumination time increases much more rapidly than for illumination with unpolarized light. The magnetization saturation time for illumination with polarized light was somewhat longer than 1 h. However, when the sample was illuminated with unpolarized light the photoinduced change of the magnetization did not saturate even after illumination for 4 h.

The increase of the magnetization of the film under illumination is not due to heating of the film by the light. The temperature dependence of the magnetization of film 1 in the FM state, where according to experiment there is no photoinduced change in magnetization, was used to determine the magnitude of the heating of the sample by laser light. For the initial sample temperature $T=25$ K illumination increases the temperature of the sample by 3–4 K. This temperature increase corresponds to a magnetization increase (see the ZFC dependence $m(H)$ in Fig. 4a) by 4×10^{-6} G·cm^3, which is almost an order of magnitude less than the observed photoinduced increase of magnetization (Fig. 3a). In addition, the temperature of the sample reaches an equilibrium value much more rapidly under illumination than the photoinduced change saturates. When the illumination was switched off after saturation was reached, a small increase of the magnetization of the film was observed (open squares in Fig. 3a); this is due to cooling of the sample. When the light was then switched on, resulting in the sample being heated, the magnetization rapidly returned to its previous value (filled squares in Fig. 3a).

As one can see in Fig. 1, the magnetization of the film under illumination does not reach the value corresponding to the FM phase in the field 25 kOe. However, its magnitude increases substantially under the action of the light. The field dependence of the magnetization, measured with the field decreasing from 25 to 0 kOe after illumination is switched off (filled circles in Fig. 1), lies on the plot much higher than the initial curve $m(H)$ obtained with the field increasing in the absence of illumination (open squares in Fig. 1). The dependence $m(H)$ measured with a subsequent increase of the field from 0 to 25 kOe in the absence of illumination is identical to the dependence obtained with decreasing field. Thus the photoinduced changes in the sample remain after the magnetic field is removed and appear when the field is reintroduced. The photoinduced transition into a different magnetic state in a $Pr_{0.6}La_{0.1}Ca_{0.3}MnO_3$ film is also irreversible, just as the magnetic field induced transition. No relaxation of the photoinduced change in magnetization was observed, to within the limits of the measurement error, over a period of 20 h after illumination was switched off.

We also note that a photoinduced increase of the magnetization was also observed in fields $H<H_1$, though the photoinduced change in this case is smaller than in the range of fields corresponding to the phase transition from the AFM into the FM state. The investigations of the film temperature dependence of the photoinduced change in magnetization

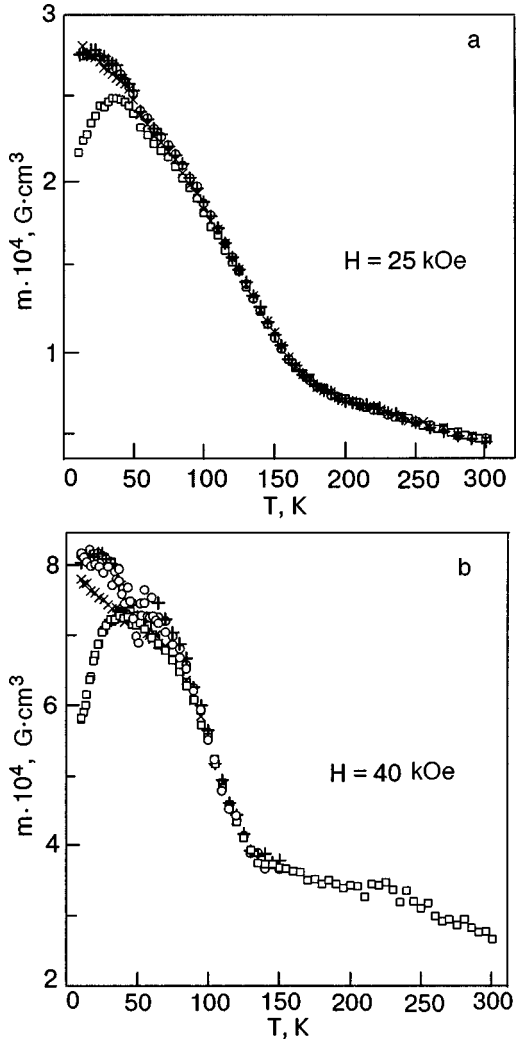

FIG. 4. Temperature dependences of the magnetization of the films 1 (a) and 2 (b) in the fields $H=25$ and 40 kOe, respectively: the ZFC and FC curves measured in unilluminated (□ and ×) and illuminated (film illuminated during the measurements and more than 1 h before the measurements) (○ and +) samples.

showed that the magnitude of the change increases as temperature decreases.

Similar photoinduced changes of the magnetic state of a sample were also observed in film 2. Figure 3b shows the dependence of the magnetization of this film on the time for which it was illuminated with linearly polarized light in a magnetic field $H=40$ kOe at temperature $T=10$ K. As one can see from the figure, the magnetization of film 2 increases under illumination, and the saturation time of the photoinduced change of magnetization is about 1.5 h. Therefore, in both films 1 and 2 photoillumination induced an increase of magnetization and stimulated a transition from the AFM into the FM state. The field dependences of the magnetization in a photoilluminated sample were measured for film 2. These dependences are presented in Fig. 2 (filled circles). Just as for measurements of the field dependences in an unilluminated film the sample was first cooled each time in zero field from room temperature to the measurement temperature. Then the film was photoilluminated for 1 h, after which the field dependence of the magnetization of the film was measured with illumination continuing in fields from 0 to 50 kOe

and from 50 to 0 kOe. As one can see in Fig. 2, the influence of photoillumination on the dependence $m(H)$ is virtually unnoticeable at $T=35$ K, is clearly seen at $T=25$ K, and increases strongly at $T=10$ K. The field H_1 in which the transition from AFM into the FM state starts decreases under the action of light. The shift of the field H_1 in the illuminated film as compared with the unilluminated film is 5 kOe at $T=25$ K and about 15 kOe at $T=10$ K, i.e. the quantity $H_1^{il}-H_1$ increases appreciably as temperature decreases.

The influence of photoillumination on the temperature dependences of the magnetization $m(H)$ of $Pr_{0.6}La_{0.1}Ca_{0.3}MnO_3$ films was also taken into account. The dependences $m(H)$ for the films 1 and 2 were measured in a magnetic field with sample, heating of the sample, which was precooled from room to liquid-helium temperature in the absence of a field or in a magnetic field in which the measurements were then performed (field cooling—FC). Figure 4 shows the ZFC and FC temperature dependences of the magnetization of the films 1 (Fig. 4a) and 2 (Fig. 4b), measured in the fields $H=25$ kOe and 40 kOe, respectively. The difference between the ZFC and FC dependences in the unilluminated films is clearly observed at temperatures $T<50$ K for film 1 and $T<40$ K for film 2 and is due to the existence of a nonuniform magnetic state containing AFM and FM phases in the sample. Figure 4 also shows the ZFC and FC temperature dependences of the magnetization for illuminated films. The films were illuminated at $T=10$ K and $H=25$ kOe by linearly polarized light at least 1 h before the magnetization measurements and during the measurements. As one can see in Fig. 4, the ZFC and FC dependences for the illuminated film 1 are indistinguishable from one another and are identical to the FC dependence of the magnetization measured for the unilluminated film. For the illuminated film 2 the ZFC and FC dependences are also the same and lie even farther above the FC dependences for the unilluminated film. The results obtained additionally confirm that illumination with He–Ne laser light stimulates a phase transition from the AFM into the FM state in $Pr_{0.6}La_{0.1}Ca_{0.3}MnO_3$ films. A difference in the temperature dependences of the magnetization between the illuminated and unilluminated films is observed at $T<50$ K for film 1 (ZFC dependence) and $T<80$ K for film 2 (ZFC and FC dependences). We note that the photoinduced change in the ZFC magnetization cannot be explained by heating of the sample. Heating can cause the ZFC magnetization to reach only its maximum value, which is less than the magnetization of illuminated films at $T<50$ K. For film 2 the ZFC and FC curves both lie above the FC dependence of an unilluminated film. Heating of the sample cannot produce such a result.

4. RESULTS OF RESISTANCE MEASUREMENTS

A phase transition from the AFM insulator into the FM metallic state and the influence of photoillumination on this transition were also observed when we studied the electric conductivity of $Pr_{0.6}La_{0.1}Ca_{0.3}MnO_3$ films in a magnetic field at temperatures $T<50$ K. The current–voltage characteristics of the experimental films were nonlinear. It is well known that the applied electric field arising in a $Pr_{0.6}La_{0.1}Ca_{0.3}MnO_3$ film when measuring the electric conductivity itself can give rise to a phase transition from the insulating into the metallic state.[9] Measurements of the temperature and field dependences $R(T)$ and $R(H)$ were performed in a regime with a prescribed voltage. This voltage was adjusted experimentally to the lowest value sufficient to ensure measurement accuracy and was 0.5 V. The electric resistance of both experimental films was approximately the same at room temperature ($\approx 2\times 10^3$ Ω) and strongly increased with decreasing temperature. Figure 5 shows the curves $R(T)$ for the films 1 (Fig. 5a) and 2 (Fig. 5b), measured with the films being cooled. The time over which the temperature drops from room temperature to 25 K varied from 45 min to 4 h. No effect of the rate of cooling on the electric state of the sample was observed. According to Fig. 5, as temperature decreases, the resistance of the films increases smoothly, and a sharp increase of resistance is observed at temperatures 100–110 K. It could be that the break observed in the curve $R(T)$ for both films near 100 K is due to AFM ordering. At low temperatures the resistances of films 1 and 2 differ substantially from one another. The resistance of film 1 reaches $\sim 10^6$ Ω, while the resistance of film 2 is several orders of magnitude greater, 10^9–10^{10} Ω. At low temperatures ($T<50$–70 K) the electric resistance of the films is not single-valued. For example, at $T=25$ K the resistance of film 1 with several coolings was in the range

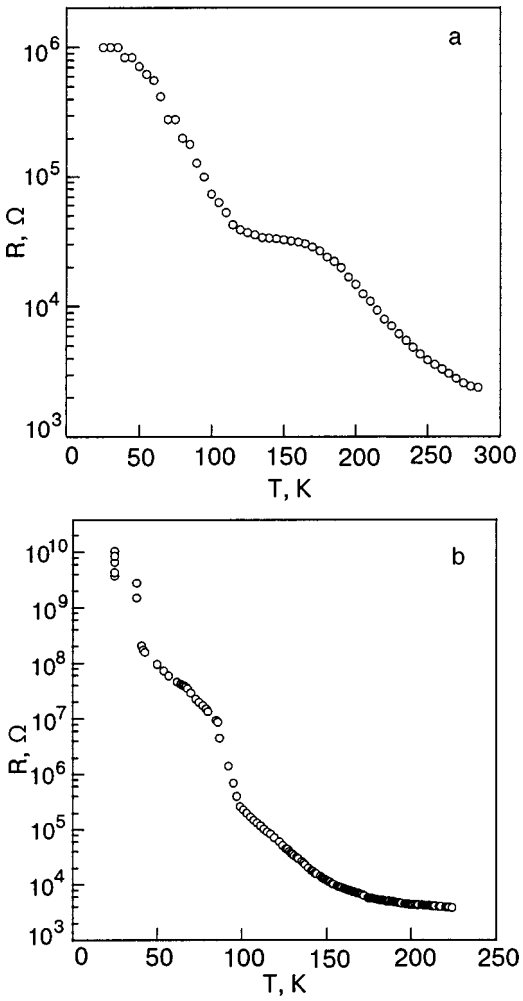

FIG. 5. Temperature dependences of the electric resistance of films 1 (a) and 2 (b).

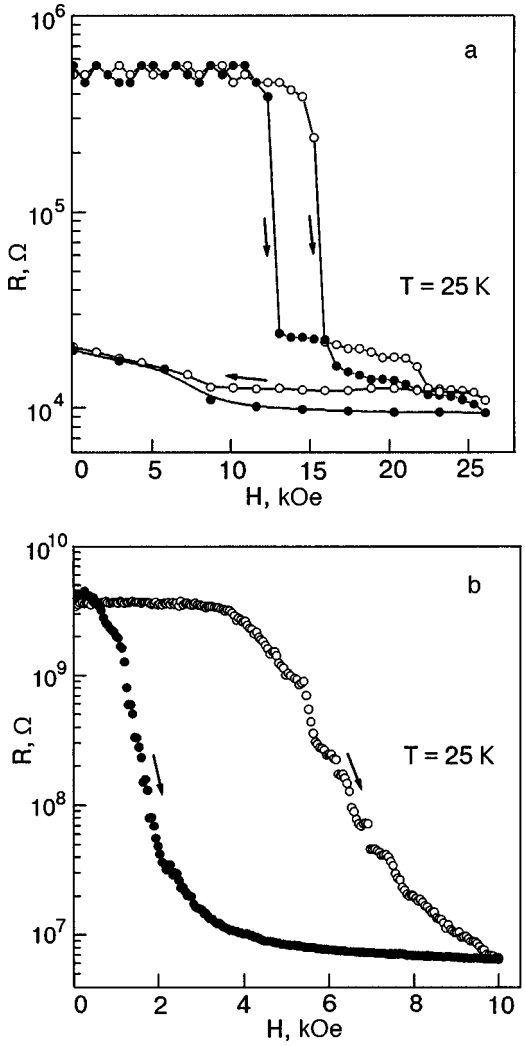

FIG. 6. Field dependences of the electric resistance of films 1 (a) and 2 (b) measured at $T=25$ K in unilluminated (○) and illuminated (●) films.

$5\times10^5-2\times10^6$ Ω, and the resistance of film 2 was in the range $4\times10^9-1\times10^{10}$ Ω. It should be noted that the error in the measurements of the resistance of the second film was high for $R>10^8$ Ω. This could be due to the jumps in the curve $R(T)$ and the large scatter of the points. Consequently, for $R>10^8$ Ω only qualitative judgments can be made about the temperature variation of the resistance of film 2.

The magnetic field dependences obtained for the electric resistance of films 1 and 2 in unilluminated and illuminated films are presented in Fig. 6. These dependences were measured with the magnetic field switched on for the first time after the films were cooled in the absence of a field from room temperature to the measurement temperature. It is interesting that an AFM-insulator—FM-metal transition appears in the curves $R(H)$ (Fig. 6) in weaker fields and is sharper than in the curves $m(H)$ (Figs. 1 and 2). Thus for film 1 in the absence of illumination the transition is observed in the curve $R(H)$ at $T=25$ K in the fields $H_1\approx14.5$ kOe and $H_2\approx16.5$ kOe (Fig. 6a), while in the curves $m(H)$ at the same temperature (Fig. 1) the transition occurs in the fields $H_1\approx19$ kOe and $H_2\approx32$ kOe. For the film 2 with no illumination the transition in the curve $R(H)$ at $T=25$ K starts in the field $H_1\approx3.6$ kOe and is essentially complete in the field $H_2\approx10$ kOe (Fig. 6b), while in the curve $m(H)$ at the same temperature (Fig. 2) the transition starts at $H_1\approx25$ kOe and is still incomplete at 50 kOe. The observed difference in the magnetic and resistance measurements is probably due to the presence in the sample, in the case where $R(H)$ is measured, of an electric field which itself can give rise to a phase transition from the insulating into the metallic state.[9] The combined effect of electric and magnetic fields on the electronic and magnetic subsystems of the crystal for resistance measurements is that the phase transition occurs in weaker external magnetic fields.

As the magnetic field decreases, the reverse transition from the metallic into the insulating state is not observed (Fig. 6a; in Fig. 6b the reverse variation of the field is not shown). Thus the resistance measurements, just as the magnetic measurements, show that the magnetic field induced AFM-insulator—FM-metal transition is irreversible.

Experiments measuring the electric resistance in illuminated $Pr_{0.6}La_{0.1}Ca_{0.3}MnO_3$ films showed, just as the magnetic measurements, that illuminating films with He–Ne laser light with $\lambda=633$ nm appreciably decreases the magnetic field in which a transition from the insulating into the metallic state is observed. Prior to illumination the film was cooled in the absence of a field from room temperature to the measurement temperature. After the required temperature was established, the film was illuminated at $H=0$ for 1 h, and then the dependence $R(H)$ was measured. Illumination of the film continued during the measurements of the field dependence. As we can see from Figs. 6a and 6b, at $T=25$ K photoillumination shifts the AFM-insulator—FM-metal transition in the direction of weak fields by ~3 kOe for film 1 and ~4 kOe for film 2. A photoinduced decrease of the transition fields was observed in experiments measuring the electric resistance at temperatures $T<50$ K. It should be noted that after a film is illuminated its resistive properties returned to the initial state observed before illumination only after the sample was heated to room temperature and held at this temperature for one day.

The kinetics of the photoinduced change in the electric resistance of films is shown in Fig. 7. In experiments studying the kinetics the magnitude of the external magnetic field was set in the range $H_1^{il}<H<H_1$, where H_1^{il} and H_1 are the fields in which a transition at a prescribed temperature from the insulating into the metallic state starts in illuminated and unilluminated films, respectively. The resistance of an unilluminated film was measured for several minutes and then photoillumination was switched on at the time marked by the arrow in Fig. 7. As one can see from Fig. 7a, after film 1 was illuminated for about 1 min its resistance abruptly dropped by almost an order of magnitude. The observed photoinduced decrease of R is close in magnitude to the decrease of the resistance of film 1 at a phase transition induced by a magnetic field (Fig. 6a). In film 2 the photoinduced phase transition is slower (Fig. 7b). The resistance of the film decreases by three orders of magnitude under the action of light; this agrees well with the decrease of R at a magnetic field-induced transition (Fig. 6b). We note that for film 2, just as for film 1, the photoinduced change of the electric resistance occurs much more quickly (Fig. 7) than the change of magnetization (Fig. 3).

Just as in the investigation of the influence of light on

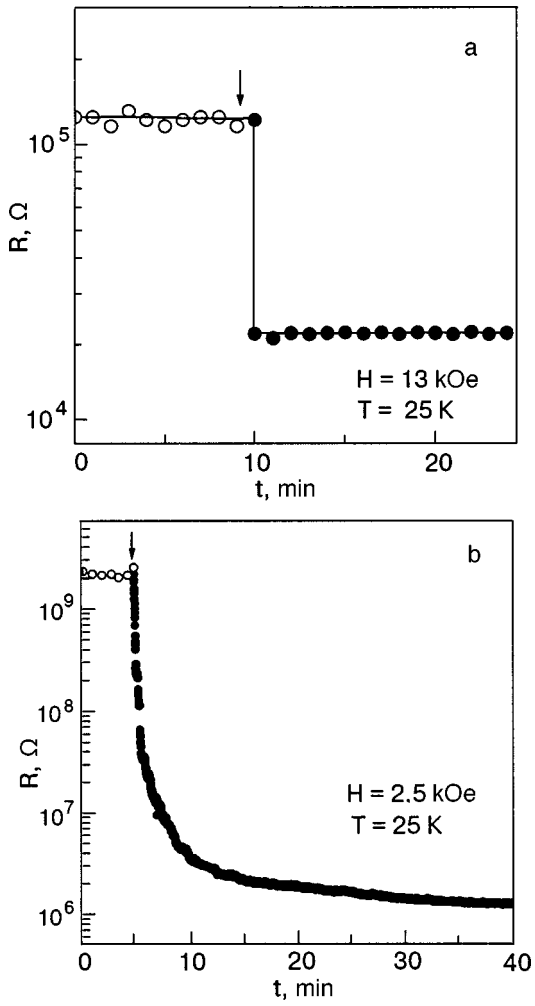

FIG. 7. Illumination-time dependences of the electric resistance of films 1 (a) and 2 (b). Open circles—without illumination; filled circles—with illumination. The arrows mark the moment when the illumination is switched on.

the magnetic properties of $Pr_{0.6}La_{0.1}Ca_{0.3}MnO_3$ films, in the investigation of the influence of illumination on the resistance properties of the same films a check was made to see that the observed photoinduced changes are not due to trivial heating of the sample. To this end the temperature dependence of the resistance of film 1 in the metallic state, in which no photoinduced changes in R are observed, was measured. This dependence was measured in the absence of a magnetic field, which when applied beforehand induced an irreversible insulator–metal transition. The temperature dependence $R(T)$ obtained can be used to determine the amount of heating of the film by the laser radiation. It was found that for initial sample temperature $T=25$ K illumination increases the temperature of the film by not more than 3 K. We note that virtually the same change of the film temperature by 3–4 K was also observed under the action of light during the magnetic measurements. An increase of the film temperature by 3 K cannot shift the phase transition toward weaker fields by the amount ~ 3 kOe, which is observed experimentally (Fig. 6a). According to the $H-T$ phase diagram obtained for film 1 from the resistance measurements with $U=0.5$ V, the temperature of the film must reach 40 K for such a shift of the phase transition to occur, i.e. the light must heat the sample by 15 K.

5. DISCUSSION AND CONCLUSIONS

The following conclusions can be drawn from the present investigations of the influence of photoillumination on the magnetic and resistance properties of $Pr_{0.6}La_{0.1}Ca_{0.3}MnO_3$ films and the magnetic field induced transition from the AFM-insulating into the FM-metallic state observed in these films.

—Illumination of $Pr_{0.6}La_{0.1}Ca_{0.3}MnO_3$ films with $\lambda = 633$ nm visible light in a magnetic field at temperatures $T<50$ K increases the magnetization and decreases the electric resistance of the films and stimulates a transition from the AFM-insulating into the FM-metallic state. In the illuminated films the magnetic field induced transition from the AFM-insulating into the FM-metallic state occurs in weaker external fields than in unilluminated films.

—The photoinduced AFM-insulator—FM-conductor transition is irreversible. The photoinduced changes in the state of the manganite $Pr_{0.6}La_{0.1}Ca_{0.3}MnO_3$ remain after the magnetic field is removed and appear after the field is restored with no changes from the form in which they were observed after the film was illuminated in a magnetic field. Relaxation of the photoinduced changes of magnetization and electric resistance is not observed. It should be noted that photoilluminating $Pr_{0.6}La_{0.1}Ca_{0.3}MnO_3$ films in the absence of a magnetic field does not produce any changes in the magnetization and electric resistance of the films either directly during illumination or when the magnetic field is subsequently switched on after illumination is switched off.

—Under identical conditions the photoinduced change of the electric resistance saturates much more quickly than the photoinduced change of magnetization. Apparently, the presence of an electric field in the manganite $Pr_{0.6}La_{0.1}Ca_{0.3}MnO_3$ films accelerates the process producing the photoinduced changes.

—Linearly polarized light gives rise to a transition from the AFM-insulating into the FM-metallic state much more quickly than unpolarized light under the same conditions.

The effect of light on the magnetic and resistance properties of $Pr_{0.6}La_{0.1}Ca_{0.3}MnO_3$ films could be due to the nonuniform state of manganite. It is known that the appearance of phase separation is characteristic for manganites. At low temperatures regions with the FM-metallic phase exist in $Pr_{0.6}La_{0.1}Ca_{0.3}MnO_3$ films together with the AFM-insulating phase. The difference of the ZFC and FC temperature dependences of magnetization at temperatures $T<50$ K attests to the nonuniform state of the crystal. The presence of a FM phase is seen in the nonlinear dependence of the magnetization in weak fields for film 1 (Fig. 1). In film 2, where the dependence $m(H)$ in weak fields is linear (Fig. 2), the number of FM-metallic clusters is smaller than in film 1. Low-temperature observations of the much higher (by 3–4 orders of magnitude at $T=25$ K) resistance of film 2 than film 1 (Fig. 5) confirm this.

Photo-illumination of manganite could result in the formation of new and growth of existing FM-metallic clusters inside the AFM-insulating phase.[2–4] A photoinduced increase in the concentration of the FM-metallic phase in the crystal

increases the magnetization and decreases the electric resistance. Thus light stimulates a phase transition from the AFM-insulating into the FM-metallic state and shifts the transition to weaker magnetic fields. It follows from the magnetic measurements that photoillumination results in a transition only of a portion of the antiferromagnetic phase into the ferromagnetic phase. Even after the photoinduced effect saturates the magnetization is less than the magnetization corresponding to the dependence $m(H)$ measured with H decreasing from 50 to 0 kOe (Fig. 1). At the same time the electric resistance of $Pr_{0.6}La_{0.1}Ca_{0.3}MnO_3$ films decreases under the action of light to the same value (Fig. 7) as for a phase transition induced by a magnetic field (Fig. 6). This can be explained by taking account of the fact that for a transition of a part of the crystal into the FM-metallic state a percolation cluster penetrating through the entire film can arise,[10–12] and from this moment on the sample will exhibit metallic conductivity. At the same time a substantial portion of the film can remain in the AFM insulating state. Subsequent photoillumination of manganite can result in the appearance of new and growth of existing FM-metallic clusters inside the remaining AFM-insulating phase and, correspondingly, an increase in the concentration of the FM phase and the magnetization. In the process the resistance properties of the film can change only negligibly, because the conductivity is determined by the existing percolation cluster. Such a model explains the experimentally observed more rapid saturation of the photoinduced change in the electric resistance as compared with the photoinduced change in the magnetization. The appearance of a percolation cluster can also explain the observed sharper AFM-insulator—FM-metal transition in the dependences $R(H)$ (Fig. 6), while in the dependences $m(H)$ (Figs. 1 and 2) this transition occurs in a wider range of fields.

The presence of an electric field in the sample at the time the resistance properties of the films are studied also probably influences the phase transition from the AFM-insulating into the FM-metallic state. It can give rise to a transition in the AFM-insulating regions lying between the FM-metallic clusters and thereby facilitate the formation of a percolation cluster. Thus the presence of an electric field can also result in a sharper phase transition and rapid saturation of the photoinduced change of the electric resistance.

As noted above, relaxation of the photoinduced changes of magnetization and electric resistance was not observed experimentally. The photoinduced transition from the AFM-insulating into the FM-metallic state is irreversible. It could be that the nonuniform state existing in a magnetic field and consisting of regions of an AFM-insulating phase and a FM-metallic phase is unstable. A photoinduced transition of a portion of the AFM-insulating into the FM-metallic phase changes the concentration of the phases and transfers the crystal into a more stable state. After the light is switched off the manganite film is in a more stable state and consequently relaxation is not observed. If this supposition is correct, we arrive at the conclusion that the state of the crystal arising when the crystal is cooled from room temperature to the measurement temperature in the absence of a magnetic field is stable and consequently does not change under illumination.

On the other hand the relaxation time of the photoexcited state can be very long, so that relaxation is not observed during the experiment for several hours (relaxation was not detected for 20 h in an experiment investigating the photoinduced change of magnetization). In a $Pr_{0.7}Ca_{0.3}MnO_3$ crystal the transition time from the metallic into the insulating state after the magnetic field was switched off was about 3 h at $T=40$ K.[13] In addition, this time increased by two orders of magnitude as temperature decreased from 45 to 40 K. It could be that in our experiments at lower temperatures the relaxation time is many orders of magnitude longer.

The effect of light on the phase transition studied in manganite films could be due to the photoinduced transfer of electrons from Mn^{3+} to Mn^{4+} ions. The transfer of an electron e_g from Mn^{3+} to Mn^{4+} through the O_{2p} orbital of oxygen occurs under the action of light.[1] A change in the valence of Mn ions can result in melting of the charge ordering, which occurs in the AFM-insulating state, and give rise to a transition into the FM-metallic phase. It could be that linearly polarized light induces directed charge transfer between Mn^{3+} and Mn^{4+} ions in the crystal lattice; this gives rise to a more rapid rearrangement of the electronic, magnetic, and structural states of the crystal. This can explain the experimentally observed more rapid process of photoinduced changes under the action of polarized light as compared with unpolarized light.

This work was partially performed under project No. 3-026/2004 of the Ukrainian National Academy of Sciences.

*E-Mail: vgapon@ilt.kharkov.ua

[1] J. M. Dai, W. H. Song, J. J. Du, J. N. Wang, and Y. P. Sun, Phys. Rev. B **67**, 144405 (2003).
[2] K. Miyano, T. Tanaka, Y. Tomioka, and Y. Tokura, Phys. Rev. Lett. **78**, 4257 (1997).
[3] T. Mori, K. Ogawa, K. Yoshida, K. Miyano, Y. Tomioka, and Y. Tokura, J. Phys. Soc. Jpn. **66**, 3570 (1997).
[4] K. Ogawa, W. Wei, K. Miyano, Y. Tomioka, and Y. Tokura, Phys. Rev. B **57**, R15033 (1998).
[5] M. Baran, S. L. Gnatchenko, O. Yu. Gorbenko, A. R. Kaul, R. Szymczak, and H. Szymczak, Phys. Rev. B **60**, 9244 (1999).
[6] O. Yu. Gorbenko, A. R. Kaul, N. A. Babushkina, and L. M. Belova, J. Mater. Chem. **7**, 747 (1997).
[7] Y. Tomioka, A. Asamitsu, Y. Moritomo, and Y. Tokura, J. Phys. Soc. Jpn. **64**, 3626 (1995).
[8] T. Tomioka, A. Asamitsu, H. Kuwahara, Y. Moritomo, and Y. Tokura, Phys. Rev. B **53**, R1689 (1999).
[9] A. Asamitsu, Y. Tomioka, H. Kuwahara, and Y. Tokura, Nature (London) **388**, 50 (1997).
[10] É. L. Nagaev, Usp. Fiz. Nauk **166**, 833 (1996).
[11] L. P. Gor'kov, Usp. Fiz. Nauk **168**, 665 (1998).
[12] V. M. Loktev, Fiz. Nizk. Temp. **26**, 231 (2000) [Low Temp. Phys. **26**, 171 (2000)].
[13] A. Anane, J. P. Renard, L. Reversat, C. Dupas, P. Veillet, M. Viret, L. Pinsard, and A. Revcolevschi, Phys. Rev. B **59**, 77 (1999).

Translated by M. E. Alferieff

Manifestation of noncentrality in the EPR spectrum of Fe^{3+} in polycrystalline substances

V. N. Vasyukov and V. V. Chabanenko*

A. A. Galkin Physicotechnical Institute, Ukrainian National Academy of Sciences, ul. R. Lyuksemburg 72, Donetsk 83114, Ukraine

R. O. Kochkanyan and M. M. Nechitaĭlov

L. M. Litvinenko Institute of Physical-Organic Chemistry and Coal Chemistry, Ukrainian National Academy of Sciences, ul. R. Lyuksemburg 70, Donetsk 83114, Ukraine

A. Nabyalek, S. Piechota, and H. Szymczak

Institute of Physics, Polish Academy of Sciences, 32/46, Al. Lotnikow 32/46, 02-668 Warsaw, Poland
(Submitted April 6, 2004; revised July 7, 2004)
Fiz. Nizk. Temp. **30**, 1272–1278 (December 2004)

The EPR spectrum of an impurity Fe^{3+} ion in three organic substances is investigated in the temperature range 4.2–295 K: bromocresol green ($C_{21}H_{14}Br_4O_5S$), crystal violet ($C_{25}H_{30}ClN_3$), and a compound of crystal violet with fullarene (($C_{25}H_{30}ClN_3$)+C_{60}). An unusual change in the shape of the EPR spectrum as a function of temperature is observed in all substances investigated. At 4.2 K the spectrum is a superposition of three contributions: two resonance lines with effective g factors $g_1=4.39$ and $g_2=2.03$ and a nonresonance contribution. As the temperature changes, the intensities become redistributed between these three contributions. As temperature increases, the total intensity of line *1* and the nonresonance contribution decrease and the intensity of line *2* increases. The observed properties of the EPR spectra are characteristic for noncentral ions which possess a multiple-minimum potential. The redistribution of the populations of vibronic states of a noncentral Fe^{3+} ion determines the temperature variation of the EPR spectrum. © *2004 American Institute of Physics.*
[DOI: 10.1063/1.1820034]

An unusual temperature dependence of the EPR spectrum of the Fe^{3+} ion has been observed in a number of organic and mineral substances.[1–7] The main feature of the EPR spectrum in these substances is the existence of two resonance lines whose intensities behave oppositely as a function of temperature. As temperature decreases, the intensity of one line increases and the intensity of the other decreases, and one line is stronger at low (liquid-helium) temperatures and the other is strong at high (room) temperatures. The first line was determined to be the low-temperature (LT) component of the EPR spectrum and the second line the high-temperature (HT) component. A change in temperature causes the absorption intensity to be redistributed between the LT and HT components of the spectrum. Such behavior of the EPR spectrum attests to an unusual dynamics of the molecules surrounding the Fe^{3+} ion or of the iron ion itself. The existence of this dynamics could have a large effect on various properties of substances containing Fe^{3+} ions.

The investigation of dynamical transitions is of interest in itself, because the magnetic centers manifesting such properties possess, as a rule, a multiple-minimum potential. Such magnetic centers have not been adequately studied experimentally. They all have the property that the motion determining the transition from the LT to the HT spectrum occurs in a potential well with several minima separated by a potential barrier. Magnetic centers with a multiple-minimum potential can have a different physical nature. Magnetic centers whose multiple-minimum potential is due to the Jahn–Teller effect have been studied in greatest detail. The Fe^{3+} ion is a S ion, and for this reason the Jahn–Teller effect is impossible. It is more likely that the properties of the Fe^{3+} ion which were observed in Refs. 1–7 are a manifestation of its noncentral (off-center) positioning.[8]

The behavior of a noncentral magnetic ion is manifested as characteristic features in the EPR spectrum: the presence of LT and HT components of the EPR spectrum and intensity redistribution between the LT and HT components of the spectrum as temperature changes.

The EPR spectra of a Fe^{3+} ion in the substances investigated in Refs. 1–7 exhibit the same general properties but also large differences. The general properties of the EPR spectra of these substances are due to the fact that the Fe^{3+} ion occupies noncentral positions. The difference in the shape of the spectra is due to the individual features of the magnetic centers. One such feature is the existence of nonresonance absorption in the EPR spectrum, whose intensity and shape depend on the temperature. In the present work, to study the manifestation of these differences the EPR spectra of the magnetic centers of a Fe^{3+} ion were investigated in three different organic substances: bromocresol green ($C_{21}H_{14}Br_4O_5S$), crystal violet ($C_{25}H_{30}ClN_3$), and a compound of crystal violet with fullarene (($C_{25}H_{30}ClN_3$) +C_{60}). The shape of the EPR spectrum of the Fe^{3+} ion in these substances is very different. This makes it possible to

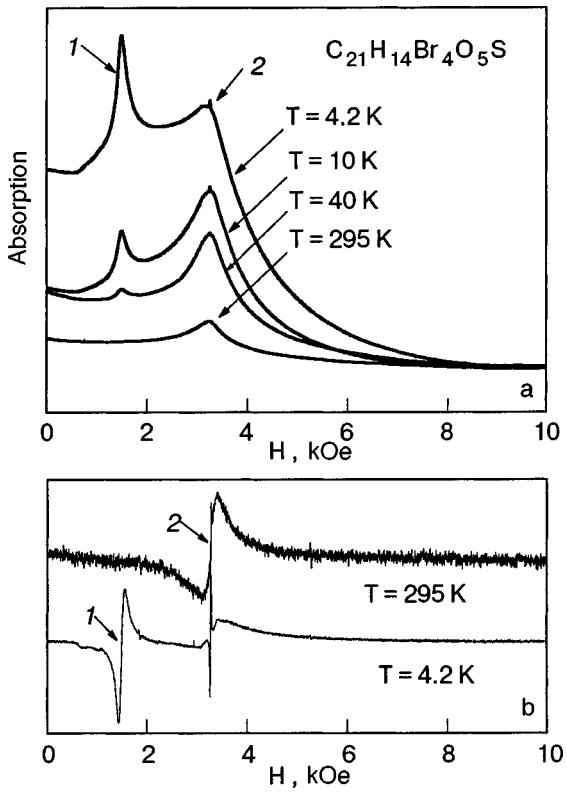

FIG. 1. EPR spectra of an Fe^{3+} ion in $C_{21}H_{14}Br_4O_5S$. The shape (a) and derivatives (b) of the absorption lines at various temperatures.

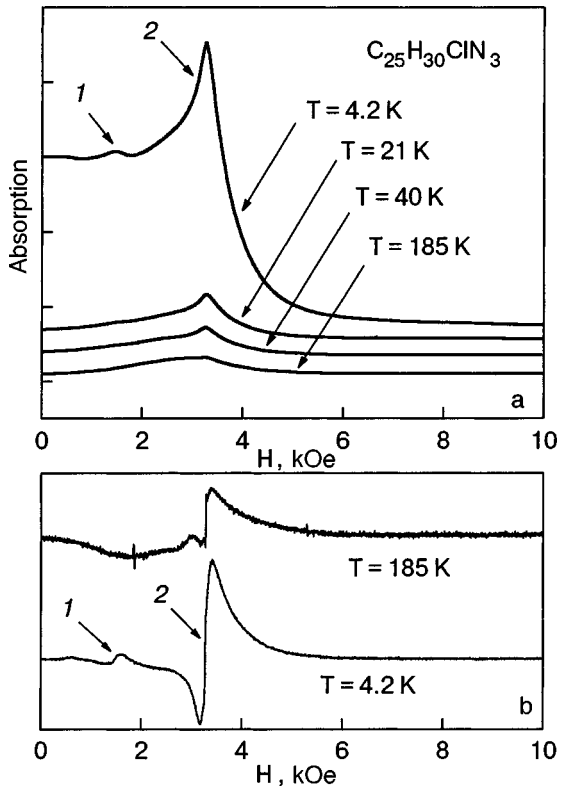

FIG. 2. EPR spectra of an Fe^{3+} ion in $C_{25}H_{30}ClN_3$. The shape (a) and derivatives (b) of the absorption lines at various temperatures.

demonstrate different manifestations of ''noncentrality.''

To obtain the compound $(C_{25}H_{30}ClN_3)+C_{60}$ a mixture consisting of 50 mg of fullarene C_{60} (99.5% purity) and 58.3 mg crystal violet (1:2 molar ratio) was heated in argon gas at a rate of 5 °C/min up to the temperature 105 °C. When cooled, the eutectic mixture formed at this temperature congeals into a uniform free-flowing mass.

1. EXPERIMENTAL RESULTS

The EPR spectrum was investigated in the temperature range $T=4.2-295$ K using a 3-cm EPR spectrometer with a H_{012} square cavity with microwave frequency $\nu=9.241\pm0.001$ GHz.

Figures 1–3 show the EPR spectra of the experimental substances at several temperatures. The absorption lines (Figs. 1a–3a) were obtained by numerically integrating the experimental EPR spectra, some of which are presented in Figs. 1b–3b. The EPR data presented in Figs. 1–3 show that the spectra of all three substances contain two resonance lines whose parameters and behavior as a function of temperature are similar to those of the resonance lines of the substances described in Refs. 1–7. For $C_{21}H_{14}Br_4O_5S$ the resonance line *1* at $T=4.2$ K is described by the effective g factor $g_1=4.39\pm0.03$. For the complexes $C_{25}H_{30}ClN_3$ and $(C_{25}H_{30}ClN_3)+C_{60}$ the g factors are $g_1=4.5\pm0.1$ and $g_1=4.3\pm0.3$, respectively. The effective g factor $g_2=2.03\pm0.02$ describes the resonance line *2* for $C_{21}H_{14}Br_4O_5S$ at 295 K. For $C_{25}H_{30}ClN_3$ $g_2=2.15\pm0.15$ at $T=185$ K. According to Fig. 3a, for the complex $(C_{25}H_{30}ClN_3)+C_{60}$ the transition to a resonance line with the effective g factor $g_2\approx2.0$ is still not complete at 295 K.

Figures 1a–3a show that the EPR spectra of the experimental substances differ substantially. The main difference is the intensity ratio of the lines *1* and *2*. For bromocresol green

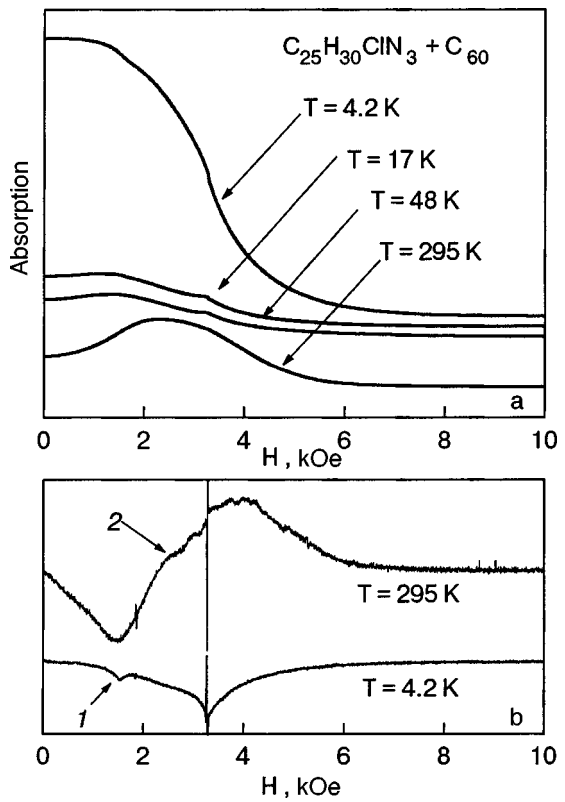

FIG. 3. EPR spectra of an Fe^{3+} ion in $(C_{25}H_{30}ClN_3)+C_{60}$. The shape (a) and derivatives (b) of the absorption lines at various temperatures.

the line *1* is stronger than the line *2*. Conversely, the line *2* is stronger for $C_{25}H_{30}ClN_3$. For the third substance (Fig. 3a) at $T=4.2$ K neither resonance line is observed at all, making it impossible to talk about their intensity ratio. Nonetheless, the resonance lines *1* and *2* do exist. The spectra in the form of the derivative of the absorption line show this (see Fig. 3b). The line *1* is not observed in the EPR spectrum of the complex $(C_{25}H_{30}ClN_3)+C_{60}$ against the strong nonresonance background contribution to the spectrum. A nonresonance contribution is present in the EPR spectra of all experimental substances.

Before analyzing the temperature dependence of the resonance lines in the spectrum and the nonresonance contribution we call attention to the fact that two mechanisms for the temperature dependence of the spectrum can be distinguished. The first mechanism is conventional. It decreases the total intensity of all contributions to the EPR spectrum. The relation $I(T)=I_0\tanh(h\nu/2kT)$ describes this decrease of the intensity. The second mechanism for the temperature dependence is due to the multiple-minimum nature of the potential of the magnetic center and is manifested as a redistribution of intensity between the various contributions to the EPR spectrum. Dividing the total intensity shown in Figs. 1a–3a by $\tanh(h\nu/2kT)$ gives the reduced total intensity and the temperature variation of the absorption line shape which is due only to the second mechanism for the temperature dependence of the EPR spectrum.

According to Figs. 1a–3a, the intensity redistribution is characteristic for all three substances but is sharpest for $C_{21}H_{14}Br_4O_5S$. At 4.2 K the EPR spectrum of these substances can be represented as a superposition of three contributions: two resonance lines (*1* and *2*), whose parameters are similar to those of the lines described in Refs. (1–7), and a nonresonance contribution to the EPR spectrum. The intensity ratios of all three contributionsin the EPR spectra of the experimental substances are substantially different. The total intensity of all contributions is temperature dependent. At $T=4.2$ K the intensity of the nonresonance contribution is much higher than the total intensity of both resonance lines. As temperature increases, the reduced total intensities of the nonresonance contribution and line *1* decrease while the intensity of line *2* increases. At room temperature the total intensity of the line *1* is zero for all three experimental substances. For $C_{21}H_{14}Br_4O_5S$ and $C_{25}H_{30}ClN_3$ the intensity of line *2* is higher than that of the nonresonance contribution, but for the complex $(C_{25}H_{30}ClN_3)+C_{60}$ the intensity of line *2* is comparable in order of magnitude to that of the nonresonance contribution.

A temperature change changes not only the total intensity of the nonresonance contribution but also the form of the contribution. As temperature increases, the intensity of the low-field part of the nonresonance contribution decreases more rapidly than that of the high-field part. This change in form is similar to the intensity redistribution between the nonresonance contribution and the resonance line *2*.

It should be noted that the temperature dependence of the nonresonance contribution is similar to that of the resonance line *1*. The total intensities of the nonresonance contribution and the resonance line *1* reach their maximum values at low temperatures. As temperature increases, the intensities of both contributions decrease. At room temperature the intensity of the line *1* is zero, and the intensity of the nonresonance contribution reaches its minimum value. This kind of correlation in the temperature dependence of the contributions to the EPR spectrum suggests that the origin of all three contributions is of the same nature and is due to the Fe^{3+} ion.

2. DISCUSSION

1. The EPR spectra of the substances studied in the present work contain two resonance lines (Figs. 1–3) with effective g factors $g_1\approx 4.3$ and $g_2\approx 2$. The lines in the EPR spectrum with such g factors are characteristic for Fe^{3+} ions in a polycrystalline substance. Different reasons for the simultaneous observation of resonance lines with g factors $g\approx 2$ and $g\approx 4.3$ are examined in Refs. 5 and 9. The temperature variation of the shape of the EPR spectrum of a noncentral iron ion in polycrystalline substances is investigated theoretically in Ref. 5. The analysis in Ref. 9 of the results of an investigation of the EPR spectra of iron ions in silicate glasses suggested that the resonance lines with these g factors in silicate glasses belong to different magnetic centers. The difference between the centers is that the magnitude of the low-symmetry component of the crystal field acting on a magnetic ion is different. The line with $g\approx 2$ corresponds to a center whose low-symmetry component of the crystal field is much less than the Zeeman energy. The initial splitting parameter D in the spin Hamiltonian satisfies the condition $D\ll h\nu$, where $h\nu$ is the microwave photon energy. The line with $g\approx 4.3$ corresponds to a center whose low-symmetry crystal field component is much greater than the Zeeman energy. Here the parameter D in the spin Hamiltonian satisfies the condition $D\gg h\nu$.

It is supposed in Refs. (1–7) that the resonance lines with g factors $g\approx 2$ and $g\approx 4.3$ belong to different vibronic states of the same magnetic center of the Fe^{3+} ion. This supposition was based on an analysis of the temperature dependence of the EPR spectra of substances containing noncentral Fe^{3+} ions,[1–4,6,7] and a noncentral-ion model[5] that takes account of all electronic–vibrational (vibronic) states. This model is similar to the model describing the temperature variation of the EPR spectrum of a Jahn–Teller ion with an ^2E orbital ground state.[10,11]

For clarity in presenting the structure and properties of the vibronic states, Fig. 4a shows schematically the shape of a potential surface with two potential wells. The parameters E_0 and R_0 denote the height of the barrier separating the potential wells and the spontaneous displacement of the Fe^{3+} ion from the symmetry point of the molecular environment. The number of wells can be different in different substances. For example, in polyparaphenylene the Fe^{3+} magnetic ion possesses two potential wells[6] whereas noncentral ions in cubic crystals can possess six or eight potential wells.[8]

It is convenient to divide the entire collection of vibronic states into three parts according to their properties. These groups of states can be called, by analogy to Ref. 11, under-barrier, near-barrier, and over-barrier. In Fig. 4a the gray shading marks the region of near-barrier states. A magnetic ion in an under-barrier state is actually localized in one of the potential wells, as a result of which the molecular environ-

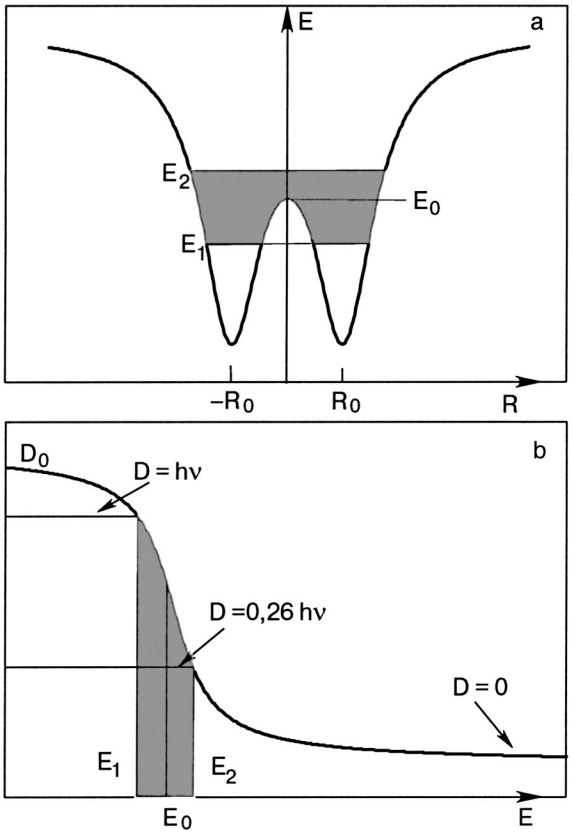

FIG. 4. The shape of the potential surface of a noncentral ion (a) and the dependence of the initial splitting parameter on the energy of the vibronic state (b).

ment of the ion is distorted more strongly than that of the ion in any over-abarrier state. The near-barrier states possess intermediate properties, which depend strongly on the excitation energy and vary from the isotropic properties of over-barrier states to the strongly anisotropic properties of below-barrier states.

A distortion of the environment engenders a low-symmetry component of the crystal field acting on a magnetic ion. The parameter D in the effective spin Hamiltonian describes this low-symmetry component of the crystal field. The values of the parameter D are different for different vibronic states. Figure 4b shows schematically the dependence of the parameter D on the activation energy of the vibronic state. The maximum value of the parameter D_0 corresponds to the ground vibronic state. The parameter D is zero for over-barrier vibronic states.

It is shown in Ref. 5 that for a fixed microwave photon energy $h\nu$ a line with g factor $g \approx 4.3$ is observed in the EPR spectrum of a polycrystalline sample when the parameter of the initial splitting of the ground vibrational state satisfies the condition $D \geqslant h\nu$, which is less stringent than the condition $D \gg h\nu$ presented in Ref. 9. For a Fe^{3+} ion the condition $D = h\nu$ determines the boundary E_1 between the over- and near-barrier states.

A necessary condition for observing a resonance line with $g \approx 2$ in the EPR spectrum of a polycrystalline sample is $D \leqslant 0.26 h\nu$.[5] For a Fe^{3+} ion the condition $D = 0.26 h\nu$ determines the boundary E_2 between the near- and over-barrier states.

2. The modeling performed in Ref. 5 of the shape of the absorption line in the EPR spectrum shows that magnetic-dipole transitions in polycrystalline substances engenders only the resonance lines *1* and *2*. The nonresonance absorption observed experimentally is not due to magnetic-dipole transitions. This absorption could be due to electric-dipole transitions between vibronic states.

The experimental results presented in Figs. 1–3 were obtained with a 3-cm EPR spectrometer with a H_{012} square cavity. The experimental sample was placed in a 3-mm in diameter glass ampul at an antinode of the alternating magnetic field at the center of the cavity. The amplitude of the alternating electric field at the center of the cavity is zero, but away from the center it increases and reaches its highest value at the distance $\lambda/4$. The ampul diameter is large enough with respect to $\lambda/4$ that the alternating electric field at the boundaries of the sample can be assumed to be different from zero. Noncentral magnetic ions in below- and near-barrier states possess an electric dipole moment **d** different from zero. For this reason these ions can interact with an alternating electric field. The interaction $-(\mathbf{d}\cdot\mathbf{E})$ at an antinode of the electric field is several orders of magnitude stronger than the interaction $-g\mu_B(\mathbf{S}\cdot\mathbf{H})$ at an antinode of an alternating magnetic field. Consequently, even a weak electric field acting on part of the sample near an antinode of the magnetic field can result in higher microwave power absorption than an alternating magnetic field.

If this supposition is correct, then it is clear why the intensity of the nonresonance contribution decreases with increasing temperature. If the barrier height is low, then a temperature increase results in filling of the over-barrier states. As the population of these states increases, the population of below- and near-barrier states decreases. The electric dipole moment is zero for over-barrier states, so that these states do not contribute to nonresonance absorption. As a result, the higher the temperature, the weaker the nonresonance absorption is.

As the magnetic field increases, nonresonance absorption decreases. To explain this feature it is necessary to take account of the fact that each vibronic state is five-fold spin degenerate ($S = 5/2$). Each vibronic state splits in a magnetic field. The properties of this splitting are ordinarily described by an effective spin Hamiltonian. The properties of the vibronic state determine the parameters of its spin Hamiltonian.

The main parameters of a spin Hamiltonian with $S = 5/2$ are the g factor and the initial splitting parameter D. For a S ion the degree of distortion of the molecular environment strongly influences the parameter D and, as a rule, has no effect on the anisotropy of the g tensor. For this reason the g factor in the spin Hamiltonians of all vibronic states is approximately the same and equal to g_2, and the parameter D takes on different values for different vibronic states. The ground vibronic state corresponds to the maximum value of the parameter $D = D_0$, and the over-barrier vibronic states correspond to spin Hamiltonians with $D = 0$.

In a strong magnetic field ($g\mu_B H \gg D$) the dependence of the energy ε_n of the nth vibronic state on the magnitude of the magnetic field is determined solely by the g factor which has the same value for all vibronic states:

$$\varepsilon_n = \varepsilon_{0n} + g\mu_B H m, \quad (1)$$

where m is the projection of the spin S on the Z axis, μ_B is the Bohr magneton, H is the magnitude of the constant magnetic field, and ε_{0n} is the energy of the nth vibronic state at $H=0$. According to the relation (1), the resonance condition for an electric-dipole transition between two vibronic states with the same spin projections is independent of the magnetic field. This means that for $g\mu_B H \gg D$ the electric-dipole absorption is independent of H and therefore cannot be observed in the EPR spectrum.

Conversely, if the magnetic field is weak ($g\mu_B H < D$), then the contribution of the parameter D to the dependence of the energy on the magnetic field becomes substantial. The energies of the vibronic states with different values of the parameter D depend differently on H.

It can be concluded on the basis of this analysis that the magnetic field dependent contribution of the electric-dipole transitions between different vibronic states should be strongest for weak magnetic fields and should decrease and vanish completely with increasing magnetic field. This agrees qualitatively with the experimentally observed behavior of the nonresonance absorption. This gives a basis for believing that the nonresonance absorption is a characteristic manifestation of ''noncentrality'' in the EPR spectrum.

3. CONCLUSIONS

The present investigations show that the EPR spectrum of noncentral Fe^{3+} ions in molecular substances can have substantially different forms. The difference in the form of the spectrum is due to the characteristics of the wells in the potential surface. The strong influence of the shape of the potential wells on the EPR spectrum opens up new possibilities for the experimental investigation of magnetic centers which exhibit noncentrality.

*E mail: chaban@zero.fti.ac.donetsk.ua

[1] V. P. D'yakonov, V. N. Vasyukov, V. A. Shapovalov, E. I. Aksiment'eva, H. Szymczak, and S. Peichota, Fiz. Tekh. Vys. Davleniĭ **8**, 60 (1998).
[2] V. N. Vasyukov, V. P. D'yakonov, V. Shapovalov, E. I. Aksiment'eva, H. Szymczak, and S. Piechota, Fiz. Nizk. Temp. **26**, 363 (2000) [Low Temp. Phys. **26**, 265 (2000)].
[3] V. N. Vasyukov, V. V. Shapovalov, S. A. Schwarz, M. H. Rafailovich, J. C. Sokolov, and V. A. Shapovalov, J. Magn. Reson. (1969-1992) **154**, 15 (2002).
[4] V. V. Chabanenko, V. N. Vasyukov, R. O. Kochkanyan, M. M. Nechitaĭlov, H. Szymczak, S. Piechota, and A. Nabyalek, Fiz. Nizk. Temp. **28**, 66 (2002) [Low Temp. Phys. **28**, 49 (2002)].
[5] V. N. Vasyukov, Fiz. Nizk. Temp. **28**, 282 (2002) [Low Temp. Phys. **28**, 199 (2002)].
[6] V. N. Vasyukov, V. A. Shapovalov, V. P. Dyakonov, A. F. Dmitruk, E. I. Aksimentjeva, H. Szymczak, and S. Piechota, Int. J. Gen. Syst. **88**, 525 (2002).
[7] V. N. Vasyukov, V. A. Shapovalov, V. P. Dyakonov, V. V. Shapovalov, E. I. Aksimentjeva, H. Szymczak, and S. Piechota, Magn. Crys. Liq. Crys. **384**, 13 (2002).
[8] M. F. Deĭgen and M. D. Glinchuk, Usp. Fiz. Nauk **114**, 185 (1974) [Sov. Phys. Usp. **17**, 691 (1975)].
[9] Ya. G. Klyava, *EPR Spectroscopy of Disordered Solids*, Znanie, Riga (1988).
[10] V. N. Vasyukov, Phys. Status Solidi B **137**, 623 (1986).
[11] V. N. Vasyukov and B. Ya. Sukharevskiĭ, Fiz. Nizk. Temp. **20**, 821 (1994) [Low Temp. Phys. **20**, 644 (1994)].

Translated by M. E. Alferieff

ELECTRONIC PROPERTIES OF METALS AND ALLOYS

On the surface magnetization of a conductor in an alternating electric field

V. M. Gokhfel'd*

A. A. Galkin Donetsk Physicotechnical Institute, Ukrainian National Academy of Sciences, ul. Rozy Lyuksemburg 72, Donetsk 83114, Ukraine

(Submitted February 16, 2004; revised May 11, 2004)
Fiz. Nizk. Temp. **30**, 1279–1282 (December 2004)

The nonequilibrium contribution to the electron paramagnetic susceptibility of a conductor in an alternating electric field applied to the surface of the conductor is calculated. © *2004 American Institute of Physics.* [DOI: 10.1063/1.1820035]

1. INTRODUCTION

The equilibrium spin magnetization of metals, which Dorfman discovered and Pauli explained, is well known.[1,2] However, the nonequilibrium nature of the electron distribution in alternating and nonuniform external fields—with a constant magnetic field **H**—can also be spin-polarized, i.e. different for spin subbands with depths $\varepsilon_F+\beta H$ and $\varepsilon_F-\beta H$ (ε_F is the Fermi energy, $\beta=e\hbar/2mc$ is the Bohr magneton). Specifically, the breakdowns of the electrical neutrality of a conductor which are caused by an alternating electric field should be accompanied by forced (with the same frequency ω) oscillations of the magnetic moment **M** of the conductor. Evidently, the effect is a surface effect: the induced magnetization $4\pi\tilde{\mathbf{M}}(0)$ has its maximum value (in modulus) at the boundary.

In the present brief communication this quantity will be calculated under reasonable simplifying assumptions and expressed in terms of the parameters of the electron spectrum. The nonequilibrium magnetization appearing in an asymmetric (no center of inversion) metal as a result of the interaction of electronic spins with the impurity potential in an electric field has been investigated in Ref. 3; the important role of nonuniformity in magnetoelectric phenomena has been pointed out in Ref. 4. In the case studied here, the natural nonuniformity due to the presence of the boundaries of the sample plays the main role, and scattering processes (with respect to momentum and spin) can be studied here in a simplified manner, since the transit time of carriers through the perturbed layer at the surface is very short on the average.

2. ELECTRIC FIELD

Let a constant magnetic field[1)] **H** and an alternating electric field with intensity $E(0)\exp(-i\omega t)$ be applied in a direction *normal to the surface* of a semi-infinite sample ($0\leqslant z<\infty$). The surface is assumed to be parallel to the crystal reflection plane and not to scatter charge carriers.[2)] We shall take account of the volume scattering in momentum space in the τ approximation; spin relaxation in a sufficiently strong "submagnetizing" field **H** is inhibited and can be neglected. This makes it possible to write separate kinetic equations for each spin projection:

$$i(kv_z-\omega)\psi_k+\tau^{-1}\left(\psi_k-\frac{\langle\psi_k\rangle_\pm}{\langle 1\rangle_\pm}\right)=-ev_zE_k, \tag{1}$$

supplementing the equations with the Poisson equation

$$ikE_k=2E(0)-4\pi e\sum_\pm\langle\psi_k\rangle_\pm \tag{2}$$

for the function E_k. For the sake of simplicity, we shall consider an electron spectrum which is axisymmetric with respect to the OZ axis, so that the magnetic field does not appear in Eqs. (1) and (2) explicitly. However, the brackets with the subscripts $\pm$ denote integration over the isoenergy surfaces $\varepsilon=\varepsilon_F\pm\beta H$ (with weight $|v|^{-1}(2\pi\hbar)^{-3}$). Thus $\langle 1\rangle_\pm$ are the corresponding partial densities of states; $\langle 1\rangle_+ +\langle 1\rangle_-=\langle 1\rangle$. The general time factor $\exp(-i\omega t)$ is omitted here and below.

The problem of the penetration of a longitudinal electric field into a metal is analyzed in detail in Refs. 5 and 6. The total distribution of the induced magnetic moment $\tilde{M}(z)$ in the sample can be found by proceeding similarily.[3)] However, here we are interested only in a narrow region at the surface of the conductor (and frequencies ω and τ^{-1} much less than the electron plasma frequency Ω_e). Consequently, passing in Eqs. (1) and (2) to the limit of large k we obtain immediately

$$\psi_k=ieE_k/k;\quad E_k=\frac{-2ikE(0)}{k^2+\kappa^2}, \tag{3}$$

where

$$\kappa=\sqrt{4\pi e^2\langle 1\rangle} \tag{4}$$

is the known (and for metals actually very large, $\simeq\Omega_e/v_F$) static-screening damping constant. It is evident that the assumption of axial symmetry of the spectrum becomes superfluous for $\beta H\ll\hbar\Omega_e$, i.e. it in no way limits the generality of the present analysis.

3. INDUCED MAGNETIZATION

The nonequilibrium part of the spin magnetic moment **M** can evidently be determined as the difference of nonequilibrium populations of the spin subbands multiplied by $\beta\mathbf{H}/H$. According to Eq. (3) the corresponding Fourier transform is

$$\tilde{M}_k \equiv \beta(\langle\psi_k\rangle_+ - \langle\psi_k\rangle_-) \approx 2\beta eE(0)\frac{\langle 1\rangle_+ - \langle 1\rangle_-}{k^2+\kappa^2}, \qquad (5)$$

so that expanding in powers of $\beta H \ll \varepsilon_F$ gives for the surface value of the inverse transform $\tilde{M}$

$$\tilde{M}(0) \approx \beta eE(0)\frac{\langle 1\rangle_+ - \langle 1\rangle_-}{\kappa} \approx M_{\text{para}}\frac{2eE(0)}{\kappa}\left(\frac{\partial \ln\langle 1\rangle}{\partial\varepsilon}\right)_{\varepsilon=\varepsilon_F}, \qquad (6)$$

where

$$M_{\text{para}} = \beta^2\langle 1\rangle H$$

is the well-known expression for the equilibrium paramagnetic moment.[2] For a typical metal the corresponding susceptibility (in SI units) is $\chi_{\text{para}} \equiv 4\pi M_{\text{para}}/H \simeq 10^{-5}$. The nonequilibrium moment (6) is proportional to the energy acquired by a charge over the penetration length of the electric field and is independent of the frequency (for $\omega \ll \Omega_e$). We have obtained a quite general result: the coefficient of transformation of the electric field into an additional magnetic field is determined only by the electron density of states $\langle 1\rangle$ and its derivative near the Fermi energy ε_F. If $\langle 1\rangle(\varepsilon) \propto \sqrt{\varepsilon}$, as in the case of a quadratic spectrum, then the amplitude of the surface magnetization is

$$4\pi\tilde{M}(0) \approx \frac{\hbar\kappa}{2mc}\frac{\beta H}{\varepsilon_F}E(0). \qquad (7)$$

We call attention to the exceptional case of a two-dimensional (or quasi-two-dimensional, which is possible in layered conductors) electronic spectrum, where the density of states is independent of energy.[7,8] In this case the expression (6) vanishes, i.e. the effect is absent in the present approximation. Conversely, the effect should be substantially stronger when the function $\langle 1\rangle(\varepsilon)$ varies sharply near ε_F.

4. DISCUSSION AND ESTIMATES

The expressions (6) and (7) are convenient for making a relative estimate

$$r \equiv \frac{\tilde{M}(0)}{M_{\text{para}}} = \frac{\tilde{\chi}(0)}{\chi_{\text{para}}} \simeq \frac{E(0)}{\sqrt{N\varepsilon_F}}. \qquad (8)$$

In principle, the perturbing field $E(0)$ is limited only by the electric strength S of the insulating layer between the sample and the electrode. For good dielectrics $S \simeq 10^4$ c.g.s.e.m.u.[9] Setting $E(0) \simeq 10^3$ c.g.s.e.m.u. we obtain $r \simeq 10^{-2}$ for a typical metal. But, for example, for bismuth with volume carrier density $N \simeq 10^{18}$ cm^{-3} and $\varepsilon_F \simeq 10^{-14}$ erg (Ref. 10) $r \simeq 10$. Thus, in strong electric fields the surface value of the nonequilibrium magnetization $\tilde{M}(0)$ can even exceed the equilibrium paramagnetic moment.

However, only the integrated magnetization of a sample with macroscopic thickness D can actually be measured, while according to the expressions (4) and (5) $\tilde{M}(z)$ decreases rapidly (with damping constant κ) with depth.[4] Averaging over the sample volume, we obtain for the effective (observable) magnetic susceptibility

$$\tilde{\chi}_{\text{eff}} \approx \frac{\tilde{\chi}(0)}{\kappa D} = 2\beta^2\frac{E(0)}{eD}\left(\frac{\partial \ln\langle 1\rangle}{\partial\varepsilon}\right)_{\varepsilon=\varepsilon_F} \simeq \beta^2\frac{E(0)}{eD\varepsilon_F}, \qquad (9)$$

where the last (order of magnitude) equality refers to a smooth power-law function $\langle 1\rangle\ \varepsilon$. Consequently, the effect is easier to observe in thin samples.[5] For purposes of estimation we assume that D is of the order of the film thickness, $D \simeq 10^{-4}$–10^{-5} cm. In addition, Eqs. (8) and (9) show that the most suitable objects would be conducting crystals with low Fermi energies: semimetals, organic complexes with charge transfer,[12] and a wide class of doped semiconductors, which are degenerate at low temperatures, with even lower values of ε_F. Summarizing and substituting on the right-hand side of Eq. (9) the approximate parameter values stipulated above we obtain

$$\tilde{\chi}_{\text{eff}} \simeq 10^{-9}. \qquad (10)$$

Fast SQUID measurements of the magnetic field with sensitivity $\simeq 10^{-12}$ have been reported in the literature. Ultraweak magnetic fields down to 10^{-13} G can also be detected (see Refs. 13–15 and the literature cited there). Consequently, it is entirely possible to discriminate the effect, especially an alternating effect, against the background of a constant magnetizing field **H**.

We note that in a macroscopic description, i.e. neglecting spatial dispersion, a longitudinal (irrotational) electric field could not generate oscillations of the magnetization (since $\dot{\mathbf{B}} = -c(\nabla\times\mathbf{E})$. Consequently, the nonequilibrium magnetoelectric effect is nontrivial and in itself merits experimental observation. In addition, it could serve for making experimental estimates of an important characteristic of the electronic spectrum—the rate of change of the energy density of states near the Fermi energy—and studying situations where this rate is anomalously high.

The contribution of orbital motion of carriers, which is neglected here, to the nonequilibrium magnetization depends in a more complicated manner on the spectral parameters. However, it can be shown that for general values of these parameters it is approximately of the same order of magnitude (absolute magnitude) as the spin contribution found here. It is unlikely that these terms will compensate one another completely, so that the expressions presented above are adequate for making an order of magnitude estimate of the total effect.

I thank V. D. Natsik, Yu. G. Pashkevich, V. G. Peschanskiĭ, I. V. Svechkarev, and S. V. Tarasenko for a discussion of this work and for helpful remarks.

*E mail: gokhfeld@teor.fti.ac.donetsk.ua

[1)]Strictly speaking, including the equilibrium magnetization of an electron gas; however, the ionic subsystem is assumed to be nonmagnetic.

[2)]This assumption greatly simplifies the mathematical formulation of the problem, i.e. the transition to Fourier transforms (with wave number k) in the Eqs. (1) and (2) following below.[5,6] However, taking account of surface scattering would hardly change the asymptotic behavior of the function E_k for large values of $|k|$; it is this asymptotic behavior that is used below.

[3)]The distribution of the induced magnetization in the sample, including also the piezomagnetic case, will be examined in detail elsewhere.

[4)]However, the decrease slows down substantially at distances exceeding κ^{-1}. The exact solution of the problem shows that a weak nonuniformity of the electron distribution together with the ''tail'' of $\tilde{M}(z)$ also remain up to macroscopic depths of the order of the carrier mean free path.

[5)]The equilibrium electron magnetization of thin metal films is studied in Ref. 11.

[1] Ya. G. Dorfman, Z. Phys. **23**, 286 (1924).
[2] W. Pauli, Z. Phys. **41**, 81 (1927).
[3] L. S. Levitov, Yu. V. Nazarov, and G. M. Éliashberg, Zh. Éksp. Teor. Fiz. **88**, 229 (1985) [JETP **61**, 133 (1985)].
[4] V. G. Bar'yakhtar, V. A. L'vov, and, D. A. Yablonskiĭ, JETP Lett. **37**, 673 (1983).
[5] V. M. Gokhfel'd, M. A. Gulyanskiĭ, M. I. Kaganov, and A. G. Plyavenek, Zh. Éksp. Teor. Fiz. **89**, 985 (1985) [JETP **62**, 566 (1985)].
[6] V. M. Gokhfel'd, M. I. Kaganov, and G. Ya. Lyubarskiĭ, Zh. Éksp. Teor. Fiz. **92**, 523 (1987) [JETP **65**, 295 (1987)].
[7] T. Ando, A. Fowler, and F. Stern, *Electronic Properties of Two-Dimensional Systems* [Russian translation], Mir, Moscow (1985).
[8] V. M. Gokhfel'd, M. I. Kaganov, and V. G. Peschanskiĭ, Fiz. Nizk. Temp. **12**, 1173 (1986) [Sov. J. Low Temp. Phys. **12**, 661 (1986)].
[9] G. I. Skanavi, *The Physics of Dielectrics*, Moscow (1958).
[10] V. S. Édel'man, in *Conduction Electrons*, edited by M. I. Kaganov and V. S. Édel'man, Nauka, Moscow (1985).
[11] S. S. Nedorezov, JETP Lett. **14**, 415 (1971).
[12] M. Pope and C. E. Swenberg, *Electronic Processes in Organic Crystals*, Oxford University Press, New York (1982) [Russian translation], Moscow (1985).
[13] A. Barone and G. Paterno, *Physics and Applications of the Josephson Effect*, Wiley, New York (1982).
[14] I. M. Dmitrenko, in *Solid State Physics. Encyclopedic Dictionary*, Naukova dumka, Kiev (1998), Vol. 2, p. 238.
[15] I. O. Kulik, in *Solid State Physics. Encyclopedic Dictionary*, Naukova dumka, Kiev (1998), Vol. 1, p. 229.

Translated by M. E. Alferieff

QUANTUM EFFECTS IN SEMICONDUCTORS AND DIELECTRICS

Effect of temperature variation on shift and broadening of the exciton band in $Cs_3Bi_2I_9$ layered crystals

V. F. Machulin, F. V. Motsnyi,* O. M. Smolanka, and G. S. Svechnikov

V. Lashkaryov Institute of Semiconductor Physics of the National Academy of Sciences of Ukraine, 41 Nauky Ave., Kyiv 03028, Ukraine

E. Yu. Peresh

Uzhgorod National University, Chemical Faculty, 46 Pidgirna St., Uzhgorod 88000, Ukraine
(Submitted February 26, 2004; revised April 29, 2004)
Fiz. Nizk. Temp. **30**, 1283–1286 (December 2004)

The exciton reflection spectra of $Cs_3Bi_2I_9$ layered crystals are investigated in the temperature region 4.2–300 K with light polarization $\mathbf{E}\perp\mathbf{c}$. It is estimated that the energy gap E_g equals 2.857 eV ($T=4.2$ K) and the exciton binding energy Ry is 279 meV. A nontraditional temperature shift of $E_g(T)$ for layered substances is found for the first time. It is learned that this shift is described very well by the Varshni formula. A transition region in the temperature broadening of the half-width $H(T)$ of the exciton band with increase of temperature is registered in the interval between 150 and 220 K. It is shown that this region may be identified as the heterophase structure region where ferroelastic and paraelastic phases coexist. A surge of $H(T)$ at the point of the ferroelastic phase transition ($T_c=220$ K) is also observed. © *2004 American Institute of Physics.* [DOI: 10.1063/1.1820036]

1. INTRODUCTION

$Cs_3Bi_2I_9$ crystals belong to an extensive family of little-studied three-component $A_3B_2X_9$ layered compounds (A are alkaline atoms, B=As, Sb, Bi, Fe, Cr, Mo, or W, and X =Br, Cl or I),[1,2] which are kindred to the well-known perovskites. Interest in these crystals is caused by the manifestation of a ferroelastic second-order phase transition at the temperature $T_c=220$ K[2–4] accompanied by a reversible change of crystal symmetry class from hexagonal $6/mmm$ to centrosymmetric monoclinic $2/m$, the prediction of an incommensurate phase at $T<220$ K,[1,5] and the possibilities of practical use in recorder systems, pressure and γ-emission sensors, and acousto- and optoelectronics.

Optical data on $Cs_3Bi_2I_9$ crystals have been obtained in connection with the birefrigence,[2] exciton states,[6,7] phonon spectra,[8] and low-temperature optical characteristics.[9]

On the other hand, one of the important physical properties of layered crystals is the anomalous temperature dependence of the energy gap $E_g(T)$, which increases at $T<T_m$ and decreases at $T>T_m$. For different layered crystals T_m varies within a temperature range of 30–45 K.[10–14] The phenomenon originates from high anisotropy of the chemical bonding due to the strong ionic-covalent bonding in separate sandwich layers and the weak van der Waals binding between neighboring sandwiches. This is confirmed by the presence of low-frequency optical vibrations in the Raman spectra of layered crystals[8,13,15–18] which determine the exciton-phonon interaction,[14,19,20] spin-lattice relaxation,[21] temperature dependence of electron paramagnetic resonance (EPR) spectra,[21,22] and also a large difference in the linear broadening coefficients in the directions perpendicular to the layers and in the planes of the layers.[23] Anomalous temperature behavior of $E_g(T)$ can be explained on the basis of the essential influence of anharmonic optical vibrations of the layered lattice starting at low temperature and of low-frequency optical phonons starting at higher temperatures.[14,24] However, this temperature dependence has not been studied for $A_3B_2X_9$ compounds in general and for $Cs_3Bi_2I_9$ crystals in particular.

The aim of this paper is to study the temperature behavior of the exciton band of $Cs_3Bi_2I_9$ layered crystals.

2. EXPERIMENTAL

$Cs_3Bi_2I_9$ layered crystals were grown by the Bridgman method. The peculiarities of this technology are given in Refs. 25 and 26. Samples with dimensions of approximately $7\times5\times0.02$ mm were cut off from a bulk crystal in air with a blade. Special care was taken to avoid deformations. The samples had a mirror-smooth surface with the optic axis c perpendicular to cleavage surface. The reflection spectra were measured in the heating regime. They were recorded with an automated experimental setup based on a MDR-23 monochromator in the energy interval of 2.0–3.5 eV in the temperature range of 4.2–300 K and with light polarization $\mathbf{E}\perp\mathbf{c}$. The energy resolution was better than 0.5 meV. The relative error of measurement of the reflection spectra did not exceed 3%. The temperature was stabilized with accuracy better than 0.1 K.

The resonance energies of the exciton absorption bands were determined from the inflection point of the exciton oscillation with quantum number $n=1$ by setting the second derivative of the reflection coefficient with respect to energy

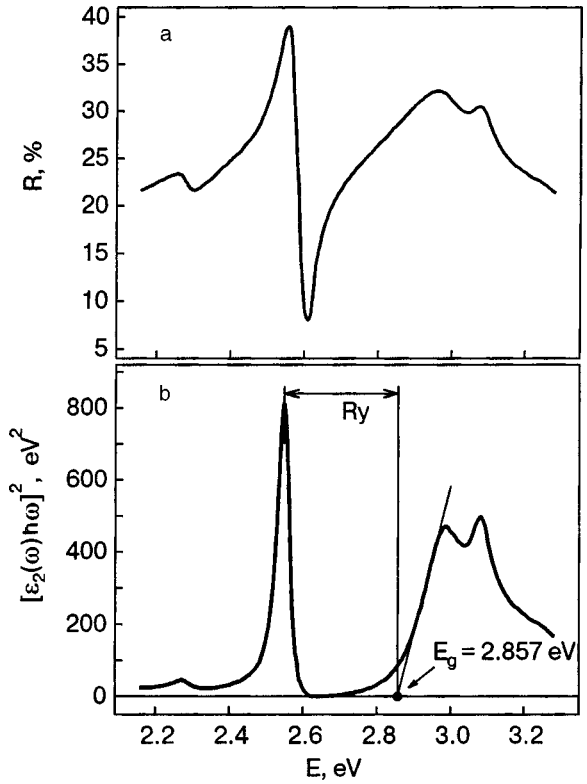

FIG. 1. Reflection spectrum at $T=4.2$ K with $\mathbf{E}\perp\mathbf{c}$ (a) and $[\varepsilon_2(\omega)\hbar\omega]^2$ (b) for $Cs_3Bi_2I_9$ layered crystals.

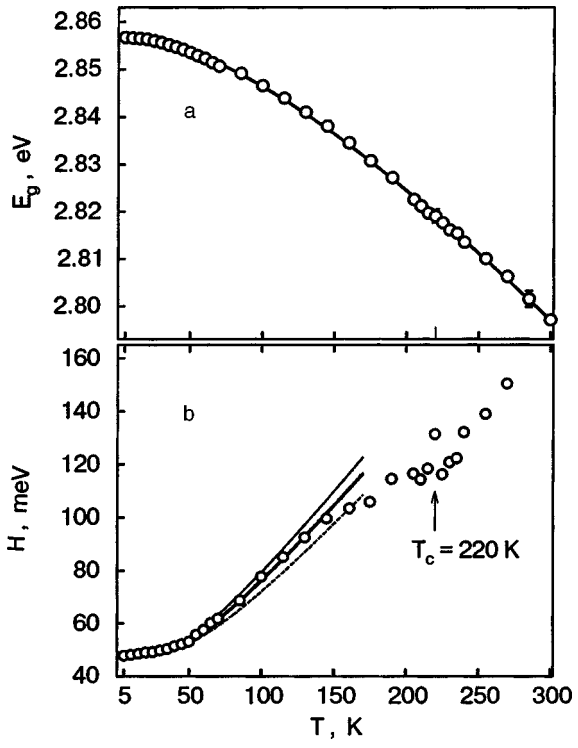

FIG. 2. Temperature shift of the energy gap $E_g(T)$ (a) and broadening of the half-width $H(T)$ (b) of the exciton band of $Cs_3Bi_2I_9$ layered crystals.

equal to zero ($d^2R/dE^2=0$). The inflection point found in such a way coincides up to $T\leqslant 200$ K with the one determined in the ordinary way as the half energy interval or the half distance on the reflectance scale between the extrema of the exciton oscillation. The half-width $H(T)$ of the exciton absorption band was found as the energy difference between the maximum and the minimum of the fundamental exciton oscillation. The insertion errors in the measured values of the temperature variations of the energy position of the exciton band $E_{ex}(T)$ and its half-width are insignificant[11] and do not influence their qualitative course.

3. RESULTS AND DISCUSSION

A typical reflection spectrum at 4.2 K and $\mathbf{E}\perp\mathbf{c}$ and the dependence of $[\varepsilon_2(\omega)\hbar\omega]^2$ as a function of energy $\hbar\omega$ for $Cs_3Bi_2I_9$ crystals are shown in Fig. 1. The intense oscillation with inflection point at energy 2.578 eV and the two shorter-wavelength maxima at energies of 2.961 and 3.073 eV (Fig. 1a) are caused by excitons in the ground state ($n=1$) and interband electronic transitions, respectively.[6,7] On the basis of this spectrum, extrapolation by the Yahoda method,[1)] and the Kramers–Kronig relations, we have previously[9] found the real $\varepsilon_1(\omega)$ and imaginary $\varepsilon_2(\omega)$ parts of the complex dielectric function $\varepsilon(\omega)$. Knowing $\varepsilon_2(\omega)$, we estimated the direct band gap E_g of $Cs_3Bi_2I_9$ crystals at 4.2 K and $\mathbf{E}\perp\mathbf{c}$. The dependence of $[\varepsilon_2(\omega)\hbar\omega]^2$ as a function of energy $\hbar\omega$ was constructed in accordance with Ref. 27 (Fig. 1b). One can see three intense bands with maxima at energies of 2.548, 2.986, and 3.079 eV. The calculated spectrum satisfactorily correlates with the experimental reflection spectrum. The value of E_g in such a case is estimated as the energy of the cutoff. It equals 2.857 eV. The binding energy Ry of the exciton is found as the difference between E_g and the maximum of the exciton band, that is Ry=279 MeV. It should be noted that Ry in the $Cs_3Bi_2I_9$ crystals is high, and higher than in basic BiI_3 (Ry=144 MeV).[19] This may be explained by that fact that $Cs_3Bi_2I_9$ crystals are alkali halide compounds. In such substances the polar type of chemical bonding takes place, and therefore Ry may be high.

The temperature shift of the energy gap $E_g(T)$ and the temperature dependence of the half-width $H(T)$ of the exciton absorption band of $Cs_3Bi_2I_9$ crystals are shown in Fig. 2. In Fig. 2a the points are experimental data for $E_g(T)$ and the continuous curve represents $E_g(T)$ as obtained from the computation by the Varshni formula[28]

$$E_g(T)=E_g(0)+\frac{\alpha T^2}{T+\theta}, \tag{1}$$

where $E_g(0)=2.857$ eV, $\alpha=-3.7\times10^{-4}$ eV/K, and $\theta=258.654$ K. We would like to stress a few points: 1) the experimental results are described very well by this formula; 2) the energy position of the energy gap does not change at $T<45$ K and shifts to the long-wavelength side with increase of temperature up to 300 K without any anomalies at $T_c=220$ K. Such behavior of $E_g(T)$ is not peculiar to layered semiconductors but is typical for the majority of the well-studied ones, for example Ge, Si, SiC, II–VI, and III–V. It can therefore be explained in the following manner. First, at low temperatures the mechanisms caused by the interaction of electrons and holes with acoustic and optical phonons are turned on and then at higher temperature the other mecha-

nisms connected with the thermal expansion of the crystal lattice take place. It is very important that all mechanisms contribute with the minus sign.

The absence of an anomaly in the temperature shift of $E_g(T)$ allow us to suppose that the anisotropy of the optical properties in the monoclinic structure is not high. This conclusion correlates very well with the low intensities of the low-frequency doublets (33.4, 38.3), (44.3, 48.2) cm^{-1} in the Raman spectra at 4.2 K. Therefore $Cs_3Bi_2I_9$ crystals are not typical layered compounds. These crystals can be considered as layered semiconductors in the hexagonal phase and normal ones in the monoclinic phase.

Thus $Cs_3Bi_2I_9$ crystals demonstrate nontraditional temperature behavior of $E_g(T)$ for layered substances.

The experimental temperature dependence of the half-width $H(T)$ (points) of the exciton band of $Cs_3Bi_2I_9$ crystals is depicted in Fig. 2b. With increasing temperature from 4.2 to 150 K the half-width increases nonlinearly from 48.9 to 99.7 meV. Then $H(T)$ begins to rise less sharply, forming a plateau (the transition region) up to $T<220$ K with a surge at $T=220$ K. After that $H(T)$ returns almost to the starting point at $T=225$ K and increases linearly ($H(T)=k(T-225\ \mathrm{K})+H_0$, where $k=0.758$ MeV/K and $H_0=116.3$ MeV) in the temperature range $225\ \mathrm{K}\leqslant T\leqslant 300$ K.

We made an effort to model the temperature dependence of the half-width of the exciton band. It was found that the half-width can be described at $T\leqslant 150$ K by the following equation:

$$H(T)=H(0)\coth\left[\frac{\hbar\omega_{\mathrm{ph}}}{2kT}\right], \tag{2}$$

obtained by Toyozawa[29] for weak exciton-phonon interaction. Here $H(0)$ is the half-width at absolute zero temperature and $\hbar\omega_{\mathrm{ph}}$ is the energy of the interacting phonon. The results of the modeling are given in Fig. 2b for $H(0)=48.92$ MeV and two real optical phonons which were registered in Raman spectra[8] at 4.2 K. The calculated curves are localized above ($\omega_{\mathrm{ph}}=99.8\ cm^{-1}$) and below ($\omega_{\mathrm{ph}}=114.8\ cm^{-1}$) the experimental dependence. The best correlation between experiment and theory exists for an effective phonon with frequency $105.8\ cm^{-1}$ (thick curve). The dependence established is essentially different from the $H(T)$ dependence of the exciton band of the classical layered semiconductor BiI_3, in which the phase transitions are absent and a high exciton-phonon interaction takes place.[14,24]

The deviation of the experimental dependence $H(T)$ from the theoretical (2) and the appearance of the transition region indicate that a reconstruction of the monoclinic crystal lattice takes place between 150 and 220 K. As was shown in Ref. 30, the region 183–221 K corresponds to a heterophase structure where ferroelastic and paraelastic phases coexist. Therefore the whole transition region may be identified with the heterophase structure.

The appearance of a surge at $T=220$ K is probably due to the ferroelastic phase transition (as $T=T_c$).[2–4]

Thus the half-width of the exciton band may be used as a highly sensitive nondestructive probe for revealing a phase transition.

4. CONCLUSIONS

We have presented analyses of the effect of temperature variation on the exciton reflection spectra of $Cs_3Bi_2I_9$ layered crystals. It was found that these are not typical layered crystals. These crystals are layered semiconductors in the hexagonal phase and behave like conventional semiconductors in the monoclinic phase. We have registered a transition region in the temperature broadening of the half-width of the exciton band in the temperature interval 150–220 K and a surge at $T=220$ K. Our analyses suggest that both phenomena are caused by the formation of a heterophase structure region and the ferroelastic phase transition, respectively.

*E-mail: motsnyi@sun.semicond.kiev.ua

[1)]The optical functions of a system of two noninteracting classical oscillators were simulated taking into account the traditional extrapolations by the Philipp-Taft and Yahoda methods. It was found that the functions are in good agreement with the model functions only in the second case.

[1] I. P. Aleksandrova, A. F. Bovina, O. A. Ageev, and A. A. Sukhovsky, Fiz. Tverd. Tela (St. Petersburg) **39**, 1105 (1997) [Phys. Solid State **39**, 991 (1997)].
[2] S. V. Mel'nikova and A. I. Zaitsev, Fiz. Tverd. Tela (St. Petersburg) **39**, 1850 (1997) [Phys. Solid State **39**, 1652 (1997)].
[3] A. V. Arakcheeva, M. Bonin, G. Chapuis, and A. Zaitsev, Z. Kristallogr. **214**, 279 (1999).
[4] A. Jorio, R. Currat, D. A. A. Myles, G. J. McIntyre, I. P. Aleksandrova, J. M. Kiat, and P. Saint-Grégoire, Phys. Rev. B **61**, 3857 (2000).
[5] I. P. Aleksandrova, A. A. Sukhovsky, and K. S. Aleksandrov, Solid State Commun. **105**, 323 (1998).
[6] A. V. Kun, S. V. Kun, V. I. Kulishov, M. P. Lisitsa, F. V. Motsnyi, E. Yu. Peresh, and S. O. Sergeyev, Zh. Prikl. Spektrosk. **53**, 331 (1990).
[7] V. G. Dorogan, M. P. Lisitsa, F. V. Motsnyi, and O. M. Smolanka, Ukr. Fiz. Zh. **48**, 181 (2003).
[8] O. V. Vakulenko, V. O. Gubanov, S. V. Kun, F. V. Motsnyi, E. Yu. Peresh, and V. A. Terekhov, Proc. SPIE **3359**, 351 (1997).
[9] M. P. Lisitsa, F. V. Motsnyi, O. M. Smolanka, S. V. Kun, and E. Yu. Peresh, Ukr. Fiz. Zh. **47**, 1161 (2002).
[10] B. M. Nitsovych, G. M. Pestryakov, and I. V. Blonskyy, Fiz. Tverd. Tela (Leningrad) **23**, 2352 (1981) [Sov. Phys. Solid State **23**, 1891 (1981)].
[11] M. S. Brodin, I. V. Blonskyy, and B. M. Nitsovych, Solid State Commun. **44**, 181 (1982).
[12] G. L. Belenkii, E. Yu. Salaev, R. A. Suleimanov, and N. A. Abdullaev, Solid State Commun. **47**, 263 (1983).
[13] M. S. Brodin and I. V. Blonskyy, *Exciton Processes in Layered Crystals* [in Russian], Naukova Dumka, Kyiv (1986).
[14] F. V. Motsnyi, "Exciton and defect states in complex nonatomic, ion implanted, and epitaxial structures" [in Russian and Ukrainian], Abstracts, Institute of Semiconductor Physics, National Academy of Sciences of Ukraine, Kyiv (1993), 33 pp.
[15] Y. Petroff, P. Y. Yu, and Y. R. Shen, Phys. Status Solidi **61**, 419 (1974).
[16] W. M. Sears, M. L. Klein, and J. A. Morrison, Phys. Rev. B **19**, 2305 (1979).
[17] M. P. Lisitsa, F. V. Motsnyi, A. M. Yaremko, and O. P. Lytvynchuk, Fiz. Tverd. Tela (Leningrad) **27**, 1008 (1985) [Sov. Phys. Solid State **27**, 1675 (1985)].
[18] I. A. Dudak, V. S. Gorelik, Yu. N. Venevtsev, and F. V. Motsnyi, Zh. Prikl. Spektrosk. **49**, 503 (1988).
[19] M. P. Lisitsa, F. V. Motsnyi, and S. F. Terechova, Ukr. Fiz. Zh. **22**, 1484 (1977).
[20] F. V. Motsnyi, Ukr. Fiz. Zh. **22**, 152 (1977).
[21] M. F. Deigen, S. S. Ischenko, V. I. Konovalov, and S. M. Okulov, Fiz. Tverd. Tela (Leningrad) **20**, 476 (1978) [Sov. Phys. Solid State **20**, 276 (1978)].
[22] S. S. Ishchenko, V. I. Konovalov, S. M. Okulov, G. B. Belen'kii, and E. Yu. Salaev, Fiz. Tverd. Tela (Leningrad) **21**, 827 (1979) [Sov. Phys. Solid State **21**, 174 (1979)].
[23] Yu. A. Kovalevskaya and P. G. Strelkov, Fiz. Tverd. Tela **8**, 1302 (1966) [Sov. Phys. Solid State **8**, 1044 (1966)].

[24] F. V. Motsnyi, Mol. Phys. Rep. **23**, 62 (1999).
[25] S. V. Kun, E. Yu. Peresh, V. A. Lazarev, A. V. Orinchai, and M. I. Gorvat, Izv. Akad. Nauk SSSR, Neorg. Mater. **24**, 1899 (1988).
[26] E. Yu. Peresh, V. A. Lazarev, S. V. Kun, I. E. Barchiy, A. V. Kun, and V. I. Sidey, Izv. Akad. Nauk SSSR, Neorg. Mater. **33**, 431 (1997).
[27] A. S. Davydov, *Theory of the Solid State* [in Russian], Nauka, Moscow (1976).
[28] Y. P. Varshni, Physica **34**, 149 (1967).
[29] Yu. Toyozawa, Prog. Theor. Phys. **27**, 89 (1962).
[30] I. Girnyk, O. Krupych, I. Martynyuk-Lototska, F. Motsnyi, and R. Vlokh, Ukr. J. Phys. Opt. **4**, 165 (2003).

This article was published in English in the original Russian journal. Reproduced here with stylistic changes by AIP.

Phonon polaritons in a planar dielectric waveguide in a magnetic field

I. E. Chupis*

B. I. Verkin Institute for Low Temperature Physics and Engineering, Ukrainian National Academy of Sciences, pr. Lenina 47, Kharkov 61103, Ukraine

(Submitted March 15, 2004)
Fiz. Nizk. Temp. **30**, 1287–1292 (December 2004)

Infrared and optical polaritons propagating in an isotropic dielectric with metal coatings in the presence of a constant magnetic field parallel to the plane of the layer are studied. It is shown that a constant magnetic field creates nonreciprocal surface modes which did not exist previously at the boundary with the metal. The number of surface modes for the opposite walls is different (1 or 2) and can be changed by switching the directions of the magnetic field or the wave vector. A polariton with a fixed frequency in a magnetic field with a definite orientation propagates along a given boundary in only one direction. A constant magnetic field also creates for volume modes new frequency intervals which are proportional to the first power of the magnetic field, and simultaneously decreases the energy of the volume modes, transferring this energy into surface modes, i.e. a constant magnetic field ''pushes'' the field of an electromagnetic wave out of the interior volume and onto the surface of the dielectric. This effect is proportional to the magnitude of the constant magnetic field and the thickness of the dielectric layer. © *2004 American Institute of Physics.* [DOI: 10.1063/1.1820037]

1. INTRODUCTION

Phonon polaritons are electromagnetic waves which propagate in a medium and interact with optical phonon excitations. The influence of a magnetic field on polaritons in semiconductors and metals with free charges (so-called plasmon polaritons) has been studied in a number of works (see, for example, Refs. 1–7).

In a dielectric with no free charges the action of a magnetic field on phonon polaritons can be described by dynamical magnetoelectric (ME) energy.[8] The magnetoelectric energy describes the change in the electric polarization in a magnetic field acting on bound (ionic and electronic) charges of the dielectric. A previous investigation[9] of the effect of a magnetic field on phonon polaritons in a uniaxial semiinfinite dielectric at its boundary with an ideal metal or a superconductor has shown that polaritons which do not exist at the boundary with a metal because of the metallic extinction effect[10] appear in the presence of a magnetic field. Strong nonreciprocity of the optical and IR surface phonon polaritons in such a system was also predicted.

In the present paper phonon polaritons in an isotropic dielectric of finite thickness, coated with metal on both sides, are studied. The metal is assumed to be a good conductor, so that the tangential component of the electric field at the boundary with the metal is zero. Examples of such metals are Ag and Au.[10] The influence of the magnitude of the magnetic field and the thickness of the dielectric on the spectra of volume and surface polaritons in such a system is analyzed. It is shown that a magnetic field gives rise to nonreciprocal surface waves and causes the field of the electromagnetic wave to concentrate near the boundaries of the dielectric. This nonreciprocal displacement of the field is proportional to the magnitude of the constant magnetic field and the thickness of the dielectric.

2. DIELECTRIC TENSOR

Let the dielectric be isotropic and located in a constant magnetic field $\mathbf{H}_0$ oriented parallel to the Y axis. We write the Lagrangian density of the optical phonons in terms of the electric polarization $\mathbf{P}$ and $\dot{\mathbf{P}}$ (time derivative of the electric polarization):

$$L=\frac{\dot{\mathbf{p}}^2}{2f}-\frac{a}{2}P^2+\mathbf{eP}-\gamma\mathbf{P}[\dot{\mathbf{P}}\mathbf{H}]. \tag{1}$$

Here $\mathbf{H}=\mathbf{H}_0+\mathbf{h}$, and $\mathbf{e}$ and $\mathbf{h}$ are the alternating electric and magnetic fields. The first term in Eq. (1) is the phonon kinetic energy density. Using the relation $\mathbf{P}=q\mathbf{r}V_0^{-1}$ (V_0 is the unit-cell volume and $\mathbf{r}$ is the displacement of the charge q), we obtain $f=q^2/mV_0$, where m is the mass of the charge. The last term in Eq. (1) is the dynamical ME energy due to the interaction of $\mathbf{P}$ with the effective electric field produced by a charge moving with velocity v in a magnetic field $\mathbf{E}_{\text{eff}}=-c^{-1}(\mathbf{v}\times\mathbf{H})$; c is the speed of light. Using the preceding estimates, we find that the constant $\gamma=V_0/cq$.

In general, ions and electrons contribute to the electric polarization. The ionic contribution predominates at IR frequencies, where m is the reduced mass of the unit cell. In the optical range the electronic contribution to the polarization is much greater than the ionic contribution, and m is the electron mass. We note that the dynamical ME energy is a scalar and therefore is present in the energy of any crystal.

Solving Lagrange's equations with the function (1) and setting $\mathbf{P}$, $\mathbf{e}$, and $\mathbf{h}$ proportional to $\exp(-i\omega t)$ we find the following expressions for the components of the dielectric tensor:

$$\varepsilon=\varepsilon_{xx}=\varepsilon_{zz}=\frac{(\Omega_1^2-\omega^2)(\Omega_2^2-\omega^2)}{(\omega_1^2-\omega^2)(\omega_2^2-\omega^2)};\quad \varepsilon_{yy}=\frac{(\Omega_0^2-\omega^2)}{(\omega_0^2-\omega^2)}, \tag{2}$$

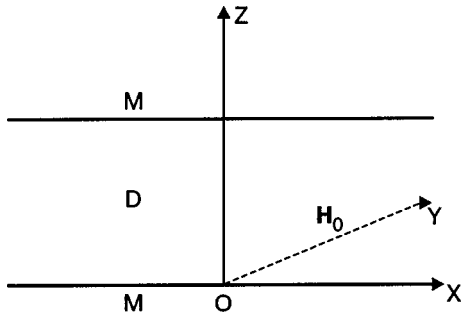

FIG. 1. Dielectric film D with thickness l and metal coatings M ($Z<0$, $Z \geqslant l$) in a constant magnetic field $\mathbf{H}_0$ oriented in the plane of the film along the positive Y axis; the wave vector $\mathbf{k}$ is oriented along the X axis.

$$i\varepsilon_{xz}=i(\varepsilon_{zx})^*=\varepsilon'=\frac{8\pi\omega\omega_H f}{(\omega_1^2-\omega^2)(\omega_2^2-\omega^2)},$$

where

$$\omega_{1,2}=\sqrt{\omega_0^2+\omega_H^2}\mp\omega_H,$$

$$\Omega_{1,2}^2=\frac{1}{2}[\omega_0^2+\Omega_0^2+4\omega_H^2 \mp\sqrt{(\Omega_0^2-\omega_0^2)^2+8\omega_H^2(\Omega_0^2+\omega_0^2)+16\omega_H^4}], \quad (3)$$

$$\omega_0^2=af,\quad \omega_H=gH_0,\quad g=f\gamma=q/mc,$$

$$\Omega_0^2=\omega_0^2+4\pi f.$$

In the absence of a magnetic field ω_0 is the frequency of the electric polarization excitations. A magnetic field removes the degeneracy of the excitations, P_y oscillates with frequency ω_0, and the excitations P_x and P_z correspond to coupled modes ω_1 and ω_2 in which the electric polarization precesses around the direction of the magnetic field. According to Eq. (2), in a magnetic field the dielectric tensor acquires off-diagonal components: ε_{xz} and ε_{zx}. These components attest to the appearance of gyrotropy.

The gyromagnetic ratio g for ionic excitations (IR region of the spectrum) is positive and is of the order of $g \sim 10^{-1}$—10^{-2} $\mathrm{A\cdot s^2\cdot kg^{-1}\cdot m^{-1}}$, and for optical range electronic excitations $|g|\sim 10^2$–10^3 $\mathrm{A\cdot s^2\cdot kg^{-1}\cdot m^{-1}}$. Assuming the ratio ω_H/ω_0 to be small we have the following approximate expressions for the frequencies (3):

$$\omega_{1,2}\approx\omega_0\mp\omega_H,$$

$$\Omega_1\approx\omega_0\left(1-\frac{\omega_H^2}{2\pi f}\right),\quad \Omega_2\approx\Omega_0\left(1+\frac{\omega_H^2}{2\pi f}\right). \quad (4)$$

3. POLARITON MODES

We shall study a flat layer of a uniaxial nonmagnetic dielectric with thickness l. Let the dielectric be in contact with an ideal metal ($Z<0$, $Z>l$). This system is actually a planar waveguide (Fig. 1). Let a constant magnetic field $\mathbf{H}_0$ be directed along the Y axis in the plane of the layer. Let an electromagnetic wave propagate in the dielectric along the X axis, and in this wave let $\mathbf{e}$, $\mathbf{h}\propto\exp(ikx-i\omega t)$. It follows from Maxwell's equations that in this geometry the magnetic field influences only the TM waves, in which the field components e_x, e_z, and h_y are nonzero and satisfy the equations

$$\frac{\partial^2 h_y}{\partial z^2}-bh_y=0,\quad b=k_x^2-\omega^2c^{-2}(\varepsilon-\varepsilon'^2\varepsilon^{-1}),$$

$$e_z=-c[\omega(\varepsilon^2-\varepsilon'^2)]^{-1}\left(\varepsilon k_x h_y+\varepsilon'\frac{\partial h_y}{\partial z}\right), \quad (5)$$

$$e_x=-ic[\omega(\varepsilon^2-\varepsilon'^2)]^{-1}\left(\varepsilon' k_x h_y+\varepsilon\frac{\partial h_y}{\partial z}\right).$$

The solution of Eq. (5) for h_y has the form

$$h_y=A\exp(-\sqrt{b}z)+B\exp(\sqrt{b}z), \quad (6)$$

where the coefficients A and B are determined from the boundary conditions, according to which the tangential component of the electric field e_x vanishes at the boundaries with an ideal metal at $Z=0,l$:

$$A(\varepsilon' k_x-\varepsilon\sqrt{b})+B(\varepsilon' k_x+\varepsilon\sqrt{b})=0, \quad (7)$$

$$A(\varepsilon' k_x-\varepsilon\sqrt{b})\exp(-\sqrt{b}l)+B(\varepsilon' k_x+\varepsilon\sqrt{b}) \times\exp(\sqrt{b}l)=0,$$

i.e. the following condition must be satisfied:

$$(\sigma^2-1)[\exp(\sqrt{b}l)-\exp(-\sqrt{b}l)]=0,\quad \sigma=\frac{\varepsilon' k_x}{\varepsilon\sqrt{b}}. \quad (8)$$

If there is no constant magnetic field, i.e. $\varepsilon'=\sigma=0$, then, as follows from Eqs. (7) and (8), $A=B$, and

$$h_y=2A\cos\alpha z,\quad \sqrt{b}=i\alpha,\quad l\alpha=n\pi\quad n=0,1\ldots. \quad (9)$$

The polaritons are volume waves. The number of modes and their dispersion laws are determined by the function $b(\omega)$ (5):

$$b=\left(k_x^2-\frac{\omega^2}{c^2}\varepsilon\right)\leqslant 0,\quad \varepsilon=\frac{\Omega_0^2-\omega^2}{\omega_0^2-\omega^2};$$

$$k_x=\pm\frac{\omega}{c}\sqrt{\varepsilon-\frac{n^2c^2\pi^2}{l^2\omega^2}}. \quad (10)$$

It follows from Eq. (10) that volume polaritons in the absence of a constant magnetic field exist in frequency ranges where $\varepsilon>0$, i.e. for $\omega<\omega_0$ and $\omega>\Omega_0$. Since the radicand in Eq. (10) must be positive, the modes exist in the frequency intervals $[\overline{\omega}_1,\omega_0]$ and $\omega\geqslant\overline{\omega}_2$ where

$$\overline{\omega}_{12}^2(n)=\frac{1}{2}[\Omega_0^2+\lambda_n^2\mp\sqrt{(\Omega_0^2+\lambda_n^2)^2-4\lambda_n^2\omega_0^2}],$$

$$\lambda_n^2=\frac{n^2c^2\pi^2}{l^2}. \quad (11)$$

The activation frequency of the mode (11) is inversely proportional to the thickness of the dielectric layer. The number of modes in these frequency ranges is infinite. For $n=0$ (or $l=\infty$) we have the dispersion law for a volume mode in a semi-infinite dielectric:

$$k_x^2=\frac{\omega^2}{c^2}\varepsilon. \quad (12)$$

The modes possess positive dispersion and lie in the radiation range.

All modes in the low-frequency range intersect the light line, and the wave vector $k_x \to \pm\infty$ as $\omega \to \omega_0$. The high-frequency modes lie to the left of the light line and approach the line asymptotically as frequency increases.

In a magnetic field off-diagonal components of the dielectric tensor $\varepsilon_{zx}=(\varepsilon_{xz})^*$ and $\varepsilon' \sim H_0$ appear and the components of the permittivity contain additional poles and zeros (2), which lie in the order (see Eq. (4)) $\omega_1 < \Omega_1 < \omega_2 < \Omega_2$. The additional frequency interval $[\omega_1, \Omega_1]$ arising in a magnetic field is proportional to H_0, while in a uniaxial dielectric the dependence is quadratic, i.e. the interval is much smaller.[9] In an isotropic dielectric the relative quantity $\Delta\omega/\omega \sim \omega_H/\omega$. In the IR range ($\omega \sim 10^{13}$ s^{-1}) in a magnetic field $H_0 \sim 10$ T the ratio $\Delta\omega/\omega \sim 10^{-4}$, and in the optical range ($\omega \sim 10^{13}$ s^{-1}) in the same field $\Delta\omega/\omega \sim 10^{-2}$.

The polariton spectrum in the presence of a magnetic field is shown in Fig. 2. The dot-dash curves, for which

$$k_x^2 = \overline{k^2} = \frac{\omega^2}{c^2}\left(\varepsilon - \frac{\varepsilon'^2}{\varepsilon}\right), \tag{13}$$

correspond to a semi-infinite crystal ($b=0$).

In the absence of a magnetic field there were two such curves: in the low- and high-frequency regions of the spectrum. These curves were described by Eq. (12). In the presence of a magnetic field there were four curves, and according to Eq. (13) they are shifted. It follows from Eqs. (6) and (7) that for $b=0$ in a constant magnetic field $A=-B$, i.e. for $k_x \neq 0$ the fields $h_y = e_z = e_x = 0$. For polarons, whose spectrum is described by the dot-dash curve, there is no electromagnetic field.

The quantity b (see Eq. (5)) is positive for $k_x^2 > \overline{k^2}$ and negative for $k_x^2 < \overline{k^2}$. Negative values of b signify the existence of volume modes. Positive values of the parameter b in the presence of a constant magnetic field correspond to the appearance of surface waves. Indeed, positive values of the parameter b in Eq. (8) correspond to real values of σ and the possibility of the solutions $\sigma = \pm 1$, i.e. $\varepsilon' k_x = \pm\varepsilon\sqrt{b}$. It follows from the expression (5) for b that Eq. (12) describes the spectrum of such waves, i.e. they exist only in frequency ranges where $\varepsilon > 0$. The sign of σ depends on the signs of H_0 and k_x, the frequency range, and the sign of the gyromagnetic ratio g ($g>0$ in the IR region of the spectrum and $g<0$ in the optical region of the spectrum). Table I gives the corresponding ranges of the parameters for $\sigma = \pm 1$. The value $\sigma = 1$ corresponds to a surface wave near the boundary $Z=0$, and if $\sigma = -1$, the wave is localized on the opposite side ($Z=l$):

$$h_y^0 = A\exp(-\sqrt{b}z), \quad B=0, \quad \sigma=1;$$

$$h_y^1 = B\exp(\sqrt{b}z), \quad A=0, \quad \sigma=-1. \tag{14}$$

According to Table I the solutions $\sigma = \pm 1$ exist in the same frequency range, but they correspond to opposite directions of propagation of a wave or opposite orientations of the constant magnetic field $\mathbf{H}_0$. Hence it follows that for given directions of $\mathbf{H}_0$ and $\mathbf{k}$ a wave with a given frequency propagates only along one of the waveguide boundaries. If the direction of the magnetic field or k_x changes, the wave will propagate along the opposite wall of the waveguide. The reason for this nonreciprocal displacement of the electromagnetic field is as follows. The action of the constant magnetic field $\mathbf{H}_0$ on the charges in the dielectric is equivalent to the action of an effective electric field $\mathbf{E}_{\text{eff}} = -c^{-1}(\mathbf{v}\times\mathbf{H}_0)$, where $\mathbf{v} \sim \mathbf{k}$ is the velocity which the charges acquire in the electromagnetic wave. In our geometry $\mathbf{E}_{\text{eff}}$ is directed along the Z axis and changes sign when the direction of $\mathbf{k}$ or $\mathbf{H}_0$ changes. Under the action of this effective electric field the charges are displaced toward one of the boundaries. The direction of displacement depends not only on the directions of $\mathbf{k}$ and $\mathbf{H}_0$ but also on the sign of the charge which predominates in the polarization process, i.e. the sign of g ($g>0$ for ionic polarizability in the IR range and $g<0$ for electronic polarizability in the optical range of the spectrum). The additional polarization arising in a magnetic field is accompanied by the appearance of an off-diagonal component of the dielectric tensor, which changes h_y according to Maxwell's equation

$$\frac{\partial h_y}{\partial z} = i\omega c^{-1}(\varepsilon e_x + \varepsilon_{xz} e_z).$$

The component $\varepsilon_{xz} \sim H_0$ and depends on the frequency. Consequently, the localization of a wave at one of the edges of the dielectric depends not only on the signs of k_x and $g\mathbf{H}_0$ but also on the sign of ε_{xz}, i.e. on the frequency. For fixed frequency and $\mathbf{H}_0$ the wave propagates in only one direction along the given boundary surface.

The penetration depth of a surface wave is $\delta \sim 1/\sqrt{b}$. The relations (2) and (12) yield

$$\delta^{-1} = \frac{8f\pi\omega^2\omega_H}{c\sqrt{(\Omega_1^2-\omega^2)(\Omega_2^2-\omega^2)(\omega_1^2-\omega^2)(\omega_2^2-\omega^2)}}. \tag{15}$$

Evidently, the penetration depth of the wave is inversely proportional to the magnitude of the constant magnetic field and depends strongly on the frequency. In the absence of a constant magnetic field the penetration depth is infinite, i.e. the waves are volume waves. In order of magnitude $\delta \sim c/\omega_H$. In the optical range, $\delta \sim 10^{-2}$ cm for $H \sim 10$ T and $\omega_H \sim 10^{12}$ s^{-1}. According to Eq. (17) the penetration depth can be even smaller near the frequencies ω_1, ω_2, Ω_1, and Ω_2. In thin films, where $l \sim d$, the wave is essentially a volume wave. We note that the field $e_x = 0$ in the surface waves studied here.

The heavy lines in Fig. 2 depict surface modes near $Z=0$ for $gH_0 > 0$ (or the modes near $Z=l$ for $gH_0 < 0$), and

TABLE I. Parameter values for surface modes in the case $gH_0 > 0$. For $gH_0 < 0$, k_x has the opposite sign in each frequency interval.

σ	k_x	ω	
+1	+	$0 < \omega < \omega_1$,	$\omega > \Omega_2$
	−	$\Omega_1 < \omega < \omega_2$	
−1	−	$0 < \omega < \omega_1$,	$\omega > \Omega_2$
	+	$\Omega_1 < \omega < \omega_2$	

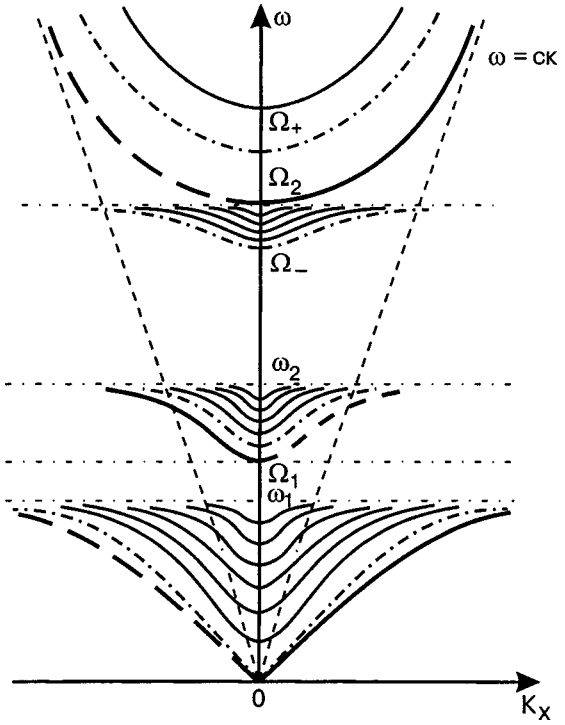

FIG. 2. Polariton modes of a metal-coated isotropic dielectric in a constant magnetic field. Fine lines—volume modes, dot-dash lines—volume modes in a semi-infinite dielectric, heavy and dashed lines—surface modes. For $gH_0>0$ the heavy lines correspond to surface modes near $Z=0$ and the dashed lines correspond to modes near $Z=l$ and vice versa for $gH_0<0$.

the dashed lines indicate surface modes near $Z=0$ for $gH_0<0$ (or surface modes near $Z=l$ for $gH_0>0$).

The fine lines in Fig. 2 depict volume modes, for which $|k_x|<\overline{k}$ and $b\leqslant 0$. Setting $\sqrt{b}=i\alpha$ and using the relations (7) we obtain the following expression for the real part of the magnetic field in the wave (6):

$$\mathrm{Re}\, h_y = 2A\frac{\alpha\varepsilon}{\varepsilon'^2 k_x^2+\alpha^2\varepsilon^2}(\alpha\varepsilon\cos\alpha z+\varepsilon' k_x\sin\alpha z),$$

$$\alpha=\frac{n\pi}{l};\quad n=0,1\ldots. \tag{16}$$

In weak fields, where $\varepsilon' k_x \ll \alpha\varepsilon$, the quantity h_y calculated using the expression (16) tends to the value h_y for $H_0=0$ (9). In the opposite limit $\varepsilon' k_x \gg \alpha\varepsilon$ (strong fields, large thickness l) we have

$$\mathrm{Re}\, h_y \approx 2A\frac{\alpha\varepsilon}{\varepsilon' k_x}\left(\sin\alpha z+\frac{\alpha\varepsilon}{\varepsilon' k_x}\cos\alpha z\right),\quad \alpha\varepsilon\ll\varepsilon' k_x. \tag{17}$$

It is evident from Eqs. (16) and (17) that a constant magnetic field (or an increase in the thickness of the dielectric layer) decreases the amplitude of the alternating field in a volume electromagnetic wave. In a prescribed constant field $\mathbf{H}_0$ in a semi-infinite dielectric ($l\to\infty$) $h_y\to 0$, and in the mode described by the dot-dash curve in Fig. 2 there is no electromagnetic field at all.

The dispersion law for volume modes in the presence of a magnetic field is

$$k_x=\pm\frac{\omega}{c}\sqrt{\varepsilon\left[1-\frac{\varepsilon'^2}{\varepsilon^2}-\frac{\lambda_n^2}{\varepsilon\omega^2}\right]}. \tag{18}$$

New frequency intervals $[\Omega_1,\omega_2]$ and $[\Omega_-,\Omega_2]$, where $\Omega_-\cong\Omega_2-\omega_H$, appear in a magnetic field. The width of these intervals is ω_H, and in these intervals if $|k_x|>\overline{k}$, surface polaritons with dispersion law (12) (heavy line in Fig. 2) exist and if $|k_x|<\overline{k}$, the volume polaritons (18) exist. All branches are radiation branches and have positive dispersion.

At high frequencies, just as in the absence of a magnetic field, there is an infinite number of volume modes but a field shifts the lower frequency limit, $\omega>\Omega_+\cong\Omega_2+\omega_H$. The modes are radiation modes and as frequency increases they approach the light line. Only one (bottom) volume branch is shown in Fig. 2.

As the thickness l of the dielectric layer increases, the volume modes contract toward the dot-dash curves, and the electromagnetic field in them tends to zero (17). In the limit of a semi-infinite dielectric in the presence of a constant magnetic field there are no volume polaritons, and in the spectrum in Fig. 2 only surface modes (heavy and dot-dash lines) remain.

4. CONCLUSIONS

It follows from the results presented that a constant magnetic field gives rise to surface polariton modes and causes the field of the electromagnetic wave to ''contract'' toward the lateral surfaces of the waveguide. The effect whereby the field is ''pressed'' against the lateral walls is well known in ferrite microwave waveguides and is used in rectifying devices.[11] Our analysis shows that this effect should also occur in the IR and optical ranges for dielectric waveguides in the presence of a constant magnetic field. A different number of surface modes, lying in different frequency intervals, arises in the dielectric (two near one wall and one near the other). A wave with a given frequency propagates along a given wall of the waveguide in only one direction. The ''choice of wall'' for a wave with a fixed frequency depends not only on the orientations of the magnetic field and the wave vector but also on the sign of the gyromagnetic ratio g, i.e. on the ionic ($g>0$) or electronic ($g<0$) type polarizability. Consequently, it is in principle possible to judge which contribution (electronic or ionic) to the polarization predominates in a given frequency interval by observing the nonreciprocal displacement of the field of a wave in the IR and optical ranges of the spectrum. Of course, the nonreciprocal displacement of a field will be more noticeable in films with thickness $l>\delta$ (δ is the penetration depth of the electromagnetic field (15)).

The influence of a constant magnetic field on volume modes is seen in the appearance of new narrow frequency bands $[\Omega_1,\omega_2]$ and $[\Omega_-,\Omega_2]$. However, as the magnetic field increases (just as when the thickness of the dielectric layer in a nonzero magnetic field increases), energy is transferred from volume into surface modes, i.e. a constant magnetic field pushes the alternating field of an electromagnetic wave onto the surface. This phenomenon could decrease losses during propagation of polaritons in a dielectric waveguide.

*E-Mail: chupis@ilt.kharkov.ua

[1] J. J. Brion, R. F. Wallis, A. Harstein, and E. Burstein, Phys. Rev. Lett. **28**, 1455 (1972); Surf. Sci. **34**, 73 (1973).
[2] K. W. Chiu and J. J. Quinn, Phys. Rev. B **5**, 4707 (1972).
[3] L. Hinchey and D. L. Mills, J. Appl. Phys. **57**, 3687 (1985).
[4] R. F. Wallis, R. Szenics, J. J. Quinn, and G. F. Giuliani, Phys. Rev. B **36**, 1218 (1987).
[5] R. F. Camley, Surf. Sci. Rep. **7**, 103 (1987).
[6] B. L. Johnson and R. E. Camley, Phys. Rev. B **38**, 3311 (1988).
[7] E. L. Albuquerque, P. Fulco, G. A. Farias, M. M. Auto, and D. R. Tilley, Phys. Rev. B **43**, 2032 (1991).
[8] I. E. Chupis, Ferroelectrics **204**, 173 (1997).
[9] I. E. Chupis and D. A. Mamaluy, J. Phys.: Condens. Matter **12**, 1413 (2000).
[10] *Surface Polaritons*, edited by V. M. Agranovich and D. L. Mills, North-Holland, Amsterdam (1982).
[11] A. G. Gurevich and G. A. Melkov, *Magnetic Oscillations and Waves*, Nauka, Moscow (1994).

Translated by M. E. Alferieff

The electron g factor for one-band and two-band extended models of the electron energy spectrum

G. P. Mikitik and Yu. V. Sharlai*

B. Verkin Institute for Low Temperature Physics and Engineering of the National Akademy of Sciences of Ukraine, 47 Lenin Ave., Kharkov 61103, Ukraine

(Submitted March 16, 2004)
Fiz. Nizk. Temp. **30**, 1293–1301 (December 2004)

At present, *explicit* expressions for the electron g factor in crystals are known only for the following two cases: when the Fermi energy ε_F of the electrons lies at the edge of the electron energy band, $\varepsilon(\mathbf{k}_{\rm ex})$, or when the electron energy spectrum of a crystal can be approximated by the two-band model. Here we obtain explicit formulas for the g factor in situations when the Fermi level ε_F is close to but does not coincide with the band edge and when the two-band model of the spectrum includes small corrections from other electron energy bands. In particular, we derive expressions that describe the dependences of the g factor on $\varepsilon_F-\varepsilon(\mathbf{k}_{\rm ex})$ and on the magnetic field direction for doped semiconductors. The results are applied to III–V semiconductors and to bismuth. © *2004 American Institute of Physics.*
[DOI: 10.1063/1.1820038]

1. INTRODUCTION

As is well known,[1] the g factor of electrons in crystals with inversion symmetry specifies the splitting of Landau energy levels caused by an interaction of the electron spin with a magnetic field, $\Delta E=g(e\hbar/2mc)H$, and can differ considerably from its free-electron value, $g=2$. Here e and m are the charge and mass of an electron, and H is the external magnetic field. In this paper we shall discuss the g factors in the semiclassical limit when there are many Landau levels under the Fermi surface of the crystal. Besides this, we exclude from consideration those situations in which magnetic breakdown occurs. In this case the semiclassical g factor appears in the well-known quantization rule[1–4] for the electron energy ε in a magnetic field,

$$S(\varepsilon,k_H)=2\pi\frac{|e|H}{\hbar c}\left(n+\gamma\pm\frac{g(\varepsilon,k_H)m^*}{4m}\right), \tag{1}$$

where S is the cross-sectional area of the closed semiclassical orbit Γ of the electron in the Brillouin zone, k_H is the component of the wave vector of the electron in the direction of the external magnetic field $\mathbf{H}$, n is a large integer, the cyclotron mass $m^*=(\hbar^2/2\pi)(\partial S(\varepsilon,k_H)/\partial\varepsilon)$, the constant γ is always equal to 1/2 when the spin–orbit interaction is taken into account,[5,6] and the g factor $g(\varepsilon,k_H)$ depends on the location of the orbit Γ in the Brillouin zone.[7]

The exact equations for the g factor were derived in Refs. 5, 8. (In fact, they are another representation of Roth's results.[9]) These equations take into account the dynamics of the electron spin when the electron moves in its semiclassical orbit. For this reason the g factor depends on the entire orbit and is usually not expressed in explicit form. On the other hand, in many papers (see, e.g., Refs. 10–26) the so-called local g factors $g(\mathbf{k})$ introduced by De Graaf and Overhauser[27] for points $\mathbf{k}$ on the Fermi surface were calculated, and the g factor of the orbit was obtained by integration of $g(\mathbf{k})$ over the orbit. In this simplified approach the dynamics of the electron spin is neglected completely. As was shown in our previous papers,[8,28] the simplified approach is approximately valid if the spin–orbit interaction in the crystal is not too strong. Besides this, at an arbitrary strength of this interaction there are two situations when the simplified approach leads to the exact result for the g factor.

In the first situation, which is characteristic of doped semiconductors, the Fermi level of the electrons practically coincides with a minimum (or a maximum) of the electron energy band $\varepsilon(\mathbf{k})$, and hence this $\varepsilon(\mathbf{k})$ can be well approximated by the "one-band" model,

$$\varepsilon(\mathbf{k})\approx\varepsilon(\mathbf{k}_{\rm ex})+\sum_{\alpha=x,y,z}\frac{\hbar^2(k_\alpha-k_{{\rm ex},\alpha})^2}{2m_\alpha}, \tag{2}$$

where $\mathbf{k}_{\rm ex}$ is the point of the energy-band extremum in the Brillouin zone, and m_α are all positive (or negative) effective masses at this point. In this case the electron orbit takes the shape of a very small ellipse surrounding the point $\mathbf{k}_{\rm ex}$, and the g factor of the orbit coincides to a first approximation with the local g factor $g(\mathbf{k}_{\rm ex})$.

In the second situation the electron energy spectrum of the crystal can be well approximated by the two-band model.[28] The two-band model can be applied to the description of the energy spectrum if in some region of the Brillouin zone the energy gap between the band under consideration and some other band as well as the energy differences between these bands and the Fermi energy ε_F are all relatively small as compared to other energy gaps in the crystal. (Then one may consider only these two bands, neglecting the other bands of the crystal.) In this case the energy dispersion relations $\varepsilon(\mathbf{k})$ for both the bands are found from a quadratic equation that can be always reduced to the form

$$\left[\varepsilon-\frac{[\mathbf{v}_0(0)+\mathbf{v}_a(0)]\mathbf{k}}{2}\right]^2=\left[\frac{E_g}{2}+\frac{[\mathbf{v}_0(0)-\mathbf{v}_a(0)]\mathbf{k}}{2}\right]^2+q_1^2k_x^2+q_2^2k_y^2+q_3^2k_z^2, \tag{3}$$

where $\mathbf{v}_0(0)$, $\mathbf{v}_a(0)$, q_1, q_2, q_3 are some real constants, and E_g is the energy gap between these bands at some point of the above-mentioned region of the Brillouin zone (we take this point as $\mathbf{k}=0$). For example, the electron energy spectrum of bismuth and its alloys near the point L of the Brillouin zone is close to this type. The two-band model can be also useful for narrow-gap semiconductors. In this two-band case the appropriate equation[8] determining the g factor can be solved explicitly,[28] and the result for the g factor of the electron orbit (this orbit need not be small now) coincides with that obtained in the framework of the local g factor approach. Interestingly, in this case the combination $\delta \equiv gm^*/4m$ is equal to $\pm 1/2$,[29] i.e., the magnetic-field splitting of the electron energy levels described by the g factor coincides exactly with their orbital splitting. This result generalizes the well-known finding of Cohen and Blount[30] obtained for a simplified variant of the two-band model.[31]

The above exactly solvable cases can be applied to real situations only approximately. In particular, the Fermi energy in doped semiconductors does not lie strictly at the edge of the energy band, and thus the electron orbits have a small but finite size. In that case, the g factors of such orbits differ slightly from the g factor calculated at the edge of the band, $g(\mathbf{k}_{\rm ex})$. Since g factors are measured with high accuracy,[32,33] the correction $\Delta g \equiv g - g(\mathbf{k}_{\rm ex})$ was investigated experimentally in a number of semiconductors.[34] It is clear that to calculate this correction, one has to go beyond the framework of the local g factor approach. As to the two-band model, it describes the energy spectrum of bismuth sufficiently well when the wave vector $\mathbf{k}$ is perpendicular to the longest axis of its Fermi surface at the point L, i.e., this model is good enough for magnetic fields directed along this axis. When the magnetic field deviates from the longest axis, corrections to the g factor of the two-band model have been observed experimentally in bismuth,[35] and accurate calculation of the g factor is possible only if one goes beyond the framework of the two-band model (and of the local g factor approach).

In this paper we consider one-band and two-band extended models of the electron spectrum which include small corrections to the above exactly solvable cases. These models enable one to describe the electron energy spectra in a number of real situations. In the framework of these extended models we find *explicit* formulas for the g factor, using the theory.[8] In particular, the case of doped semiconductors is analyzed in detail. As an illustration, the results obtained are applied to III–V semiconductors and to bismuth.

2. CALCULATION OF THE *g* FACTOR

The g factor in the quantization rule (1) is expressed in terms of the matrix elements of the effective one-band Hamiltonian $\hat{H}_{\rm eff}$ of a Bloch electron in a magnetic field. Since the electron bands are twofold degenerate in crystals with inversion symmetry,[4] the Hamiltonian is a 2×2 matrix in the spinor space. This Hamiltonian to first order in the magnetic field H has the form[36,37]

$$\hat{H}_{\rm eff} = \varepsilon(\hat{\mathbf{k}})\hat{\mathbf{1}} + \frac{e}{c} H \hat{\mu}(\hat{\mathbf{k}}, \mathbf{n}), \tag{4}$$

where $\mathbf{n}$ is a unit vector directed along the magnetic field $\mathbf{H}$, $\varepsilon(\mathbf{k})$ is the electron dispersion relation for the band being investigated, $\hat{\mathbf{k}} = \mathbf{K} - (e/c\hbar)\mathbf{A}(i\partial/\partial \mathbf{K})$, $\mathbf{A}(\mathbf{r})$ is the vector potential of the magnetic field $\mathbf{H}$, and the function $\varepsilon(\hat{\mathbf{k}})$ in Eq. (4) is assumed to be completely symmetrized in the components of $\hat{\mathbf{k}}$. The 2×2 matrix $[eH\hat{\mu}(\mathbf{k},\mathbf{n})/c]$ describes the interaction of the electron spin with the magnetic field in the crystals, and its elements satisfy the relations $\mu_{11} = -\mu_{22}$, $\mu_{12} = \mu_{21}^*$. In Ref. 8 (Appendix) it was shown how to calculate this matrix explicitly when one starts from the so-called $\mathbf{k}\cdot\mathbf{p}$ Hamiltonian[4] or from the Hamiltonian in the LMTO representation.[38] Dependences of the matrix $\hat{\mu}$ on $\mathbf{k}$ and on $\mathbf{n}$, up to numerical factors, can be also found using the theory of invariants.[39]

In Appendix A of this paper we present the equations of Ref. 8 for the g factor and find the g factors for the one-band and two-band models of the spectrum. Let us denote the energy dispersion relation and the matrix $\hat{\mu}$ for the energy band under consideration in these exactly solvable cases as $\varepsilon^{(0)}(\mathbf{k})$ and $\mu^{(0)}_{\rho\rho'}(\mathbf{k})$ $(\rho,\rho' = 1,2)$. Below we shall consider models for which one may write

$$\varepsilon(\mathbf{k}) = \varepsilon^{(0)}(\mathbf{k}) + \Delta\varepsilon(\mathbf{k}), \tag{5}$$

$$\mu_{\rho\rho'}(\mathbf{k}) = \mu^{(0)}_{\rho\rho'}(\mathbf{k}) + \Delta\mu_{\rho\rho'}(\mathbf{k}), \tag{6}$$

where the terms $\Delta\varepsilon(\mathbf{k})$, $\Delta\mu_{\rho\rho'}(\mathbf{k})$ are small corrections. Assuming that these corrections are known, we shall find the appropriate corrections to the g factors of the electron orbits for these extended models. Note that the orbits are slightly deformed by the term $\Delta\varepsilon(\mathbf{k})$ in Eq. (5). The appropriate deformation is found in Appendix B.

To find the g factor, we have to solve Eq. (A2). Note that it is always possible to reduce the matrix $c_{\rho\rho'}$ in Eq. (A5) to diagonal form by a constant unitary transformation in the spinor space. Thus, without loss of generality we may assume that $c_{11} = -c_{22} = \lambda$, $c_{12} = c_{21} = 0$, with λ from Eq. (A6). Then Eq. (A2) takes the form

$$i\frac{\hbar c}{|e|H}\dot{\tau} = 2\lambda\tau\psi(\mathbf{k}) + \Delta\mu_{12}(\mathbf{k})\tau^2 + 2\Delta\mu_{11}(\mathbf{k})\tau - \Delta\mu_{12}^*(\mathbf{k}), \tag{7}$$

where $\mathbf{k} = \mathbf{k}[t,\varepsilon]$ (see Appendix B). The solution of this equation can be represented in the form

$$\tau(t) \approx C e^{-i\varphi(t)} + \Delta\tau(t),$$

where the first term is the solution of Eq. (7) at $\Delta\mu_{\rho\rho'} = 0$; C is some complex constant which is to be found from the boundary condition (A3); $\Delta\tau$ is a small correction proportional to $\Delta\mu_{\rho\rho'}$, and

$$\varphi(t) = 2\frac{\lambda|e|H}{\hbar c}\int_0^t dt'\,\psi(\mathbf{k}[t',\varepsilon]). \tag{8}$$

Inserting $\tau(t)$ thus obtained into Eq. (A4), we eventually arrive at

$$\Delta g \equiv g(\varepsilon,k_H) - g^{(0)}(\varepsilon^{(0)},k_H) = \frac{m}{m^*}\frac{\Delta\varphi}{\pi} + \frac{4m}{\hbar}[\overline{\Delta\mu_{11}} + \mathrm{Re}(\overline{\Delta\mu_{12}}C)], \tag{9}$$

where the first term is due to the deformation of the electron orbit [i.e., it is caused by $\Delta\varepsilon(\mathbf{k})$],

$$\Delta\varphi \equiv \varphi(T) - \varphi^{(0)}(T),$$

the function $\varphi^{(0)}(T)$ is given by formula (8), but with $\mathbf{k}[t',\varepsilon]$ replaced by $\mathbf{k}^{(0)}[t',\varepsilon^{(0)}]$ in the argument of ψ (note that according to Eq. (A7), one has $m\varphi^{(0)}(T)/(\pi m^*) = g^{(0)}$); the bar over $\Delta\mu_{\rho\rho'}$ means time averaging over the period T:

$$\overline{\Delta\mu_{\rho\rho'}} = \frac{1}{T}\int_0^T dt' \Delta\mu_{\rho\rho'}(\mathbf{k}^{(0)}[t',\varepsilon^{(0)}]) e^{i\varphi^{(0)}(t)(\rho-\rho')},$$

and the constant C is determined from the equation

$$\overline{\Delta\mu_{12}}C^2 + 2\left(\overline{\Delta\mu_{11}} + i\hbar\frac{1-e^{i\varphi(T)}}{2\mu m^*}\right)C - (\overline{\Delta\mu_{12}})^* = 0. \tag{10}$$

It should also be emphasized that we are finding the difference in the g factors calculated at different energies ε and $\varepsilon^{(0)}$. However, since the difference $\varepsilon - \varepsilon^{(0)}$ is small (Appendix B) and we calculate Δg to first order in $\Delta\varepsilon(\mathbf{k})$, $\Delta\mu_{\rho\rho'}$, we may neglect the difference between ε and $\varepsilon^{(0)}$ in Eq. (9).

In the case of the one-band model (Appendix A), the function $\psi \equiv 1$, and thus $\Delta\varphi \equiv 0$. This means that in this case Δg determined only by $\Delta\mu_{\rho\rho'}$ rather than by $\Delta\varepsilon(\mathbf{k})$. Moreover, if the combination $\delta^{(0)} \equiv g^{(0)}m^*/4m$ is not close to an integer or a half-integer (i.e., if the appropriate difference is considerably larger than $m^*|\overline{\Delta\mu_{12}}|/\hbar$), the constant C is relatively small, and the third term in Eq. (9) may be omitted. Then we arrive at the simple formula

$$\Delta g = \frac{4m\overline{\Delta\mu_{11}}}{\hbar}. \tag{11}$$

In the case of the two-band model (Appendix A), Δg depends on both $\Delta\mu_{\rho\rho'}$ and $\Delta\varepsilon(\mathbf{k})$. Besides this, since in this case the electron energy levels in the magnetic field are doubly degenerate ($\delta^{(0)} = \pm 1/2$), the constant C is not small, and it follows from Eqs. (9), (10) that

$$\Delta g = \sqrt{\left(\frac{m}{m^*}\frac{\Delta\varphi}{\pi} + \frac{4m\overline{\Delta\mu_{11}}}{\hbar}\right)^2 + \left|\frac{4m\overline{\Delta\mu_{12}}}{\hbar}\right|^2}. \tag{12}$$

3. SEMICONDUCTORS

To apply our results to semiconductors, let us consider more closely the case of the one-band model of the electron energy spectrum, Eq. (2). Assuming that the energy is measured from the band edge $\varepsilon(\mathbf{k}_{\rm ex})$ and the wave vector $\mathbf{k}$ from $\mathbf{k}_{\rm ex}$, Eq. (2) is rewritten as follows:

$$\varepsilon^{(0)}(\mathbf{k}) = \sum_{\alpha=x,y,z} \hbar^2 k_\alpha^2 (2m_\alpha)^{-1}, \tag{13}$$

where k_α are the components of $\mathbf{k}$. As was mentioned above, in the one-band case the correction Δg depends only on $\Delta\mu_{\rho\rho'}$ rather than on the correction to the energy dispersion relation, $\Delta\varepsilon$. Thus it is sufficient to consider only $\Delta\mu_{\rho\rho'}$ here. Since $\mu^{(0)}_{\rho\rho'}$ is a constant matrix (Appendix A), the first correction to it is proportional to $\mathbf{k}$. However, this linear correction may be identically equal to zero due to symmetry of the crystal, and so we shall treat both the linear and the quadratic corrections to $\mu^{(0)}_{\rho\rho'}$:

$$\mu(\mathbf{k}) = \hat{c} + \sum_{\alpha=x,y,z} \hat{b}^\alpha k_\alpha + \sum_{\alpha,\beta=x,y,z} \hat{a}^{\alpha\beta} k_\alpha k_\beta, \tag{14}$$

where $\hat{c} \equiv \hat{\mu}^{(0)}$, and $\hat{b}^\alpha$, $\hat{a}^{\alpha\beta}$ are some constant matrices. The matrices $\hat{\mu}^{(0)}$, $\hat{b}^\alpha$, $\hat{a}^{\alpha\beta}$ depend only on the unit vector $\mathbf{n} \equiv \mathbf{H}/H$.

It should be also noted that formula (11) was derived in the representation in which the matrix c is diagonal. If this matrix is not assumed to be diagonal, formula (11) transforms into

$$\Delta g = \frac{4m}{\hbar T}\int_0^T dt \frac{c_{11}\Delta\mu_{11} + \mathrm{Re}(c_{12}^*\Delta\mu_{12})}{\lambda}, \tag{15}$$

where $\lambda = \sqrt{c_{11}^2 + |c_{12}|^2} = \sqrt{-\mathrm{Det}(\hat{c})}$. Using Eqs. (15) and (14), we find that

$$\Delta g = \frac{2m}{\hbar\lambda}\left(a_s\left[\frac{m_n\varepsilon}{\hbar^2} - \frac{k_H^2}{2}\right] + b_n k_H + a_n k_H^2\right), \tag{16}$$

where $k_H = \mathbf{n}\cdot\mathbf{k}$; $\mathbf{n} = \mathbf{H}/H$, and the $\mathbf{n}$-dependent parameters m_n, b_n, a_n, a_s are expressed via traces of the matrices $\hat{c}$, $\hat{b}^\alpha$, $\hat{a}^{\alpha\beta}$ as follows:

$$m_n = \sum_{\alpha=x,y,z} m_\alpha n_\alpha^2,$$

$$b_n = m_n^{-1}\sum_{\alpha=x,y,z} n_\alpha m_\alpha \mathrm{Tr}(\hat{c}\hat{b}^\alpha),$$

$$a_n = m_n^{-2}\sum_{\alpha,\beta=x,y,z} n_\alpha n_\beta m_\alpha m_\beta \mathrm{Tr}(\hat{c}\hat{a}^{\alpha\beta}),$$

$$a_s = m_n^{-1}\sum_{\alpha=x,y,z} m_\alpha \mathrm{Tr}(\hat{c}\hat{a}^{\alpha\alpha}) - a_n.$$

Experimental investigations of the oscillation effects enable one to measure the g factors of the electron orbits lying in the extremal cross sections of the Fermi surface (with respect to k_H).[1] For spectrum (13) the extremal cross sections correspond to $k_H = 0$, and for such orbits we obtain from Eq. (16)

$$\Delta g(\varepsilon, k_H = 0) = \varepsilon\frac{2mm_n}{\hbar^3\lambda}a_s. \tag{17}$$

Formulas (16) and (17) are the main result of this Section. For a given matrix $\Delta\mu_{\rho\rho'}(\mathbf{k},\mathbf{n})$ they enable one to find Δg *explicitly* for various ε, k_H, and magnetic field directions $\mathbf{n}$. However, these formulas fail for values of $\delta^{(0)} \equiv g^{(0)}m^*/4m$ such that $\sin(2\pi\delta^{(0)}) \approx 0$; see Sec. 2. A more accurate estimate of the condition under which Eqs. (16) and (17) hold true yields

$$\left|\frac{\sin(2\pi\delta^{(0)})}{2\pi}\right| \gg \left|\frac{\Delta g m^*}{4m}\right|. \tag{18}$$

Note that the intervals of $\delta^{(0)}$ where Eqs. (16), (17) fail are very narrow when Δg is small.

4. EXAMPLES

III–V semiconductors

As an example, we consider the III–V semiconductors, and in particular, the well-known GaAs, which are widely used in practice. The semiconductors of this class have the zinc-blende crystal structure with the point of the band extremum, k_{ex}, being in the center of the Brillouin zone, i.e., $k_{ex}=0$. These semiconductors have no center of inversion, and strictly speaking, the electron energy levels in these crystals are nondegenerate in spin even without a magnetic field. However, near the center of the Brillouin zone this splitting of the electron energy levels caused by the spin–orbit interaction is considerably less[40] than the splitting $\Delta E = g(e\hbar/2mc)H$ caused by the magnetic field that is usually applied to the samples in experiments. In this context the concept of the g factor is justified and is commonly used to describe the electron energy levels in magnetic field for III–V semiconductors.

The correction Δg has been investigated experimentally in these semiconductors, and it was found that[34]

$$\Delta g(\varepsilon)=\beta\varepsilon \tag{19}$$

for the extremal cross sections ($k_H=0$). The coefficient β varies from 144 eV^{-1} for InSb to 2.2 eV^{-1} for InP. Note that relation (19), found experimentally, is in complete agrement with our result, Eq. (17).

Let us take the axes of the coordinate system along the principal crystal axes. Then the energy dispersion relation for these compounds has the form of Eq. (13) with $m_1=m_2=m_3=m^*$, and the matrix $\hat{\mu}(\mathbf{k},\mathbf{n})$ can be written as[40,41]

$$\frac{e}{c}\hat{\mu}(\mathbf{k},\mathbf{n})=\frac{g^{(0)}}{2}\mu_B(\hat{\sigma}\mathbf{n})+a_4\mathbf{k}^2(\hat{\sigma}\mathbf{n})+2a_5(\hat{\sigma}\mathbf{k})(\mathbf{kn}) + a_6(\hat{\sigma}_x k_x^2 n_x+\hat{\sigma}_y k_y^2 n_y+\hat{\sigma}_z k_z^2 n_z), \tag{20}$$

where $\mathbf{n}=\mathbf{H}/H$, μ_B is the Bohr magneton, $g^{(0)}$ is the g factor at the band edge, and a_4, a_5, and a_6 are some constant real parameters (expressions for these parameters in terms of the band-structure parameters can be found in Ref. 41). The first term in this expression describes $\hat{\mu}^{(0)}=c$ [see Eqs. (6) and (14)], while the other terms in Eq. (20) give $\Delta\mu_{\rho\rho'}$. Note that the term linear in $\mathbf{k}$ is absent. Inserting these $\Delta\mu_{\rho\rho'}$ into formula (16), we immediately arrive at

$$\Delta g(\varepsilon,k_H)=\frac{8mm^*}{\hbar^3|e|}\left[a_4\varepsilon+2a_5\frac{\hbar^2k_H^2}{2m^*}+a_6\left(\varepsilon F(\theta,\varphi) + \frac{\hbar^2k_H^2}{2m^*}(1-3F(\theta,\varphi))\right)\right], \tag{21}$$

where

$$F(\theta,\varphi)=\frac{1}{2}\left(1-\sum_{\alpha=x,y,z}n_\alpha^4\right) =\sin^2\theta(\sin^2\theta\cos^2\varphi\sin^2\varphi+\cos^2\theta),$$

and the angles θ and φ are defined as follows:

$$\mathbf{n}=(\sin\theta\cos\varphi,\sin\theta\sin\varphi,\cos\theta).$$

Expression (21) completely agrees with that calculated in Ref. 40. At $k_H=0$, formula (21) yields

$$\Delta g(\varepsilon)=\frac{8mm^*c\varepsilon}{|e|\hbar^3}(a_4+a_6F(\theta,\varphi)), \tag{22}$$

i.e., we obtain an expression for the coefficient β in relation (19). For the case $\varphi=\pi/4$ formula (22) coincides with that derived in Ref. 41 by another method, and it very well describes the experimental angular dependences of Δg for GaAs.[42]

According to Ref. 34, one has $g^{(0)}=-0.44$ and $\beta\approx 6.3$ eV^{-1} for GaAs. But it is well known that even a small amount of Al significantly shifts $g^{(0)}$ to positive values. This property of the compound $\mathrm{Al}_x\mathrm{Ga}_{1-x}\mathrm{As}$ is now used in spintronic devices.[43] At a concentration $x\approx 0.1$ the electron g factor $g^{(0)}\approx 0$. Then condition (18) fails, and Eq. (9) must be used to calculate Δg. Eventually, in the region of concentrations x where $g^{(0)}\approx 0$, we obtain

$$\Delta g=\frac{8mm^*c\varepsilon}{\hbar^3|e|}\sqrt{[a_4+a_6F(\theta,\varphi)]^2+a_6^2G(\theta,\varphi)}, \tag{23}$$

where

$$G(\theta,\varphi)=\frac{\sin^6\theta}{64}[\cos^2\theta(\cos 4\varphi+7)+\sin^2 4\varphi].$$

Note that the angular dependence of Δg described by Eq. (23) differs noticeably from that given by Eq. (22).

Bismuth

In bismuth near the symmetry points L of its Brillouin zone there are two bands, $\varepsilon_0(\mathbf{k})$ and $\varepsilon_a(\mathbf{k})$, which are close to each other and to the Fermi energy.[1,35] (These bands, which we denote by subscripts 0 and a, are separated by a gap $E_g=\varepsilon_0-\varepsilon_a\sim 10$ meV at this point.) The electron Fermi surface of Bi consists of three ''ellipsoids'' located near the three L points. The symmetry of this point is C_{2h}. It is common practice to put the origin of the coordinate system (i.e., the point $\mathbf{k}=0$) at L, to take the x axis along the twofold axis C_2, to place the yz plane on the reflection plane σ_h, and to choose the y axis in the direction of the longest principal axis of the ellipsoid (this axis is approximately ten times longer than the other two). Since the Fermi surface of bismuth is elongated in the k_y direction, the two-band model is not sufficient to describe the electron energy spectrum in this direction, and the following extended two-band model of McClure[44,45] is commonly used:

$$\left[\varepsilon-\frac{(\alpha_0-\alpha_a)k_y^2}{4}\right]^2=\left[\frac{E_g}{2}+\frac{(\alpha_0+\alpha_a)k_y^2}{4}\right]^2+q_1^2k_x^2 + |q_2|^2k_y^2+q_3^2k_z^2, \tag{24}$$

where the energy ε is measured from the middle of the energy gap E_g at the L point; α_0, α_a, q_1, and q_3 are real parameters of the model, while q_2 is an imaginary constant, $\mathrm{Re}(q_2)=0$. The values of all these parameters are well known.[46,47] It is essential that the value of $|q_2|$ is relatively small. It is for this reason that the Fermi surface is elongated in the k_y direction, and the terms $\alpha_0k_y^2$, $\alpha_ak_y^2$ are taken into account. Without these terms, Eq. (24) reduces to the two-band model.

The g factors of the central cross sections of the Fermi surface of Bi have been measured with high accuracy.[35]

When the magnetic field is directed along y, one has $k_y=0$ for the central cross section, and Eq. (24) reduces to the two-band model. This model describes the spectrum of bismuth sufficiently well in this situation, and hence $\delta \equiv gm^*/4m \approx 1/2$. If the magnetic field deviates from the y axis, a correction to this two-band result appears. This correction was calculated in Ref. 28 for an arbitrary angle between **H** and the y axis. Here we shall consider the terms with α_0 and α_a as small corrections and shall find Δg for the conduction band $\varepsilon_0(\mathbf{k})$, using Eq. (12). It is clear that this approach is valid at sufficiently small angles η between **H** and the y axis.

It follows from Eq. (24) that

$$\varepsilon_0(\mathbf{k})=\varepsilon_0^{(0)}(\mathbf{k})+\Delta\varepsilon,$$

$$\varepsilon_0^{(0)}(\mathbf{k})=\sqrt{(E_g/2)^2+q_1^2k_x^2+|q_2|^2k_y^2+q_3^2k_z^2},$$

$$\Delta\varepsilon=\frac{(\alpha_0-\alpha_a)k_y^2}{4}+\frac{E_g}{2\varepsilon_0^{(0)}(\mathbf{k})}\,\frac{(\alpha_0+\alpha_a)k_y^2}{4}.$$

The matrix elements of $\hat{\mu}_0$ for the central cross sections of the Fermi surface of Bi were calculated in Ref. 28. They are

$$\mu_{0,11}(\varepsilon)\equiv\mu_{11}^{(0)}+\Delta\mu_{11}=A[-iBq_2q_3n_x+\tilde{\rho}_0(E_a-\varepsilon)^2 +\tilde{\rho}_a(t^2-|u|^2)+t(\tilde{\nu}_a u^*+\tilde{\nu}_a^* u)], \tag{25}$$

$$\mu_{0,12}(\varepsilon)\equiv\mu_{12}^{(0)}+\Delta\mu_{12}=A[iBq_1(q_3n_y-q_2n_z)-2\tilde{\rho}_a tu +\tilde{\nu}_0(E_a-\varepsilon)^2+\tilde{\nu}_a t^2-\tilde{\nu}_a^* u^2], \tag{26}$$

where

$$A=[(E_a-\varepsilon)(E_0+E_a-2\varepsilon)]^{-1};$$

$$B=(E_a+E_g+\varepsilon)/\hbar;\quad E_{0,a}(\mathbf{k})=\pm\left(\frac{E_g}{2}+\frac{\alpha_{0,a}}{2}k_y^2\right);$$

$$t=q_1k_x;\quad u=q_2k_y+q_3k_z,$$

and

$$\tilde{\rho}_{0,a}=\rho_{0,a}n_x,\tilde{\nu}_{0,a}=\nu_{0,a}^y n_y+\nu_{0,a}^z n_z.$$

Here n_i are the components of the vector $\mathbf{n}=\mathbf{H}/H$; ρ_0 and ρ_a are some real constants, and ν_0^y, ν_a^y, ν_0^z, ν_a^z are constant complex parameters. The matrix $\hat{\mu}^{(0)}$ is obtained from Eqs. (25), (26) by setting $\rho_{0,a}=\nu_{0,a}^y=\nu_{0,a}^z=\alpha_{0,a}=0$. Note that Eqs. (25), (26) take into account corrections to the two-band model even for magnetic field directed along the y axis ($n_x=n_y=0$).

Using Eq. (12), we obtain

$$\delta\approx\frac{1}{2}+\frac{\varepsilon}{2\Lambda}\left[\hbar|q_2|q_3n_x^2\overline{\rho}+\frac{1}{8}(q_1^2n_z^2+q_3^2n_x^2)\left(1-\frac{E_g}{2\varepsilon}\right)\overline{\alpha} +\hbar q_1\,\mathrm{Im}([q_3n_y+i|q_2|n_z][\overline{\nu^y}n_y+\overline{\nu^z}n_z])\right], \tag{27}$$

where

$$\Lambda=n_y^2q_1^2q_3^2+n_z^2q_1^2|q_2|^2+n_x^2|q_2|^2q_3^2,$$

$$\overline{\rho}=\rho_a\left[1-\frac{E_g}{2\varepsilon}\right]-\rho_0\left[1+\frac{E_g}{2\varepsilon}\right],$$

$$\overline{\nu}^\beta=\nu_a^\beta\left[1-\frac{E_g}{2\varepsilon}\right]+\nu_0^\beta\left[1+\frac{E_g}{2\varepsilon}\right],$$

$$\overline{\alpha}=\alpha_0\left[1+\frac{E_g}{2\varepsilon}\right]-\alpha_a\left[5+\frac{E_g}{2\varepsilon}\right],$$

with $\beta=y,z$. Formula (27) can be further simplified if one takes into account that this expression is valid only for $n_y\neq 0$ and that the ratio $(|q_2|^2/q_1q_3)$ is of the order of 10^{-2} in bismuth.[46,47] Then we may put $\Lambda\approx n_y^2q_1^2q_3^2$, and eventually we find

$$\delta\approx\delta(0)+C_1\tan\eta\cos\zeta+\tan^2\eta[C_{2x}\sin^2\zeta +C_{2z}\cos^2\zeta], \tag{28}$$

where the following parametrization for the vector $\mathbf{n}\equiv\mathbf{H}/H$ has been used: $\mathbf{n}=(\sin\eta\sin\zeta,\cos\eta,\sin\eta\cos\zeta)$. The quantity $\delta(0)$ is the value of δ for magnetic field directed along y, i.e., when the angle η between **H** and this axis is zero. Note that this $\delta(0)$ differs from 1/2 if the parameter $\overline{\nu^y}$ has an imaginary part,

$$\delta(0)=\frac{1}{2}+\frac{\hbar\varepsilon}{2q_1q_3}\,\mathrm{Im}\,\overline{\nu^y}.$$

The constants C_1, C_{2x}, C_{2z} are

$$C_1=\frac{\hbar\varepsilon}{2q_1q_3^2}(q_3\,\mathrm{Im}\,\overline{\nu^z}+|q_2|\mathrm{Re}\,\overline{\nu^y}),$$

$$C_{2x}=\frac{\hbar\varepsilon|q_2|}{2q_1^2q_3}\overline{\rho}+\frac{\varepsilon-E_g/2}{16q_1^2}\overline{\alpha},$$

$$C_{2z}=\frac{\hbar\varepsilon|q_2|}{2q_1q_3^2}\mathrm{Re}\,\overline{\nu^z}+\frac{\varepsilon-E_g/2}{16q_3^2}\overline{\alpha}.$$

It is clear from these formulas that an experimental investigation of angular dependences of δ in the xy and yz planes (i.e., in the planes $\zeta=\pi/2$ and $\zeta=0$) near the y direction would enable one to measure $\delta(0)$, C_1, C_{2x}, C_{2z} and hence to extract the parameters $\mathrm{Im}\,\overline{\nu^y}$, $q_3\,\mathrm{Im}\,\overline{\nu^z}+|q_2|\mathrm{Re}\,\overline{\nu^y}$, $\mathrm{Re}\,\overline{\nu^z}$, and $\overline{\rho}$ from the appropriate experimental data.

In Fig. 1 we compare the δ obtained using the explicit formula (28) with the δ calculated numerically in Ref. 28. Note that in Ref. 28 the terms $\alpha_0k_y^2$ and $\alpha_ak_y^2$ were not assumed to be small, and hence the results for δ are valid even at $\eta\sim\pi/2$. Interestingly, the approximate formula (28) describes δ quantitatively even if the vector **n** deviates substantially from the y axis.

APPENDIX A: FORMULAS FOR THE *g* FACTOR

Here we present the equations determining the g factor[5,8] and the solutions of these equations[28] for the cases of the one-band and two-band models of the electron energy spectrum.

As is well known,[4] in the semiclassical approximation an electron in a crystal in a magnetic field **H** may be considered

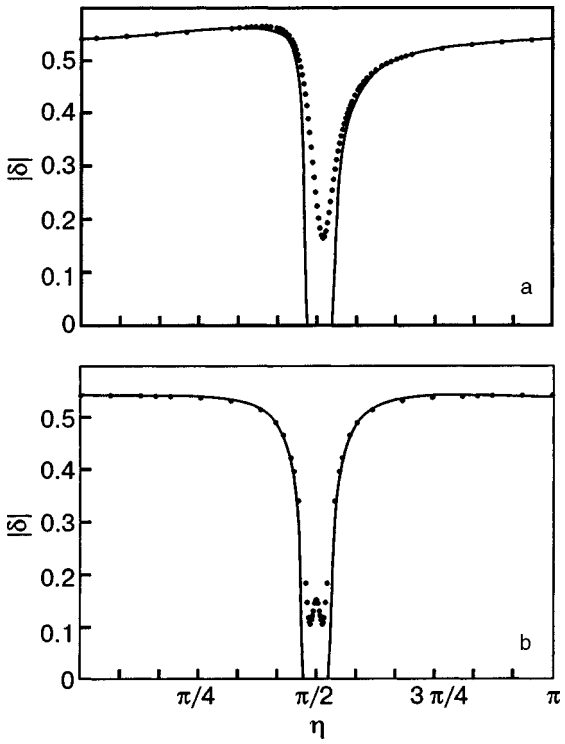

FIG. 1. The dependence of $\delta \equiv gm^*/4m$ on the magnetic field direction in Bi, Eq. (28), (solid lines). The values of the parameters are the same as in Ref. 28. The magnetic field lies either in the yz plane (a) or in the xy plane (b). The angle η is measured from the y axis; the positive direction of y is taken as in Ref. 35. The dotted lines show the appropriate results of Ref. 28, which well describe the experimental data.[35]

as a wave packet, with the wave vector of the packet $\mathbf{k}$ moving in an orbit[7] Γ in the Brillouin zone. The dependence of the wave vector $\mathbf{k}$ on the time t can be found from the equation

$$\hbar \dot{\mathbf{k}} = \frac{|e|}{c}[\mathbf{H} \times \nu(\mathbf{k})], \tag{A1}$$

where the electron velocity is given by

$$\mathbf{v}(\mathbf{k}) = \frac{1}{\hbar}\frac{\partial \varepsilon(\mathbf{k})}{\partial \mathbf{k}}.$$

During the electron motion in the orbit Γ, the direction of its spin $\mathbf{s}$ changes due to the spin–orbit interaction. To describe the direction of the electron spin in the semiclassical approximation, we introduce a complex parameter $\tau(\mathbf{k})$ that defines the components of the electron wave function $\Psi(\mathbf{k})$ in the spinor space of the Hamiltonian (4) as follows:

$$\Psi(\mathbf{k}) \propto \begin{pmatrix} 1 \\ \tau \end{pmatrix}.$$

This definition leads to the following representation of the electron spin at the point $\mathbf{k}$ of the semiclassical orbit:

$$\mathbf{s} = \frac{1}{2}\frac{(2\,\mathrm{Re}\,\tau, 2\,\mathrm{Im}\,\tau, 1-|\tau|^2)}{1+|\tau|^2}.$$

Then the dynamics of the electron spin may be described by a function $\tau(t)$. This function obeys the equation[5,8]

$$i\hbar\dot{\tau} = \frac{|e|H}{c}(\mu_{12}\tau^2 + 2\mu_{11}\tau - \mu_{12}^*). \tag{A2}$$

Here $\mu_{\rho\rho'} = \mu_{\rho\rho'}[\mathbf{k}(t)]$ are the matrix elements of the matrix $\hat{\mu}$ in Eq. (4), and $\mathbf{k}(t)$ is the function determined from Eq. (A1). The boundary condition to Eq. (A2) is

$$\tau(T) = \tau(0), \tag{A3}$$

where $T = 2\pi c m^*/(|e|H)$ is the period of the electron motion in the orbit Γ, and m^* is the electron cyclotron mass.

On calculating the functions $\mathbf{k}(t)$ and $\tau(t)$ the electron g factor for a closed orbit Γ is given by[5,8]

$$g = \frac{2m|e|H}{\pi m^* \hbar c}\int_0^T dt(\mu_{11}(\mathbf{k}) + \mathrm{Re}\{\tau(t)\mu_{12}(\mathbf{k})\}). \tag{A4}$$

Here $\mathbf{k}$ denotes the function $\mathbf{k}(t)$ determined from Eq. (A1). Since the combination $|e|Hdt/c$ is proportional to the infinitesimal element $|d\mathbf{k}|$ of the orbit Γ [see Eq. (A1)], the appearance of the factor $|e|H/c$ in Eq. (A4), of course, does not mean the proportionality of g to H. This factor is due only to the parametrization of the electron orbit with the use of the time t.

For the one-band and two-band models of the electron energy spectrum, the orbit Γ is an ellipse, and the function $\mathbf{k}(t)$ is easily found from Eq. (A1). In both these cases the matrix $\mu_{\rho\rho'}$ has the form[28]

$$\mu^{(0)}_{\rho\rho'}(\mathbf{k}) = \psi(\mathbf{k})c_{\rho\rho'}, \tag{A5}$$

where $\rho, \rho' = 1,2$, $\psi(\mathbf{k})$ is some real function of the wave vector (and of the electron energy), and $c_{11} = -c_{22}$ and $c_{12} = c_{21}^*$ are real and complex constants, respectively. With the use of Eq. (A5), equation (A2) with boundary condition (A3) is solved exactly,

$$\tau = (-c_{11} \pm \lambda)/c_{12},$$

where

$$\lambda = \sqrt{(c_{11})^2 + |c_{12}|^2}. \tag{A6}$$

Then it follows from Eq. (A4) that the g factor for these models is

$$g^{(0)} = \pm\frac{2m\lambda|e|H}{\pi m^*\hbar c}\int_0^T dt\,\psi(\mathbf{k}(t)). \tag{A7}$$

In the one-band case one has[28] $\psi = 1$, $c_{\rho\rho'} = \mu_{\rho\rho'}(\mathbf{k}_{\mathrm{ex}})$, where $\mathbf{k}_{\mathrm{ex}}$ is the point of the band extremum in the Brillouin zone. Using the formula $T = 2\pi c m^*/(|e|H)$, we obtain

$$g^{(0)} = \pm 4m\lambda/\hbar.$$

Note that in the one-band model this $g^{(0)}$ does not depend on the energy and thus coincides with the g factor at the band edge.

In the two-band case one has[28]

$$\psi(\mathbf{k}) = \frac{\hbar[\varepsilon + 0.5E_g - \hbar\mathbf{v}_a(0)\mathbf{k}]^{-1}}{2\varepsilon - \hbar[\mathbf{v}_0(0) - \mathbf{v}_a(0)]\mathbf{k}},$$

where ε is the electron energy, and the other notations are as in Eq. (3). The explicit expressions for $c_{\rho\rho'}$ are presented in Ref. 28. Integrating Eq. (A7), we now arrive at[28]

$$g^{(0)} = \pm 2m/m^*.$$

Note that in this case the combination $\delta \equiv gm^*/(4m)$ is equal to $\pm 1/2$, and thus the electron energy levels in the magnetic field are doubly degenerate.[29]

APPENDIX B: DEFORMATION OF THE ELECTRON ORBIT

An electron moving in the semiclassical orbit in a magnetic field has a constant energy ε. Suppose that the solution of Eq. (A1) for the dispersion relation $\varepsilon^{(0)}(\mathbf{k})$ is known, and that the electron orbit at the energy $\varepsilon^{(0)}$ is given by some function $\mathbf{k}^{(0)}[t,\varepsilon^{(0)}]$. We now find the new orbit

$$\mathbf{k}[t,\varepsilon]=\mathbf{k}^{(0)}[t,\varepsilon^{(0)}]+\Delta\mathbf{k}[t],$$

which corresponds to the new energy ε and to the modified dispersion relation (5). We obtain

$$\Delta\mathbf{k}(t)=\mathbf{F}_{\|}(\mathbf{k}^{(0)}(t))+[\mathbf{n}\times\mathbf{v}_{\perp}^{(0)}]\times\left\{F(t)-\frac{\int_0^T dt'(\mathbf{v}_{\perp}^{(0)}(t'))^2F(t')}{\int_0^T dt'(\mathbf{v}_{\perp}^{(0)}(t'))^2}\right\},$$

where $\mathbf{n}\equiv\mathbf{H}/H$, and $\mathbf{v}_{\perp}^{(0)}$ is the component of the velocity $\mathbf{v}^{(0)}\equiv(1/\hbar)(\partial\varepsilon^{(0)}(\mathbf{k})/\partial\mathbf{k})$ perpendicular to the magnetic field,

$$F(t)=\int_0^t dt'\frac{eH}{c\hbar}[\nabla_{\mathbf{k}_\perp}\mathbf{F}_{\|}(\mathbf{k})]\big|_{\mathbf{k}\to\mathbf{k}^{(0)}(t')},$$

and

$$\mathbf{F}_{\|}(\mathbf{k})=\frac{[\varepsilon-\varepsilon^{(0)}-\Delta\varepsilon(\mathbf{k})]\mathbf{v}_{\perp}^{(0)}(\mathbf{k})}{\hbar[\mathbf{v}_{\perp}^{(0)}(\mathbf{k})]^2}.$$

In calculating the change of the g factor, Δg, it is convenient to chose the constant $\varepsilon^{(0)}$ so that the periods of the electron motion (and hence the cyclotron masses) are the same for the orbits $\mathbf{k}[t,\varepsilon]$ and $\mathbf{k}^{(0)}[t,\varepsilon^{(0)}]$, i.e.,

$$\Delta T\equiv T-T^{(0)}=\int_0^T dt'(\nabla_{\mathbf{k}_\perp}\mathbf{F}_{\|}(\mathbf{k}))\big|_{\mathbf{k}\to\mathbf{k}^{(0)}(t')}=\frac{c\hbar}{eH}F(T)=0.$$

This condition is assumed to be fulfilled throughout this paper.

*E-mail: sharlai@ilt.kharkov.ua

[1] D. Shoenberg, *Magnetic Oscillations in Metals*, Cambridge University Press, Cambridge (1984).
[2] L. Onsager, Philos. Mag. **43**, 1006 (1952).
[3] A. M. Lifshits and A. M. Kosevich, Zh. Éksp. Teor. Fiz. **29**, 730 (1955) [Sov. Phys. JETP **2**, 636 (1956)].
[4] See, e.g., J. M. Ziman, *Principles of the Theory of Solids*, Cambridge University Press, Cambridge (1972); E. M. Lifshitz and L. P. Pitaevskii, *Statistical Physics*, Pergamon Press, Oxford (1986), Pt. 2.
[5] G. P. Mikitik and Yu. V. Sharlai, Zh. Éksp. Teor. Fiz. **114**, 1357 (1998) [Sov. Phys. JETP **87**, 747 (1998)].
[6] G. P. Mikitik and Yu. V. Sharlai, Phys. Rev. Lett. **82**, 2147 (1999).
[7] This orbit is determined by the equations[4] $\varepsilon(\mathbf{k})=\text{const}\,(=\varepsilon)$, $k_H=\text{const}$, where $\varepsilon(\mathbf{k})$ is the electron dispersion relation in the crystal in absence of magnetic field.
[8] G. P. Mikitik and Yu. V. Sharlai, Phys. Rev. B **65**, 184426 (2002).
[9] L. M. Roth, Phys. Rev. **145**, 434 (1966).
[10] A. M. De Graaf and A. W. Overhauser, Phys. Rev. **2**, 1437 (1970).
[11] R. A. Moore and C. F. Liu, Phys. Rev. B **8**, 599 (1973).
[12] M. Singh, J. Callaway, and C. S. Wang, Phys. Rev. **14**, 1214 (1978).
[13] F. Beuneu, J. Phys. F: Met. Phys. **10**, 2875 (1980).
[14] T. Jarlborg and A. J. Freeman, Phys. Rev. B **23**, 3577 (1981).
[15] A. H. MacDonald, J. M. Daams, S. H. Vosko, and D. D. Koelling, Phys. Rev. B **25**, 713 (1982).
[16] H. Ohlsen, P. Gustafsson, L. Nordborg, and S. P. Hornfeldt, Phys. Rev. **29**, 3022 (1984).
[17] H. Ohlsen and J. L. Calais, Phys. Rev. **35**, 7914 (1987).
[18] G. E. Grechnev, N. V. Savchenko, I. V. Svechkarev, A. V. Zhalko-Titarenko, M. J. G. Lee, and J. M. Perz, Fiz. Nizk. Temp. **13**, 1219 (1987) [Sov. J. Low Temp. Phys. **13**, 689 (1987)].
[19] N. V. Savchenko and G. E. Grechnev, Fiz. Nizk. Temp. **15**, 656 (1989) [Sov. J. Low Temp. Phys. **15**, 370 (1989)].
[20] G. E. Grechnev, N. V. Savchenko, I. V. Svechkarev, M. J. G. Lee, and J. M. Perz, Phys. Rev. **39**, 9865 (1989).
[21] O. Eriksson, H. Ohlsén, and J. L. Calais, Phys. Rev. B **40**, 5961 (1989).
[22] A. Hjelm and J. L. Calais, Phys. Rev. Lett. **67**, 2064 (1991).
[23] N. V. Savchenko, Fiz. Nizk. Temp. **17**, 77 (1991) [Sov. J. Low Temp. Phys. **17**, 41 (1991)].
[24] N. V. Savchenko, G. E. Grechnev, and I. V. Svechkarev, Fiz. Nizk. Temp. **17**, 859 (1991) [Sov. J. Low Temp. Phys. **17**, 449 (1991)].
[25] A. Hjelm and J. L. Calais, Phys. Rev. B **48**, 8592 (1993).
[26] V. I. Smelyansky, M. J. G. Lee, and J. M. Perz, J. Phys.: Condens. Matter **5**, 6061 (1993).
[27] A. M. De Graaf and A. W. Overhauser, Phys. Rev. B **180**, 701 (1969).
[28] G. P. Mikitik and Yu. V. Sharlai, Phys. Rev. B **67**, 115114 (2003).
[29] Here we mean the orbital part of the g factor. Note that its spin part is negligibly small when the two-band model is well applicable.
[30] M. H. Cohen and E. I. Blount, Philos. Mag. **5**, 115 (1960).
[31] Cohen and Blount[30] obtained their result under the conditions that the minimum of the first band and the maximum of the second band are at the same point of the Brillouin zone (i.e., they considered the case $\mathbf{v}_0(0)=\mathbf{v}_a(0)=0$) and that the electron orbit lies near the extremum of one of these bands and thus is small.
[32] E. R. Glaser, T. A. Kennedy, K. Doverspike, L. B. Rowland, D. K. Gaskill, J. A. Freitas, Jr., M. Asin Khan, D. T. Olson, J. N. Kuznia, and D. K. Wickenden, Phys. Rev. B **51**, 13326 (1995).
[33] G. Denninger, R. Beerhalter, D. Reiser, K. Maier, J. Scheider, T. Detchprohm, and K. Hiramatsu, Solid State Commun. **99**, 347 (1996).
[34] M. J. Yang, R. J. Wagner, B. V. Shanabrook, J. R. Waterman, and W. J. Moore, Phys. Rev. B **47**, 6807 (1993), and references therein.
[35] V. S. Edel'man, Usp. Fiz. Nauk **123**, 257 (1977) [Sov. Phys. Usp. **20**, 819 (1977)]; V. S. Édelm'man, Zh. Éksp. Teor. Fiz. **64**, 1734 (1973) [Sov. Phys. JETP **37**, 875 (1973)].
[36] E. I. Blount, Phys. Rev. **126**, 1636 (1962).
[37] L. M. Roth, J. Phys. Chem. Solids **23**, 433 (1962).
[38] H. L. Skriver, *The LMTO Method*, Springer-Verlag, Berlin (1984).
[39] J. L. Bir and G. E. Pikus, *Symmetry and Strain-Induced Effects in Semiconductors*, Wiley, New York (1974).
[40] V. G. Golubev, V. I. Ivanov-Omskii, I. G. Minervin, A. V. Osutin, and D. G. Polyakov, Zh. Éksp. Teor. Fiz. **88**, 2052 (1985) [Sov. Phys. JETP **61**, 1214 (1985)].
[41] M. Braun and U. Rössler, J. Phys. C: Solid State Phys. **18**, 3365 (1985).
[42] H. Mayer and U. Rössler, Phys. Rev. B **44**, 9048 (1991).
[43] See, e.g., S. A. Wolf *et al.*, Science **294**, 1488 (2001).
[44] J. W. McClure, J. Low Temp. Phys. **25**, 527 (1976).
[45] In the case of bismuth, the subscripts "0" and "a" are frequently denoted by "c" and "v," respectively.
[46] S. Sh. Akhmedov, R. Herrmann, K. N. Kashirin, A. Krapf, V. Kraak, Ya. G. Ponomarev, and M. V. Sudakova, Zh. Éksp. Teor. Fiz. **97**, 663 (1990) [Sov. Phys. JETP **70**, 370 (1990)].
[47] G. P. Mikitik and Yu. V. Sharlai, Fiz. Nizk. Temp. **26**, 54 (2000) [Low Temp. Phys. **26**, 39 (2000)].

This article was published in English in the original Russian journal. Reproduced here with stylistic changes by AIP.

Photoinduced lowering of the valence of vanadium ions in the garnet $NaCa_2Mn_2V_3O_{12}$

S. L. Gnatchenko, V. V. Eremenko, I. S. Kachur, V. G. Piryatinskaya, V. V. Slavin,* and V. V. Shapiro

B. I. Verkin Institute for Low Temperature Physics and Engineering, Ukrainian National Academy of Sciences, pr. Lenina 47, Kharkov 61103, Ukraine

M. B. Kosmyna, B. P. Nazarenko, and V. M. Puzikov

NTK "Institute of Single Crystals," Ukrainian National Academy of Sciences, pr. Lenina 60, Kharkov 61001, Ukraine

(Submitted April 26, 2004)
Fiz. Nizk. Temp. **30**, 1302–1306 (December 2004)

Measurements of the spectral distribution of the light absorption coefficient in the garnet $NaCa_2Mn_2V_3O_{12}$ are performed in a wide range of wavelengths. The influence of unpolarized illumination of a crystal on the light absorption spectrum is investigated. A substantial long-lived photoinduced effect is observed at low temperatures. This effect is manifested as a change in the spectral distribution of the light absorption coefficient and reflects a lowering of the valence of the vanadium ions under the influence of photoillumination. [DOI: 10.1063/1.1820039]

1. INTRODUCTION

Optical excitation is one of the most effective methods for generating metastable states, which are found to be long-lived in many cases. Many micro- and macroscopic properties of compounds change as a result of a photoinduced transition into metastable states. For example, in certain high-temperature superconductors photoexcitation changes the spectral characteristics of these compounds,[1,2] and at the same time stimulated their conducting properties—the superconducting transition temperature, the normal-phase conductivity, and the critical superconductivity current all increase.[3,4] At low temperatures these effects are long-lived—the relaxation times are of the order of days and possibly months. However, above 120–150 K the relaxation times decrease sharply (to minutes, seconds, or less). In high-temperature superconductors the oxygen subsystem plays a decisive role in the formation of long relaxation times.

Quite long-lived photoinduced effects have also been observed in many garnets.[5–13] As in the preceding case, these effects are due to charge transfer as a result of optical excitation. There is good reason to believe[13] that just as in high-temperature superconductors the long relaxation times in these garnets are also due to the presence of an oxygen subsystem.

Some transition-metal ions in the crystal lattice of most garnets where a photoinduced effect has been observed could be in a valence state different from the ground state for this compound (this is probably due to the presence of structural nonuniformities, which inevitably appear when the crystals are grown). Moreover, in many cases, external perturbations can change the valence of transition-metal ions.[11–14]

The ground-state configuration of the experimental garnet $NaCa_2Mn_2V_3O_{12}$ contains ions of divalent manganese Mn^{2+} and pentavalent vanadium V^{5+} ions. At the same time EPR measurements have shown that V^{4+} ions are present in the compound $NaCa_2Mg_2V_3O_{12}$ whose stoichiometric composition is close to that of $NaCa_2Mn_2V_3O_{12}$; the V^{4+} ions are present in the lattice together with V^{5+} ions.[15] It is very likely that V^{4+} ions are also present in the initial structure of the garnet $NaCa_2Mn_2V_3O_{12}$. Moreover, on the same basis, this could also be true for Mn^{3+} ions.

The most informative experimental method for determining the valence of ions is spectroscopy, specifically, optical spectroscopy. Indeed, the energy spectrum reflects quite clearly the individual features of any particular ion. If an ion changes valence, acquiring an extra electron or, conversely, loses an electron, then this necessarily influences the energy spectrum of the ion.

There is now full justification for believing that photoinduced effects in garnets based on manganese ions are due to a change in the valence of these ions under the influence of photoillumination.[11–13] Nonetheless, manganese garnets can also contain other optically active ions (for example, ions of different transition metals) that can also change valence under photoillumination, so there is no guarantee that all photoinduced changes in spectra are due to a change in the valence of solely manganese ions.

In addition, the contributions of Mn^{2+} and Mn^{3+} in the spectral distribution of photoinduced absorption cannot always be separated simply and uniquely. This is because a Mn^{2+} ion has a *half-filled* $3d$ shell (five electrons). The degeneracy of the $3d^5$ state is high because the maximum possible values of the total orbital L and spin S angular momenta are large. As a result of the interaction of the $3d$ electrons the energy structure of Mn^{2+} is found to be very developed and most electronic transitions occur into the near-IR, visible, and UV regions. The electronic $3d$ shell of the Mn^{3+} ion is nearly half-filled ($n=4$). The energy structure of the ion is also well developed. In addition, Mn^{3+} can undergo a spin-allowed electronic transition $^3E(^5D) \rightarrow {}^5T_2(^5D)$. In the absorption spectra of garnets this transition corresponds to a very wide and intense band near

19000 cm^{-1}, overlapping a large part of the spin-forbidden bands of Mn^{3+} and Mn^{2+} ions. It should also be kept in mind that charge transfer, which in these systems accompanies at least some electronic transitions, causes substantial broadening of the absorption bands of electromagnetic waves and increases the band intensities. All this complicates the interpretation of the bands associated with electronic transitions in manganese ions and makes it difficult to attribute the bands unequivocally to Mn^{2+} or Mn^{3+} ions.

The situation for transition-metal ions is different. For these ions the number of electrons in an unfilled $3d$ shell (or, conversely, with an almost filled shell) is small. In particular, this is true for the vanadium ion. The $3d$ shell of a vanadium ion in the V^{5+} state is empty and the d-d transitions are completely absent. In the V^{4+} state there is only one $3d$ electron; the spectrum of such an ion is not very developed—it lies in the radio, IR, and visible ranges and is due to which occur from a *single* crystal field split term ^2D. Consequently, if transitions of vanadium from the V^{5+} into the V^{4+} state occur as a result of photoexcitation, then such transitions should be accompanied simply by the appearance of a new absorption band (or several bands) which does not exist in the initial spectrum.[14] In other words, the interpretation of the changes in the absorption spectrum in this case is much simpler and, most importantly, unequivocal. For example, in Ref. 14 EPR and optical spectroscopy were used to observe the change in valence of vanadium ions in a $NaCa_2Mg_2V_3O_{12}$ single crystal, using thermal quenching (heating of the sample followed by rapid cooling) to transfer the sample into a metastable state.

In the present paper the results of the observation of valence changes of a vanadium ion in the garnet $NaCa_2Mn_2V_3O_{12}$ under the action of optical excitation are presented. Optical spectroscopy is used as the instrument of observation. At sufficiently low measurement temperature (30 K) the photoinduced changes in the absorption spectra are large, and the relaxation times are long. At the same time this temperature is somewhat higher than the Néel temperature of the garnet $NaCa_2Mn_2V_3O_{12}$ ($T_N = 25$ K (Ref. 16)), making it possible to neglect in the analysis any features due to antiferromagnetic ordering.

2. EXPERIMENT

$NaCa_2Mn_2V_3O_{12}$ single crystals were grown by spontaneous crystallization.[17] Samples were cut in the form of plane-parallel plates perpendicular to the [100] crystallographic axis. A quartz halogen lamp, powered by a highly stable current source, served as a light source for the measurements. The light from the lamp was passed through a MDR-23 diffraction monochromator, which was used to scan the spectrum, and directed onto a sample located in a cryostat. In the sample the light propagated along the [100] axis. The monochromatic light flux density on the sample was low, so that the photoinduced effect from the probe source was below the threshold of measurement accuracy. Photomultipliers were used to record the light intensity at the exit from the sample.

Figure 1 shows the spectral distribution of the light absorption coefficient $K(\nu)$ in a sample of a $NaCa_2Mn_2V_3O_{12}$ single crystal before the sample was illuminated with light.

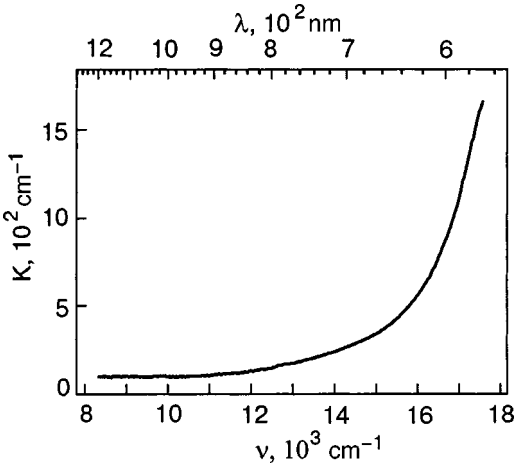

FIG. 1. Photoabsorption spectrum of $NaCa_2Mn_2V_3O_{12}$ in the absence of optical excitation. $d = 50$ μm; $T = 30$ K.

Absorption is observed in the entire experimental frequency range, but substantial growth of $K(\nu)$ starts at 14000 cm^{-1}.

Unpolarized emission from a helium–neon laser was used as the source for optical excitation. The radiation wavelength was 633 nm and the radiation density was 0.13 W/cm^2. The laser beam was directed at a small angle to the [100] axis.

Optical excitation results in a photoinduced increase of the light absorption coefficient of the crystal in the entire experimental frequency range. Figure 2 shows the kinetics of the photoinduced changes ΔK of the light absorption coefficient of the crystal measured at two wavelengths. The initial sharp growth of K corresponds to the moment when the laser illumination is switched on, and the dropoff near $t = 15$ min corresponds to the time when the laser illumination is switched off. The photoinduced effect essentially saturates in 15 min of illumination, after which the spectral distribution of the absorption coefficient of the illuminated sample remains virtually constant.

On this basis, with the laser switched on, the light absorption spectrum was recorded 15 min after the photoillumination. The difference between the two measurements of the absorption spectrum of the sample performed after and before photoillumination gives the spectral distribution of the

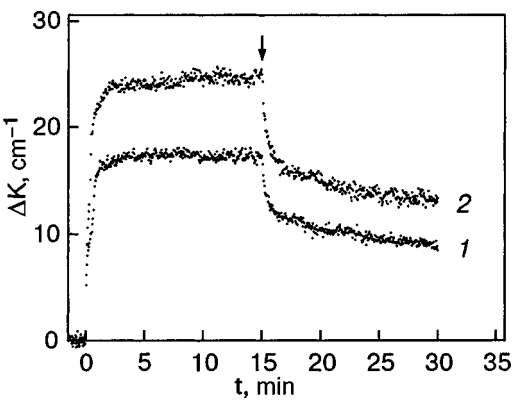

FIG. 2. Time dependence of the photoinduced light absorption in $NaCa_2Mn_2V_3O_{12}$. $d = 50$ μm, $T = 30$ K; $\lambda = 750$ μm (1), $\lambda = 575$ μm (2). The arrow marks the moment when photoillumination is switched off.

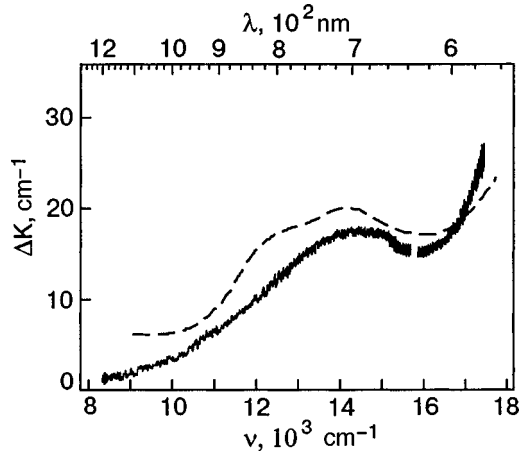

FIG. 3. Spectral distribution of photoinduced light absorption in $NaCa_2Mn_2V_3O_{12}$. $d=50$ μm, $T=30$ K. For comparison the broken line shows the light absorption spectrum of a $NaCa_2Mg_2V_3O_{12}$ crystal with an optically active V^{4+} ion[14] (in arbitrary units along the ordinate).

photoinduced effect (Fig. 3). The gap in the spectral distribution of the photoinduced absorption in the sample near the optical excitation wavelength $\lambda=633$ nm is due to suppression of the scattered laser light.

Aside from the general growth of the photoinduced absorption in the entire experimental frequency range, the optical excitation gives rise to a new absorption band with a maximum near $\nu_v=14500$ cm^{-1} and half-width about 4000 cm^{-1}. This new band can be clearly seen against the background due to the long-wavelength tail of the stronger absorption.

3. DISCUSSION

As noted in the introduction, the presence of an oxygen subsystem in the experimental garnet plays a special role in the formation of holes with long recombination times.[13] In the present case there are two basic possibilities for the formation of holes in the oxygen subsystem (O^{2-}) which are capable of producing a long-lived photoinduced effect in $NaCa_2Mn_2V_3O_{12}$. We shall briefly examine these possibilities.

1. A Mn^{3+} ion absorbs a laser photon. The excitation energy is expended on transferring a hole from the Mn^{3+} ion into the subsystem of oxygen ions (O^{2-}) with a completely filled p shell. As a result, the Mn^{3+} ion transforms into Mn^{2+} and a hole (O^- ion) is formed in the oxygen subsystem. The long relaxation times in $NaCa_2Mn_2V_3O_{12}$ (Fig. 2) attest to the fact that we are dealing with very heavy holes, existing in the form of compact, tightly bound polarons. A polaron is a diatomic molecule $O^- - O^{2-}$ whose constituents O^{2-} and O^- possess, respectively, the configurations $1s^22s^22p^6$ (the configuration of neon) and $1s^22s^22p^5$ (the configuration of oxygen with a p hole). This scenario is described in detail in Ref. 13. Of course, the efficiency of this mechanism is determined by the number of Mn^{3+} ions in the initial structure of the garnet $NaCa_2Mn_2V_3O_{12}$.

2. A Mn^{2+} ion absorbs a laser photon. The Mn^{2+} ion passes from the initial fully symmetric ^6S state into a lower-symmetry state with an orbital extending toward one of the oxygen ions. The potential of the oxygen subsystem becomes deformed because the electron on the photoexcited Mn^{2+} ion is repelled by the electrons on the oxygen ion. This creates a favorable situation for a hole to leave the V^{5+} ion and enter the oxygen subsystem. In other words, a vanadium ion, which has an oxygen neighbor in common with the photoexcited Mn^{2+} ion, is transferred into the V^{4+} state.

Therefore both scenarios produce identical changes in the oxygen subsystem. But they differ by the method by which a hole is generated: in the first case the hole arrives from a Mn^{3+} ion and in the second case from V^{5+}.

In Fig. 3, which shows the spectral distribution of the photoinduced effect in $NaCa_2Mn_2V_3O_{12}$, the most noticeable feature is the appearance of a new band ν_v. It is known[18] that the frequency of the lowest energy band in the absorption spectrum of a Mn^{2+} ion in the octahedral environment formed by O^{2-} ions (close to the O^{2-} complex in $NaCa_2Mn_2V_3O_{12}$) is of the order of 16000 cm^{-1}. In the case of a Mn^{3+} ion the lowest band (spin-allowed transition) in garnets lies near 19000 cm^{-1}.[19] Therefore the new band cannot be identified with electronic transitions in the Mn^{2+} and Mn^{3+} ions. On the other hand, the contour of the photoinduced band ν_v is nearly identical to that of the band in the absorption spectrum of the crystal $NaCa_2Mg_2V_3O_{12}$ (Fig. 3).[14] In Ref. 14 the quenching method made it possible to lower the initial valence of the vanadium ion (i.e. V^{5+} was reduced to V^{4+}). Thus the appearance of the new band ν_v in the spectrum of the photoilluminated garnet $NaCa_2Mn_2V_3O_{12}$ can be attributed, with a high degree of confidence, to the appearance of *additional* ions V^{4+} in the crystal lattice, which occurs together with the photoinduced effect as a result of the transfer of electrons from the oxygen subsystem O^{2-} to the V^{5+} ions (mechanism 2).

The result obtained is direct experimental proof of the lowering of the valence of a vanadium ion in the garnet $NaCa_2Mn_2V_3O_{12}$ under photoillumination. At the same time not all photoinduced changes observed in the absorption spectrum of garnet in the experimental wavelength range (Fig. 3) are due exclusively to the transitions $V^{5+}\rightarrow V^{4+}$ in a vanadium ion. It is very likely that manganese ions also contribute to the observed photochromic effect in the high-frequency region of the spectrum.

We are deeply grateful to A. M. Ratner for a fruitful discussion of the results.

*E-Mail: slavin@ilt.kharkov.ua

[1] V. I. Kudinov, I. L. Chaplygin, A. I. Kirilyuk, N. M. Kreines, R. Laiho, E. Lahderanta, and C. Ayache, Phys. Rev. B **47**, 9017 (1993).
[2] I. Fugol, V. Samovarov, A. Ratner, V. Zhuravlev, G. Saemann-Ischenko, M. Lippert, and B. Holzapfel, Physica C **216**, 391 (1993).
[3] V. V. Eremenko, I. S. Kachur, V. G. Piryatinskaya, A. M. Ratner, and V. V. Shapiro, Physica C **262**, 54 (1996).
[4] V. M. Dmitriev, V. V. Eremenko, I. S. Kachur, V. G. Piryatinskaya, O. R. Prikhod'ko, A. M. Ratner, E. V. Khristenko, and V. V. Shapiro, Fiz. Nizk. Temp. **21**, 219 (1995) [Low Temp. Phys. **25**, 168 (1995)].
[5] R. W. Teale and D. W. Temple, Phys. Rev. Lett. **19**, 904 (1967).
[6] R. F. Pearson, A. D. Annis, and P. Kompfner, Phys. Rev. Lett. **21**, 1805 (1968).
[7] K. Hisatake, J. Matsubara, K. Maeda, H. Yasuoka, H. Mazaki, and K. Vematsu, J. Magn. Magn. Mater. **140–144**, 2127 (1995).
[8] J. F. Dillon, E. M. Gyorgy, and J. P. Remeika, Phys. Rev. Lett. **23**, 643 (1969).

[9] H. Van der Heide, Solid State Commun. **6**, 347 (1968).
[10] E. M. Gyorgy, J. F. Dillon, and J. P. Remeika, J. Appl. Phys. **42**, 1454 (1971).
[11] V. V. Eremenko, S. L. Gnatchenko, I. S. Kachur, V. G. Piryatinskaya, A. M. Ratner, and V. V. Shapiro, Phys. Rev. B **61**, 10670 (2000).
[12] V. V. Eremenko, S. L. Gnatchenko, I. S. Kachur, V. G. Piryatinskaya, A. M. Ratner, V. V. Shapiro, M. Fally, and R. A. Rupp, Fiz. Nizk. Temp. **27**, 30 (2001) [Low Temp. Phys. **27**, 22 (2001)].
[13] V. V. Eremenko, S. L. Gnatchenko, I. S. Kachur. V. G. Piryatinskaya, A. M. Ratner, M. B. Kosmyna, B. P. Nazarenko, and V. M. Puzikov, J. Phys.: Condens. Matter **15**, 4025 (2003).
[14] G. Oversluizen and R. Metselaar, J. Phys. C **15**, 4869 (1982).
[15] V. Havlicek, P. Novak, and M. Vichr, Phys. Status Solidi B **44**, K21 (1971).
[16] K. P. Belov and V. I. Sokolov, Usp. Fiz. Nauk **121**, 285 (1977) [Sov. Phys. Usp. **20**, 149 (1977)].
[17] V. V. Eremenko, S. L. Gnatchenko, I. S. Kachur, V. G. Piryatinskaya, A. M. Ratner, V. V. Shapiro, M. B. Kosmyna, B. P. Nazarenko, and V. M. Puzikov, Ukr. Phys. J. **49**, 432 (2004).
[18] D. R. Huffman, R. L. Wild, and M. Shinmei, J. Chem. Phys. **50**, 4092 (1969).
[19] S. Kuck, S. Hartung, S. Hurling, K. Petermann, and G. Huber, Phys. Rev. B **57**, 2203 (1998).

Translated by M. E. Alferieff

PHYSICAL PROPERTIES OF CRYOCRYSTALS

Influence of an admixture of H_2 molecules on the structure and parameters of a Ne lattice

N. N. Gal'tsov,* A. I. Prokhvatilov, and M. A. Strzhemechnyĭ

B. I. Verkin Institute for Low Temperature Physics and Engineering, Ukrainian National Academy of Sciences, pr. Lenina 47, Kharkov 61103, Ukraine
(Submitted February 11, 2004; revised June 17, 2004)
Fiz. Nizk. Temp. **30**, 1307–1314 (December 2004)

X-Ray investigations of solid solutions formed by condensation of mixtures of normal hydrogen and neon gases are performed for concentrations ranging from 2 to 60 mol.% nH_2 and temperatures ranging from 5 K to the melting temperature of the sample. The structure of the vacuum condensates Ne-nH_2 immediately after the samples are obtained is investigated. The boundary of single-phase solutions of hydrogen in neon is established to be 2 mol.%. At high H_2 concentrations a hexagonal hcp_2 phase forms in addition to a cubic fcc phase. The lattice volumes of these phases are somewhat larger but close to the volume of a pure-neon cell. The hexagonal hcp_2 phase vanishes when the condensates are heated to a temperature of the order of the melting temperature of neon. This metastable hexagonal phase in the neon-rich mixtures studied is probably identical in nature to the previously observed hcp_2 phase in hydrogen-rich solid mixtures. Both phases have one symmetry and the same cell volume. Information on the phase composition of the condensates is obtained from data on the concentration and temperature variations of the x-ray reflection intensities. It is shown that as the concentration of hydrogen molecules in the initial gas mixtures increases, the amount of the fcc phase in the condensates decreases almost linearly and the amount of the hcp_2 phase increases. A combined analysis of the data obtained in the present work and previous measurements established the phase boundaries in the entire concentration range of the condensates. Evidently, because the molecular parameters of the components are close the Ne-nH_2 mixtures do not form gel-like states, which are characteristic for quench-condensed Kr–H_2 condensates. © *2004 American Institute of Physics.* [DOI: 10.1063/1.1820040]

1. INTRODUCTION

The problem of controllable technologies for preparing solid mixtures capable of functioning as accumulators of energy-dense states is topical from the standpoint of applications and general physics. A method for producing solid mixtures of helium with various particles (atoms, small molecules and radicals, and so on) was once proposed.[1] This was done using a jet of the corresponding impurity particles, which was blown directly into the container holding the superfluid helium. This yielded self-maintaining gel-like samples which held their shapes for very long times, if their temperature remained sufficiently low. As temperature increased, these samples decomposed explosively and a corresponding impurity fraction was formed;[2] the critical temperature depended strongly on the type of impurity. A series of experiments enabled the authors of this method to advance the hypothesis that the impurity particles (Im) form van der Waals complexes of the type $ImHe_{12}$ (as a result of the stronger impurity-helium attraction), which in turn can form an amorphous or even crystalline body as a result of attractive intercomplex forces. Subsequent structural and optical investigations (see the review in Ref. 3) showed that morphologically the states under discussion are gels where the impurity particles form an irregular hollow framework and the helium atoms fill nanovoids. Since diffusion is strongly suppressed at sufficiently low temperatures, helium interlayers prevent the impurity fractions from forming macroscopic particles. As temperature increases, all particles start to diffuse, the binding of impurity nanoparticles with one another causes additional heat to be released, and the process of crystallization of the impurity fraction proceeds like an avalanche. Not so long ago it was believed that an absolutely necessary experimental condition for obtaining impurity-helium states is high thermal conductivity of superfluid helium, as a result of which the high energy of the impurity particles in the jet blown into the container dissipates rapidly and effectively. Subsequently, however, a procedure for embedding impurities directly in solid helium was proposed and realized (see Ref. 4). But, a no less unique property of solid helium is used in this case—its superhigh plasticity.

Since hydrogen is not a superfluid, the no less topical problem of producing similar states based on hydrogen must be solved on the basis of different considerations. We have proposed and realized a method for quench-condensing gaseous mixtures of normal hydrogen with krypton and argon atoms on a cold substrate. This method has yielded samples with a large fraction being similar to helium-impurity states.[5] This showed that we were dealing with hydrogen-impurity

gels. More generally, it would be desirable to extend this method (possibly, modifying it appropriately) to other nonmetallic, specifically, noble, elements.

Among binary mixtures of cryocrystals the system $Ne-H_2$ possesses the unique feature that the molecular parameters of the components are extremely close.[6,7] It is now known that in many respects $Ne-H_2$ alloys close to equilibrium behave anomalously. For example, the presence of a structural anomaly[8] in weak solutions of neon in solid parahydrogen led to the conclusion that van der Waals complexes $Ne(H_2)_n$, which are "built into" and from the dynamics standpoint are quasi-independent of the hydrogen lattice, can exist. The specific anomaly in the heat capacity[9] of such solutions can also be explained on the basis of the complex-formation hypothesis. In addition, x-ray studies of solutions of neon with parahydrogen and normal hydrogen have revealed an unusual phase which can be regarded as a phase formed on the basis of neon but with a cubic fcc instead of a hexagonal hcp structure.[10] The main motivation for the present work was to investigate this new hexagonal phase and the formation of gel-like states in greater detail and from the standpoint of possible partial decomposition of the semiclassical system $Ne-H_2$.

Another question proposed for the present work was the maximum mutual solubility of the components[1)] for our sample-preparation procedure. The point is that even though the molecular parameters of the experimental components are extremely close (according to different sources, the Lennard-Jones parameters are $\sigma=2.928-2.96$ Å and $\varepsilon=35.2-36.7$ K for H_2 and $\sigma=2.749-2.788$ Å and $\varepsilon=35.6-36.7$ K for Ne) the degrees to which the components retain their quantum nature differ substantially primarily because of the large difference in masses. Consequently, the difference of the molar volumes of the crystals of the pure components is also large. Thus, the cell volume is 13.31 cm^3/mole is for hcp neon and 22.83 cm^3/mole for the hcp lattice of normal hydrogen,[7] which predisposes this nominally almost isotopic system to decomposition, just as in the case of truly isotopic hydrogen–deuterium mixtures.[11] According to Refs. 12 and 13, separation occurs even in liquid solutions. As a result, the mutual solubility of the components is very limited in the liquid state and especially in the solid state. According to x-ray investigations, when $Ne-H_2$ mixtures crystallize from the liquid phase[14] the maximum solubility of neon in normal solid hydrogen is no more than 0.25%. (Here and below we refer to molar fractions.) This result has been confirmed by more accurate measurements,[15] where the same quantity was determined to be 0.2%. An analysis of the thermal conductivity of solutions of neon in hydrogen gave the same value.[16] As far as the maximum solubility of normal hydrogen in polycrystalline neon is concerned, x-ray diffraction investigations have shown that it is at least 0.5% for crystallization of liquid mixtures.[14]

When solid solutions are obtained under extremely nonequilibrium conditions, for example, with high degrees of supercooling, the regions of single-phase solutions based on the initial components can be much wider than the nominal limits (determined according to the composition in the condensing gas), depending on the maximum solubilities at the solidus. There are two reasons for this. In the first place, in this case the concentration boundary is determined not by the equilibrium line but by the lability line. In the second place, the true concentration in a uniform phase can differ appreciably from the nominal concentration and, in addition, it can strongly depend on the condensation procedure. For example, we have established in our previous work that when hydrogen is dissolved in neon the fcc structure of neon remains up to 5% H_2. For a different method for obtaining samples[17,18] the solubility of hydrogen can reach 10%, and the application of hydrostatic pressure decreases it appreciably in this system.

In the present work, using the results of previous investigations[8,10] and the latest data on solutions of hydrogen in argon and krypton,[5] experiments were performed on samples obtained under extremely nonequilibrium conditions of crystallization. How the annealing temperature and hydrogen concentration influence the structural characteristics of the $Ne-H_2$ solid solutions is also studied.

2. EXPERIMENTAL PROCEDURE

The samples were obtained by condensing small portions of gaseous mixtures of normal room-temperature hydrogen and neon onto a flat copper substrate at $T=5$ K. The condensation conditions were adjusted so that the substrate would not be heated by more than 1–2 K when the mixture crystallizes. The initial components were at least 99.99% pure. The hydrogen concentration in the mixtures was set to within 5% using the P-V method. The nominal hydrogen concentration x in the gas mixtures was varied from 2 to 60%. The polycrystalline samples obtained were estimated to be 0.1 mm thick.

The powder x-ray diffraction method with a DRON-3M diffractometer and a helium cryostat for the temperature range 5–300 K was used to perform the structural studies. The temperature of the samples was measured and stabilized to within ± 0.05 K. Diffraction patterns were obtained not only from freshly prepared samples but also while the samples were heated (for two or three temperatures right up to the corresponding melting temperatures).

3. RESULTS AND DISCUSSION

For the extremely stringent conditions which we used to condense Ne-$n$$H_2$ mixtures and for hydrogen impurity concentrations varying over wide limits it is impossible to obtain completely amorphous samples, though partial structural disordering is observed, especially near the equimolar composition. This is clearly seen in Fig. 1, where typical x-ray diffraction patterns from a sample obtained by condensing a gas mixture with $x=50\%$ Ne are presented as an example. It is evident that the coherent reflections from condensates freshly prepared at 5 K are much weaker and much wider than the reflections from solid solutions annealed with temperature increasing. A substantial temperature variation of the form and intensity of incoherent scattering is also observed. The initial samples have a clearly noticeable bell-shaped background scattering localized at angles $2\theta=32-38°$, covering the strongest reflection from the close-packed (111) planes of the fcc neon crystals. As temperature

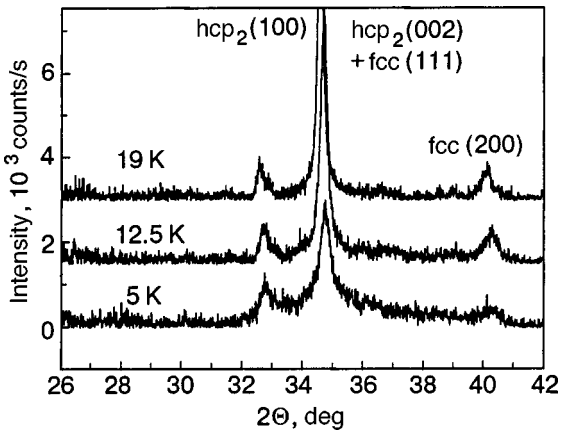

FIG. 1. X-Ray diffraction patterns from the solid mixtures Ne+50% nH$_2$ condensed at 5 K and then systematically annealed at higher temperatures. The diffraction patterns do not contain reflections from a phase based on the hydrogen lattice; only two systems of reflections (the indexing is indicated) from cubic and hexagonal phases with molar volumes close to that of solid neon can be seen. The diffraction patterns are shifted relative to one another along the vertical axis.

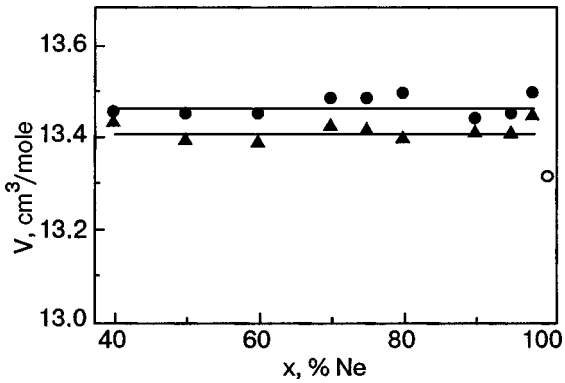

FIG. 2. Concentration dependences of the volumes of the fcc and hcp$_2$ phases of the solid mixtures Ne-nH$_2$, obtained by condensation from gas at 5 K: fcc (●), hcp (▲), molar volume of fcc phase of pure neon at 5 K (○).

increases above 10 K, this background vanishes and the intensity and localization of coherent scattering increase appreciably. This could indicate that the defect density and stresses in the crystal structure of the solutions decrease and that an amorphous phase, which is present in the samples and is responsible for the observed background halo, crystallizes, and the crystallites increase in size as a result. This temperature behavior is characteristic for all compositions of the experimental mixtures.

It is evident, including in Fig. 1, that the diffraction patterns contain a collection of reflections which are unusual for the cubic phase of pure neon. Analysis showed that the observed diffraction pattern corresponds to the presence of two phases in the sample—cubic fcc and hexagonal hcp phases. In addition, the molar volumes of both phases are close to the volume of the pure-neon lattice. Since the two indicated phases have close volumes, the reflections from the close-packed layers of both phases almost completely coincide with one another. We obtained the same result in Ref. 10, where this phase was first observed and correctly identified but not investigated. The hcp phase was also observed in Ref. 14 with crystallization of mixtures with hydrogen concentration above 0.5 mol.% from the liquid phase, but the appearance of this phase was attributed to the decomposition of a solid solution with separation of a hydrogen-based hexagonal phase. In the present work it was established that together with a cubic fcc neon phase, the reflections from this unusual hexagonal hcp$_2$ phase (the notation hcp$_2$ is introduced in order to distinguish this phase from the hydrogen-based hexagonal phase hcp$_1$) are observed for $x \leqslant 98\%$ Ne. Since these reflections from the hcp$_2$ phase are strongly shifted (by more than 5°) relative to the "hydrogen" triplet, they cannot correspond to diffraction from hydrogen-based hexagonal crystals. Summarizing this part of the our investigations, we underscore the fact that for all samples, right up to a mixture composition with 60 mol.% hydrogen, no reflections from a phase based on a hydrogen lattice are observed. We also note here that samples with $x = 98\%$ did not always give reproducible results in the sense that the hcp$_2$ phase was absent in some samples and traces of this phase were present in other samples. Consequently, this concentration is taken as a limit where the hcp$_2$ phase only just begins to appear, and it is also assumed that all of the hydrogen dissolves in the fcc neon phase.

The lattice parameters and volumes of both phases were determined in the entire experimental range of concentrations. It was found that within the statistical variance the molar volumes of the fcc and hcp$_2$ phases are essentially independent of the composition of the samples in the gas phase (Fig. 2). Nonetheless the nominal hydrogen content varies by a factor of 30. We note that the volumes of both phases are clearly greater than the characteristic value for pure crystalline neon (open circle in Fig. 2).[19] In addition, the volume of the hexagonal hcp$_2$ phase in the entire concentration range is systematically less (by 0.06 cm^3/mole) than the average volume of the cubic phase (Fig. 2). The neon-based hexagonal phase hcp$_2$ is characterized at $T=5$ K by the parameter ratio $c/a = 1.636 \pm 0.0005$, which agrees satisfactorily with the previously obtained value[10] and somewhat greater than the value 1.634 ± 0.0005 observed for pure normal hydrogen.[20] The ratio c/a remains constant (to within the variance), just as the volume, over the entire concentration range. The ratio c/a for the hcp$_2$ phase is also temperature-independent.[20]

The data showing that the lattice parameters and volumes of both phases are independent of the hydrogen concentration are very surprising (Fig. 2). This is especially strange because we did not observe a hydrogen-based phase, and therefore in the entire experimental concentration range almost all of the hydrogen can enter into the solid neon when the Ne-nH$_2$ mixtures condense. The phenomenon under discussion can be understood if it is assumed that the H$_2$ molecules in solid mixtures with neon do not possess the quantum properties which they possess in pure-hydrogen crystals. When hydrogen enters the neon lattice the quantum nature of the hydrogen molecules is easily suppressed. Then, substitution of hydrogen molecules for neon atoms at the sites of the unit cell should not greatly change the interaction energy, since the molecular parameters ε and σ for hydrogen molecules and neon atoms are close to one another, and there should be no observable lattice deformations over a wide concentration range. This prerequisite is confirmed in the

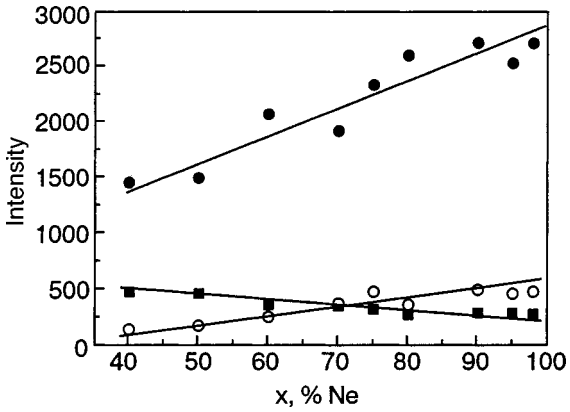

FIG. 3. Concentration dependences of the intensities of the (200) reflections from the fcc phase (○) and (100) reflections from the hcp_2 phase (■) and the sums of the intensities of the reflections from the cubic (111) and hexagonal (002) phases of the solid solutions Ne-nH$_2$, obtained immediately after condensation of gas mixtures on a substrate with temperature 5 K (●).

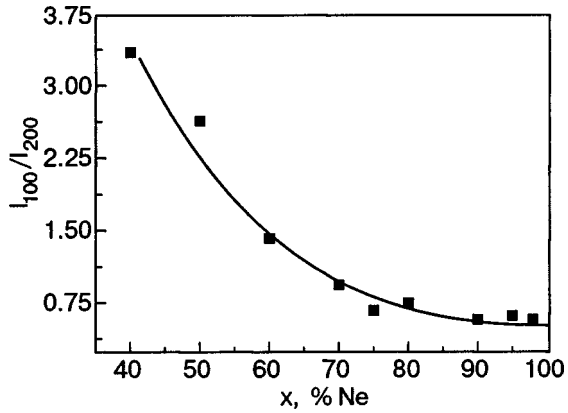

FIG. 4. Concentration dependence of the ratio of the intensities of the (100) and (200) reflections from the hexagonal hcp_2 and cubic fcc phases of the solid solutions Ne-nH$_2$ obtained by condensing gaseous mixtures on a substrate with temperature 5 K.

concentration dependences of the parameters and volumes which we obtained for the lattices of the fcc and hcp_2 phases of Ne-nH$_2$ solid solutions condensed from gas on a substrate at temperature 5 K (Fig. 2). The cubic and hexagonal neon phases have, to within the measurement error, almost the same lattice volumes, which remain virtually unchanged as a function of concentration over a wide concentration range.

On this basis the appearance of coexisting fcc and hcp_2 phases at a certain composition cannot serve as evidence for the ''standard'' separation of the solid solution. Both observable phases possess almost identical lattice volumes, while the volumes of the neon- and hydrogen-based solid solutions should be substantially different (by 70% or more). Therefore the observed cubic and hexagonal phases should be attributed to the crystalline modifications of neon-based solutions. It is well known that the difference of the energies of the fcc and hcp lattices is extremely small for crystals of inert elements. The high density of stacking faults in fcc inert-gas crystals attests to this.[19] Consequently, various factors, including impurities, can disrupt the stability of the cubic structure relatively easily.

As a supposition requiring further checking, we shall formulate the following scenario for the crystallization of neon-hydrogen mixtures. In all probability, the fcc lattice of neon cannot accept even a very small (less than 2%) amount of H_2 impurity without becoming unstable. In this respect the hcp lattice is found to be more ''suitable,'' admitting an admixture of hydrogen molecules as impurities in substantially larger numbers. As a result, two phases are formed when a gas mixture with a definite composition condenses. In one phase the hydrogen content is minimum (fcc) and virtually all of the impurity component is in the other structure (hcp_2). Actually, in this case a single factor will determine the ratio of the amounts of these two phases in the samples.

To analyze the ratio of the hexagonal and cubic phases of neon, curves of the total intensities of all observed reflections were constructed as a function of x (Fig. 3) for freshly prepared samples, and similar curves were constructed for the ratios of the total intensities of the reflections belonging unequivocally to different phases—(100) reflections for hcp and (200) reflections for fcc (Fig. 4). The intensities of the x-ray reflections from the condensates of the solid solutions Ne-nH$_2$ were analyzed assuming that the microstructural state of the samples (degree of dispersion, microdistortions, texture, and so on) was the same at all concentrations. This assumption is close to reality, since the method used to obtain the condensates and the x-ray diffraction measurements performed on them were identical for all compositions. This makes it possible to attribute the observed changes in the intensities primarily to a change in the phase composition of the samples. Figure 3 shows that as the nominal hydrogen content increases, the intensity of the (200) line of the fcc phase decreases and the intensity of the (100) line of the hcp phase increases; both dependences are nearly linear. As x decreases, the total intensity of the reflections, which are actually inseparable, from the close-packed (111) layers for the fcc and (002) layers for the hcp_2 lattices also decreases quite rapidly.

The dependences of the total intensity of the (200) line of the fcc phase on the nominal concentration were analyzed to obtain quantitative data on the phase composition of the samples. Figure 5 shows the ratio of the total intensities of the (200) line of the fcc phase as a function of x, referenced to the intensity of this line at the critical concentration $x = 98\%$, for which we believe (see above) the entire sample to be still in the fcc phase. Assuming the microstructure of the samples to be the same for all compositions, it can be

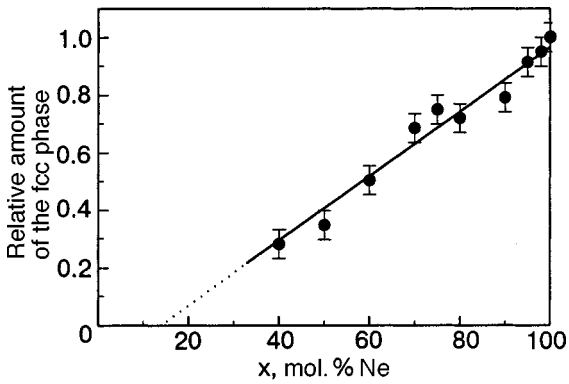

FIG. 5. Concentration dependence of the content of the cubic fcc phase in the vacuum condensates Ne-nH$_2$ at $T = 5$ K.

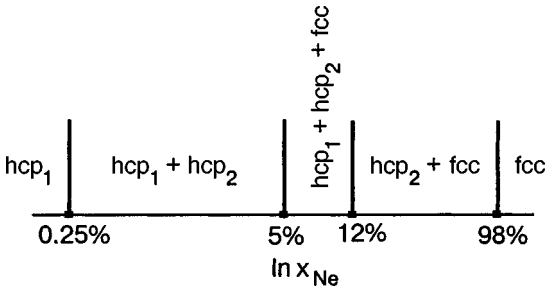

FIG. 6. Diagram showing the change in phase composition in the binary system Ne-nH$_2$ in the entire concentration range at 5 K.

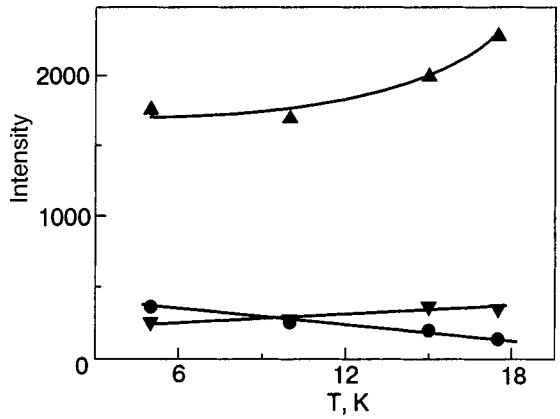

FIG. 7. Temperature dependences of the intensities of x-ray reflections from the hexagonal hcp$_2$ and cubic fcc phases of the binary mixture Ne+60 mol.% nH$_2$: (100) hcp (●), (111) and (002) hcp (▲), and (200) fcc (▼).

supposed that this ratio characterizes the specific content of the fcc phase. It is evident that as x decreases, the content of the fcc fraction decreases and, according to the linear extrapolation performed, drops to zero with approximately 17% neon in the mixtures.

The results obtained, together with the data in Refs. 8 and 10, make it possible to construct the following unified qualitative picture of the phase composition and boundaries of the phase regions of Ne-nH$_2$ condensates obtained in the entire concentration interval at 5 K. The solid solutions based on pure components exist in relatively narrow ranges (Fig. 6): the hcp$_1$ phase of hydrogen for $x<0.25$ mol.% and the fcc phase of neon-based solutions for $x(n\mathrm{H}_2)\leqslant(2-5)$ mol.%. Multiphase samples form in the intermediate concentration range. On the Ne side the condensates consist of two phases in a wide concentration range from 2 to 87 mol.% nH$_2$—cubic fcc and hexagonal hcp$_2$. Then a range of triple-phase states is observed 5–13 mol.% Ne, where a hydrogen-based hexagonal hcp$_1$ phase is added to the phases with the volume of the fcc and hcp$_2$ neon lattices. In the interval 0.5–5 mol.% Ne only two hexagonal phases hcp$_1$ and hcp$_2$ with volumes close to the volumes of the lattices of pure hydrogen and neon were usually observed. The result of extrapolating to low neon concentrations agrees well, to within the error in determining the reflection intensities, with the proposed diagram (Fig. 6) of the phase composition of the condensates. The amount of the fcc phase in the triple-phase region is indeed very small, and this phase completely vanishes at the boundary with the region of coexistence of the hcp$_1$ and hcp$_2$ phases.

The presence of a three-phase region in a two-component system attests to the fact that one phase is a nonequilibrium state. Previous investigations[8,10] and the investigations performed in the present work have established that even though it is long-lived at low temperatures the hcp$_2$ phase is a nonequilibrium state. At high temperatures, where the accelerating diffusion of the molecules leads to an equilibrium state, the hcp$_2$ phase becomes unstable and irreversibly vanishes, decomposing into the stable hcp$_1$ hydrogen and fcc neon phases. The present investigations of the influence of temperature on the phase composition of Ne-nH$_2$ condensates confirm this conclusion. Heating samples with a high neon content above the hydrogen melting temperature ordinarily results first in a weak and then, near the melting point of neon, a strong change in the intensity of reflections from the hcp$_2$ and fcc phases, attesting to an increase in the amount of the latter (Fig. 7). It was noted that as the hydrogen concentration in the condensates increases, the temperature of intense decomposition of the hcp$_2$ phase decreases. As follows from Ref. 8, in the limit of hydrogen-rich solutions this phase decomposes at temperatures near the melting temperature of pure H$_2$.

4. CONCLUSIONS

Quench condensation of Ne-nH$_2$ mixtures in a wide concentration range from 0.5 to 98% does not yield amorphous or extremely fine-crystalline states, as observed in mixtures with heavier inert gases. The system studied here follows a different path, specifically, the hexagonal hcp$_2$ phase of neon is present in vacuum condensates together with phases based on the hcp$_1$ and fcc lattices of the initial components. Both phases—hcp$_2$ and fcc—have nearly same unit-cell volume, which is close to the lattice volume of pure neon and remains constant over a wide concentration range. The hcp$_2$ phase is an excellent hydrogen accumulator and, in the limit, can contain up to 83 mol.% H$_2$. As the concentration of hydrogen molecules in the initial mixtures increases, the quantity of the hcp$_2$ phase increases, and the content of the cubic fcc phase decreases linearly. When the temperature of the samples increases, a complete irreversible decomposition of the hcp$_2$ phase into the phases of the initial components occurs near the melting point of the crystals. The latter circumstance attests to the facts that this phase is metastable and its appearance in the condensates is due to the extremely nonequilibrium conditions of crystallization under which the solid mixtures were obtained directly from the gaseous state. For the vacuum condensation method used in the present work, the boundary of single-phase states on the neon side is 2 mol.% H$_2$.

We are deeply grateful to M. I. Bagatskiĭ and B. Ya. Gorodilov for a discussion of the results obtained in this work and for valuable remarks. Partial financial support for this work was provided by the International Science Foundation CRDF (grant UP2-2445-KH-02).

*E-Mail: galtsov@ilt.kharkov.ua

[1)]We underscore that here we are not referring to the equilibrium solubility of H$_2$ in solid neon (or vice versa), because at temperatures near 5 K it should be vanishingly small. The measured quantity is the maximum concentration x_{lim} of the H$_2$ impurity in Ne crystals obtained under definite

quench-condensation conditions for which decomposition does not occur and the neon-rich phase retains ''its individuality.''

[1] E. B. Gordon, L. P. Mezhov-Deglin, and O. F. Pugachev, JETP Lett. **19**, 63 (1974).
[2] E. B. Gordon, V. V. Khmelenko, A. A. Pelmenov, E. A. Popov, and O. F. Pugachev, Chem. Phys. Lett. **155**, 301 (1989).
[3] V. V. Khmelenko, S. I. Kiselev, D. M. Lee, and C. Y. Lee, Physica Scripta T **102**, 118 (2003).
[4] E. B. Gordon, Fiz. Nizk. Temp. **30**, 1009 (2004) [Low Temp. Phys. **30**, 756 (2004)].
[5] M. A. Strzhemechny, N. N. Galtsov, and A. I. Prokhvatilov, Fiz. Nizk. Temp. **29**, 699 (2003) [Low Temp. Phys. **29**, 522 (2003)].
[6] *Cryocrystals*, edited by B. I. Verkin and A. I. Prokhot'ko, Naukova dumka, Kiev (1983).
[7] V. G. Manzhelii, A. I. Prokhvatilov, I. Ya. Minchiina, and L. D. Yantsevich, *Handbook of Binary Solutions of Cryocrystals*, Begell House, New York (1996).
[8] A. S. Baryl'nik, A. I. Prokhvatilov, M. A. Strzemechnyĭ, and G. N. Shcherbakov, Fiz. Nizk. Temp. **19**, 625 (1993) [Low Temp. Phys. **19**, 447 (1993)].
[9] M. I. Bagatskiĭ, I. Ya. Minchina, and V. B. Manzheliĭ, Fiz. Nizk. Temp. **22**, 53 (1996) [Low Temp. Phys. **22**, 37 (1996)].
[10] A. S. Baryl'nik, A. I. Prokhvatilov, and G. I. Shcherbakov, Fiz. Nizk. Temp. **21**, 787 (1995) [Low Temp. Phys. **21**, 607 (1995)].
[11] M. A. Strzhemechny, A. I. Prokhvatilov, G. N. Shcherbakov, and N. N. Galtsov, J. Low Temp. Phys. **115**, 109 (1999).
[12] M. Simon, Phys. Lett. **5**, 319 (1963); Physica **29**, 1079 (1963).
[13] J. P. Brouwer, L. J. Hermans, H. F. P. Knaap, and J. J. Beenakker, Physica **30**, 1409 (1964).
[14] S. Barrett, L. Meyer, and J. Wasserman, J. Chem. Phys. **45**, 834 (1966).
[15] N. G. Bereznyak, A. A. Sheĭnina, and L. V. Karnatsevich, Ukr. Fiz. Zh. **19**, 668 (1974); Fiz. Nizk. Temp. **1**, 780 (1975) [Sov. J. Low Temp. Phys. **1**, 376 (1975)].
[16] B. Ya. Gorodilov, A. I. Krivchikov, V. G. Manzheliĭ, N. N. Zholonko, and O. A. Korolyuk, Fiz. Nizk. Temp. **21**, 723 (1995) [Low Temp. Phys. **21**, 561 (1995)].
[17] P. Loubeyre, R. LeToullec, and J. P. Pinceaux, Phys. Rev. Lett. **67**, 3271 (1991).
[18] P. Loubeyre, R. Letoullec, and J. P. Pinceaux, Phys. Rev. B **45**, 12844 (1992).
[19] *Rare Gas Solids*, edited by M. L. Klein and J. A. Venables, Academic Press, London (1966), Vol. 1 and (1967), Vol. 2.
[20] I. N. Krupskiĭ, A. I. Prokhvatilov, and G. N. Shcherbakov, Fiz. Nizk. Temp. **9**, 858 (1983) [Low Temp. Phys. **9**, 446 (1983)].

Translated by M. E. Alferieff

Observation of charged excimer complexes radiating in the VUV range in Xe–Ne cryoalloys

A. G. Belov, M. A. Bludov, E. A. Bondarenko, Yu. S. Doronin, V. N. Samovarov,* and E. M. Yurtaeva

B. I. Verkin Institute for Low Temperature Physics and Engineering, Ukrainian National Academy of Sciences, pr. Lenina 47, Kharkov 61103, Ukraine
(Submitted April 21, 2004; revised June 7, 2004)
Fiz. Nizk. Temp. **30**, 1315–1320 (December 2004)

Comparative measurements are performed of the cathodoluminescence of Xe–Ne solid alloys and free Xe clusters. A nonelementary band is observed on the low-energy side of the well-known transition in the neutral excimer complex Xe_2^* (7.1 eV). The structure and intensity of this band depend on Xe concentration. It is concluded on the basis of an analysis of the experimental data for cryocrystals and ionized clusters that this new band is a superposition of the luminescence of homo- and heteronuclear charged excimer complexes. It is shown that the neon matrix can serve as an effective reservoir for accumulation of hole centers and localized electrons. © *2004 American Institute of Physics.* [DOI: 10.1063/1.1820041]

1. INTRODUCTION

In connection with the development of high-power excimer lasers, special attention has been devoted since 1980s to the observation and investigation of charged excimer complexes of inert elements in gas discharges.[1] In the last few years studies have been performed of the emission from gas mixtures in cryodischarges cooled almost to the condensation temperature of inert gases.[2] It should be noted that experiments studying excimer complexes in condensed inert media have been performed in parallel for more than 20 yr. These works are devoted primarily to the investigation of neutral excimer complexes (Refs. 3–5 and the references cited there).

At the beginning of the 1990s the VUV emission spectroscopy method was used for the first time to show the existence of charged excited clusters of inert elements, which can be regarded as an ionized cluster containing an ion and an excimer molecule.[6] In Ref. 6 free argon, krypton, and xenon clusters ranging in size from 100 to 10^4 atoms/cluster were ionized and excited by an electron beam. This resulted in the formation of complexes of the type $(R_4^+)^*$, where R is an atom of an inert element, in them. The radiative decay of such complexes greatly expands the spectral range of the radiation of ordinary neutral R_2^* centers. The ionic complexes $(R_3^+)^*$ and $(R_4^+)^*$ in small argon and xenon complexes (30–100 atoms/cluster) have also been observed in experiments on the photoexcitation of cluster beams.[7] The question of whether or not such clusters can form in massive cryocrystals has remained open up to now. For a long time it was believed that it is very difficult to accumulate charge centers in pure defect-free cryocrystals of inert elements, excited above the band gap, because of rapid electron-hole recombination.[8] It is precisely the rapid electron-hole recombination via the formation of excitons that is responsible for the appearance of neutral excimers of the type R_2^* in bulk cryocrystals.

However, if electron traps (structural or impurity) form in the matrix, then, in principle, conditions can be created for stabilizing positively and negatively charged centers. Thus, doping cryocrystals with impurities capable of forming negative ions and serving as traps for electrons is widely used in the ''matrix isolation'' method.[9,10] In Ref. 11 luminescence spectroscopy was used to obtain evidence of electron localization in pure and doped neon at liquid-helium temperature. The existence of long-lived traps for electrons in pure cryocrystals of inert elements was recently established by thermally stimulated exoelectronic emission.[12]

Among cryocrystals neon occupies a special position because of the large band gap ($E_g \approx 21.5$ eV), the lattice lability, and the large high electron affinity, which creates favorable conditions for generation and accumulation of charged centers.

The objective of the present work is to search for charged excimer complexes in solid solutions of inert elements in a neon matrix. Comparative measurements were performed of the cathodoluminescence of cryocrystals based on a Xe–Ne mixture and free xenon clusters, where complexes similar to those indicated above exist. In this work reliable proof of the formation of excited charged complexes in bulk cryocrystals radiating with appreciable intensity in the VUV region is obtained for the first time.

2. EXPERIMENTAL PROCEDURE

Comparative spectral measurements were performed on setups for studying the luminescence of cryocrystals and their solid solutions as well as free clusters.

Cryocrystals consisting of solid binary mixtures Xe–Ne were investigated with Xe concentrations ranging from $C = 0.01\%$ to 30%. The samples were grown by rapid condensation of a gas mixture on a substrate in an optical helium cryostat at $T = 4.5$ K and exposed at the same temperature. Spectrally pure Xe and Ne with total impurity content not exceeding 0.01% were used to prepare the gas mixture. A beam of monoenergetic electrons with energy 400 eV and current density 0.1 mA/cm^2 excited the luminescence. A VMR–2 monochromator and a photon-counting circuit were

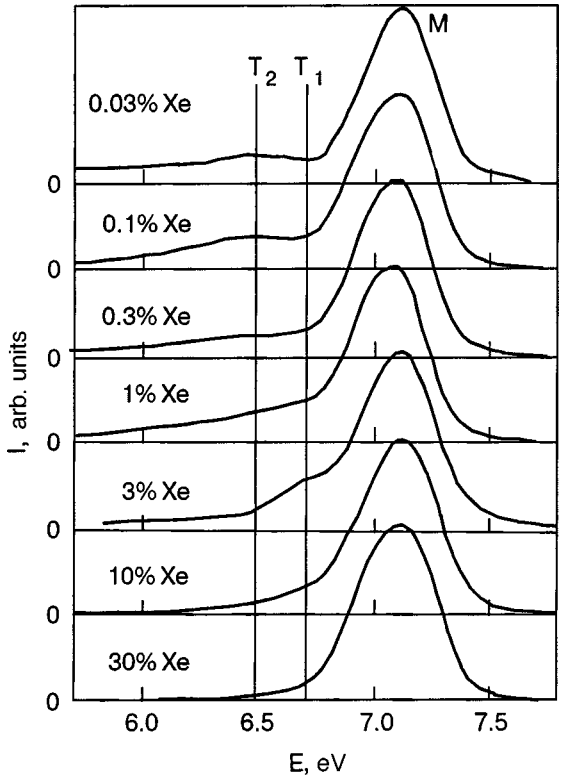

FIG. 1. Intensity distribution in the cathodoluminescence spectra of Xe–Ne cryoalloys for various Xe concentrations. $T=4.2$ K.

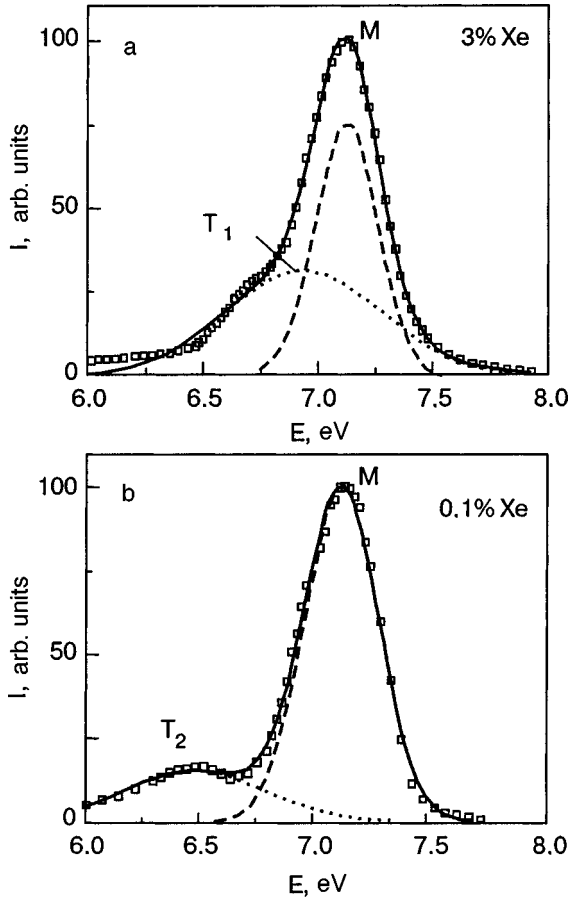

FIG. 2. Decomposition of the measured luminescence spectra (□) into Gaussian components (broken lines). The solid line is the sum of the two components of the decomposition. The Xe concentration in Ne is 3% (a) and 0.1% (b).

used to record the spectra. In addition, the influence of the irradiation dose on the nature of the spectrum under continuous irradiation of the sample by electrons and the afterglow spectra and the decay time of their individual bands were studied.

Free xenon clusters were obtained by homogeneous condensation of the gas flowing out of a supersonic nozzle into vacuum. Clusters ranging in size from $N=100$ to 4×10^4 atoms/cluster were obtained by varying the temperature and gas pressure at the entrance into the nozzle. The temperature of the clusters studied was about 57 K. A beam of 1 keV electrons was used to excite the clusters.

The experimental techniques used for cryocrystals and cluster beams are described in greater detail in Refs. 13 and 14.

3. EXPERIMENTAL RESULTS

The relative distribution of the luminescence intensities of xenon in a neon matrix in the range 6–8 eV are presented in Fig. 1 for several concentrations of the binary mixture. For Xe concentrations from 0.03 to 10% a distinct shoulder is observed on the low-energy side of the M band corresponding to the well-known transition $^{1,3}\Sigma_u^+\rightarrow{}^1\Sigma_g^+$ in the excimeric molecule Xe_2^* ($E_{max}=7.1$ eV). The shape, characteristic width, and position of this shoulder depend on the concentration of the solution. A systematic shift of the maximum point of the shoulder with increasing concentration is observed. This suggests that the observed shoulder is not elementary and consists of at least two components and that the intensities of these components depend oppositely on the Xe concentration. The component with the longest wavelength is characteristic for solutions with low impurity concentration, while the shorter-wavelength component reaches its maximum intensity at concentration $C=3\%$ (Fig. 1). To check this supposition the total spectrum ws decomposed into three components: the M band, corresponding to the transition $^{1,3}\Sigma_u^+\rightarrow{}^1\Sigma_g^+$ in neutral Xe_2^* center, and the bands T_1 and T_2, which form the low-energy shoulder of the M band. The decomposition into M and T_2 (Fig. 2a) and M and T_1 (Fig. 2b) is shown for two strongly different xenon concentrations—0.1 and 3%, for which the relative contribution of one of the T bands is greatest. The decomposition into these three Gaussian bands made it possible to describe satisfactorily the general spectral distribution in the entire concentration range. The maximum of the T_1 band lies at $E_{max}^{T_1}=6.8\pm0.1$ eV and the half-width is $\Delta E^{T_1}=0.7\pm0.1$ eV; the values for the T_2 band are $E_{max}^{T_2}=6.5\pm0.03$ eV and $\Delta E^{T_2}=0.8\pm0.1$ eV.

An investigation of the influence of the irradiation dose on the intensity distribution did not show any substantial features. Only a tendency for the total intensity of the spectrum to decrease was observed.

However, a persistent (up to 1 h and longer) post-irradiation afterglow was observed. This attests to delayed electron-hole recombination. The duration of the afterglow depended on the impurity concentration in the cryoalloy and decreased with increasing xenon concentration. A sum of two

exponentials described the intensity decay curves well: $I = A_1 \exp(-t/\tau_1) + A_2 \exp(-t/\tau_2)$, where $\tau_2 \sim 8.5$ s for all concentrations and τ_1 decreased substantially with increasing concentration from 140 s for $C = 0.3\%$ to 37 s for $C = 30\%$. Generally speaking, the existence of such a persistent impurity afterglow, which is not observed in other inert cryocrystals, in itself attests to low electron mobility, i.e. electron localization in the neon matrix.

The presence of a persistent afterglow made it possible to determine its spectral composition. It was found that the afterglow spectrum contains only the M band. The radiation in the T_1 and T_2 bands is absent from the persistent afterglow spectra. It should be noted that when the sample was heated from 4.5 K after the afterglow vanished thermal luminescence was observed only in the M band; this attests to the existence of quite deep traps for charges of both signs.

In summary, the observation of persistent afterglow and thermal luminescence shows a substantial accumulation of spatially separated and localized (in the volume of the solid alloy) positively charged Xe_2^+ and electrons in the samples during the initial irradiation. The M band is due to the recombination of the these centers. On the other hand, the absence of persistent afterglow in the T_1 and T_2 bands of the spectra shows convincingly that these bands cannot be due to recombination of Xe_2^+ and e^-.

4. DISCUSSION

A comparative analysis of the emission spectra of gaseous and solid Xe–Ne mixtures and also pure xenon clusters in the 6–8 eV range was performed to identify the T_1 and T_2 bands. The emissions from the gaseous and solid (0.1% Xe) Xe–Ne mixtures are compared in Fig. 3a; a similar comparison is made in Fig. 3b for xenon clusters and a solid mixture with 3% Xe. The data for the gas mixtures were taken from Ref. 15. In this work the charged Ne^+ particles were injected from a gas discharge into Xe buffer gas at pressure $P \approx 0.5$ atm. An intense peak was observed on the low-energy side of the M band. This peak was attributed to the emission from triatomic ions Ne^+Xe_2 and is represented in Fig. 3a by the broken curve. The radiative transition into the bottom repulsive ionic state of the complex proceeds according to the scheme[15]

$$Ne^+Xe_2 \rightarrow NeXe_2^+ + h\nu \qquad (1)$$

and results in the appearance of a band at 6.49 eV with half-width 0.34 eV. The quite good agreement between the position and shape of the emission band of the complex Ne^+Xe_2 and the position and shape of the T_2 band makes it possible to attribute the latter to the same transition (1) but in the solid alloy Xe–Ne. The following facts confirm this assertion: 1) the transition (1) in an ionic complex is allowed and has a very short lifetime ($\approx 10^{-9}$ s), and since no change in the charge occurs in the reaction, the transition should precede the recombination process; this is why the T_2 band is absent in the persistent afterglow in our experiment; 2) the maximum of the T_2 band should be reached at Xe concentrations for which the probability of the formation of diatomic complexes Xe_2 in the Ne matrix reaches its highest value; statistical computational methods[16] show that this should occur for concentrations of several percent, which

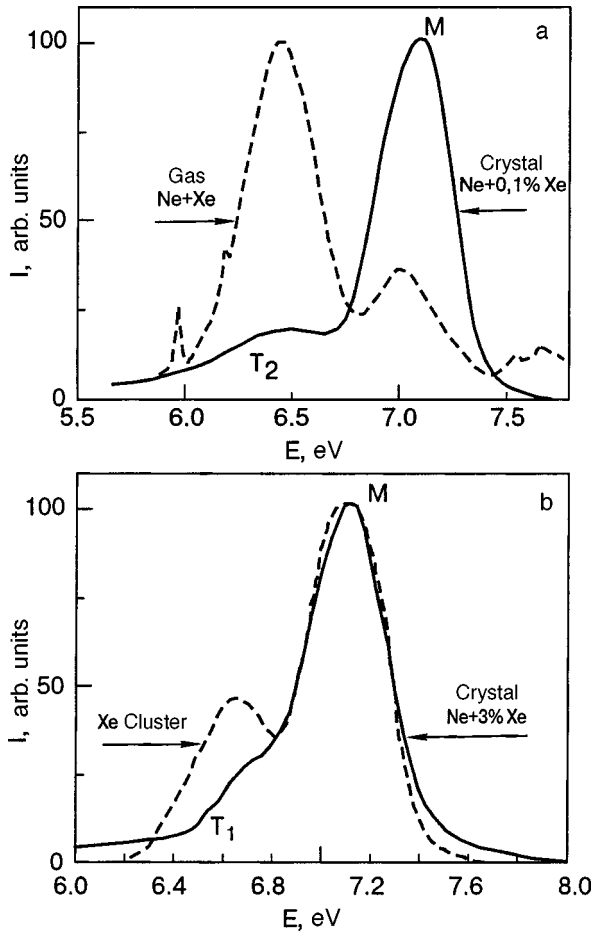

FIG. 3. Comparison of the luminescence spectra of Xe in Ne for various Xe concentrations and the emission spectra of a Xe–Ne gaseous mixture (a) and luminescence spectra of free Xe clusters (b).

corresponds to the maximum intensity of the T_2 band in Fig. 1. We note in this connection that at higher concentrations the formation probability of multiatom impurity complexes in alloys increases and that of diatomic complexes decreases.

We shall now consider the nature of the T_1 band, which, just as the T_2 band, is not observed in the persistent afterglow spectra. The latter indicates that this band likewise is not due to the recombination of localized charge carriers. According to Fig. 3b, for high concentrations $C \approx 3\%$, when the T_2 band is greatly weakened, the T_1 component correlates well with the radiation from xenon clusters with $N > 100$ atoms per cluster. According to the results of Refs. 6, 7, and 14 the observed band for clusters corresponds to radiation from ionized clusters containing charged excimeric complexes. It is worth repeating that the maximum intensity of the T_1 band is observed at concentrations for which impurity centers with $N_i = 3-4$ atoms begin to form in the matrix. This makes it possible to attribute the T_1 band to radiation from excited ionic centers of the type $(Xe_4^+)^*$ and $(Xe_3^+)^*$. An additional argument for attributing the T_1 band to charged centers is that this band is absent in the luminescence of Ne+0.25% Xe crystals with selective photoexcitation by synchrotron radiation photons below the ionization threshold of xenon in a Ne matrix.[17] We also note the following. According to Fig. 1, the intensity of the low-energy shoulder decreases appreciably for xenon concentration

above 10%. The matrix isolation of xenon in neon is already substantially suppressed at concentrations of several percent, and the solution separates.[18] Actually, this situation corresponds to a pure xenon cryocrystal, where holes are localized primarily in the form of diatomic centers. This results in recombination emission in the *M* band. We note also that visible-range radiation from $(Xe_2^+)^*$ (with a maximum near 2.15 eV) is observed in xenon cryocrystals and large xenon clusters.[7,19,20]

5. CONCLUSIONS

In summary, our comparative investigations of the luminescence of solid Xe–Ne cryoalloys and free xenon clusters excited by electrons has revealed in the spectra an appreciable component on the low-energy side of the known *M* band (radiation from the excimeric molecule Xe_2^*). This additional nonelementary band is identified quite reliably as radiation from charged excimeric complexes. This shows that a solid neon matrix can be an effective reservoir for creating and accumulating ionic impurity excimers of the type $(Xe_3^+)^*$, $(Xe_4^+)^*$, and Ne^+Xe_2, which emit in the VUV range. When xenon regions with substantial volume appear in the matrix, the formation of $(Xe_2^+)^*$ centers is found to be favored. On the whole, the observation of multiatom charged excimeric complexes in cryocrystals opens up new approaches to studying the problems of the migration and relaxation of electronic excitations and the formation of high-energy excimeric states. It is also worth noting that questions concerning the accumulation of charges of different sign in inert cryocrystals are closely related with the long-standing but still little studied problem of creating a strongly nonideal ''frozen plasma,'' [21] which should possess many very unusual properties.

In closing, it is our duty to thank E. V. Savchenko and É. T. Verkhovtsevoĭ for a helpful discussion of the results obtained in this work.

*E-Mail: samovarov@ilt.kharkov.ua

[1] N. G. Basov, M. G. Voĭtik, V. S. Zuev, and V. P. Kutakhov, Kvantovaya élektronika **15**, 2204 (1985) [Sov. J. Quantum Electron. **15**, 1455 (1985)].
[2] B. Krylov, G. Gerasimov, A. Morozov, A. Arnesen, R. Hallin, and F. Hejkenskjold, Eur. Phys. J. D **8**, 227 (2000).
[3] I. Ya. Fugol', A. G. Belov, E. V. Savchenko, and Yu. B. Poltoratskiĭ, Fiz. Nizk. Temp. **1**, 203 (1975) [Sov. J. Low Temp. Phys. **1**, 98 (1975)]; E. V. Savchenko, A. N. Ogurtsov, O. N. Grigorashchenko, and S. A. Gubin, Fiz. Nizk. Temp. **22**, 1210 (1996) [Low Temp. Phys. **22**, 926 (1996)]; A. G. Belov, I. Ya. Fugol, E. M. Yurtaeva, and O. V. Bazhan, J. Lumin. **91**, 107 (2000).
[4] M. Kirm, V. Kisand, E. Sombrowcki, B. Steeg, S. Vielhauer, and G. Zimmerer, Fiz. Nizk. Temp. **29**, 1081 (2003) [Low Temp. Phys. **29**, 822 (2003)].
[5] M. Selg and R. Kink, Fiz. Nizk. Temp. **29**, 1130 (2003) [Low Temp. Phys. **29**, 862 (2003)].
[6] E. A. Bondarenko, E. T. Verkhovtseva, Yu. S. Doronin, and A. M. Ratner, Chem. Phys. Lett. **82**, 637 (1991).
[7] R. Müller, M. Joppin, and T. Möller, Z. Phys. **26**, 370 (1993); A. V. Kanaev, M. C. Castex, L. Meseur, R. von Pietrowski, and T. Möller, Phys. Rev. Lett. **75**, 2674 (1995); T. Laarmann, A. Kanaev, K. von Haeften, H. Wabnitz, R. von Pietrowski, and T. Möller, J. Chem. Phys. **16**, 7558 (2002).
[8] N. Schwentner, E. E. Koch, and J. Jortner, *Electronic Excitations in Condensed Rare Gases*, Springer, Berlin (1985).
[9] V. A. Apkarian and N. Schwentner, Chem. Rev. (Washington, D.C.) **99**, 1481 (1999).
[10] V. A. Bondybey, M. Räsänen, and A. Lammers, Annu. Rev. Prog. Chem. Sec. C **95**, 331 (1999).
[11] A. G. Belov, G. M. Gorbulin, I. Ya. Fugol', and E. M. Yutaeva, Fiz. Nizk. Temp. **23**, 439 (1997) [Low Temp. Phys. **23**, 322 (1997)].
[12] O. N. Grigorashchenko, V. V. Rudenkov, I. V. Khizhnyi, E. V. Savchenko, M. Frankowski, A. M. Smith-Gickfhom, and M. K. Beyer, Fiz. Nizk. Temp. **29**, 1147 (2003) [Low Temp. Phys. **29**, 876 (2003)]; E. V. Savchenko, O. N. Grigorashchenko, A. N. Ogurtsov, V. V. Rudenko, G. V. Gumenchuk, M. Lorenz, A. Lammers, and V. E. Bondybey, J. Low Temp. Phys. **122**, 379 (2001).
[13] A. G. Belov, I. Ya. Fugol', and E. M. Yurtaeva, Fiz. Nizk. Temp. **24**, 580 (1998) [Low Temp. Phys. **24**, 440 (1998)].
[14] É. T. Verkhovtseva, E. A. Bondarenko, and Yu. S. Doronin, Fiz. Nizk. Temp. **30**, 47 (2004) [Low Temp. Phys. **30**, 34 (2004)].
[15] N. Tsuji, M. Tanaka, and Y. Nishimura, J. Chem. Phys. **107**, 4852 (1997).
[16] M. M. Kreitmann and D. L. Barnett, J. Chem. Phys. **43**, 364 (1965).
[17] M. Runne, Doctoral Thesis, University of Hamburg, Interner Bericht DESY Hasylab, N 97-4 (1997).
[18] V. G. Manzhelii, A. I. Prohvatilov, I. Ya. Minchina, and L. D. Yantsevich, *Handbook of Binary Solutions of Cryocrystals*, Beden House, New York (1996).
[19] E. V. Savchenko, N. Caspary, A. Lammers, and A. E. Bondybey, J. Low Temp. Phys. **111**, 693 (1998).
[20] A. G. Belov, E. I. Tarasova, and E. M. Yurtaeva, Fiz. Nizk. Temp. **29**, 539 (2003) [Low Temp. Phys. **29**, 401 (2003)].
[21] B. M. Smirnov, Usp. Fiz. Nauk **125**, 331 (1978) [Sov. Phys. Usp. **21**, 522 (1978)]

Translated by M. E. Alferieff

LETTER TO THE EDITOR

Observation of the electric induction due to a second-sound wave in He II

A. S. Rybalko*

B. I. Verkin Institute for Low Temperature Physics and Engineering, Ukrainian National Academy of Sciences, pr. Lenina 47, Kharkov 61103, Ukraine
(Submitted July 29, 2004)
Fiz. Nizk. Temp. **30**, 1321–1325 (December 2004)

It is shown experimentally that the relative motion of the superfluid and normal components of He II in a second-sound wave is accompanied by the appearance of electric induction. The process is reversible. It is shown that the amplitude ratio of the temperature and induction potential oscillations is a temperature-independent constant equal to 2.3×10^4 K/V. © *2004 American Institute of Physics.* [DOI: 10.1063/1.1820042]

1. INTRODUCTION

The question of a possible connection between the macroscopic superfluid motion and electric properties of condensed helium is a virtually unstudied aspect of the physics of superfluid ^{4}He. In the present paper the idea of a possible relationship between the internal electric fields and undamped superfluid flows of liquid helium below T_λ is developed experimentally for the first time.

The hydrodynamics of He II can be described in the two-fluid model by introducing two velocity fields—superfluid motion with velocity V_s and normal motion with velocity V_n. One of the most convenient methods for exciting these motions is to generate a first or second sound. It is well known that in a first-sound wave both components oscillate in-phase ($V_s=V_n$) and in a second-sound wave they move in antiphase, i.e., $V_s=-V_n\rho_n/\rho_s$, where ρ_n and ρ_s are the densities of the corresponding normal and superfluid components of He II. In addition, first sound is a density (pressure) wave and second sound is a temperature wave; they are coupled only through the thermal expansion coefficient, which can be neglected because it is small.

Although first and second sounds have now been investigated in great detail, the question of their influence on the electric properties of He II and, first and foremost, the polarization remains unclear.

One specific property of superfluid helium can be used to study the physics of the processes occurring inside He II. It is well known that when the walls of a vessel are heated counter currents of normal and superfluid components arise in superfluid helium in a direction perpendicular to the wall. In turn, the relative motion of the normal and superfluid components is due to the action of the internal forces in the liquid, which are associated with the kinetics of establishing an equilibrium macroscopic quantum state, on the microscopic level. The distinct direction of the vector of forces makes it possible to ask the following question: Does an electric multipole moment of the liquid arise in this case?

In the present paper the results of the first experiments searching for and studying the electric response induced by second sound in superfluid helium are reported.

2. EXPERIMENTAL PROCEDURE

The experiments with first and second sounds were performed by the resonance method in the temperature range 1.3–4.2 K in two cavities with working lengths 1.05 and 28 mm. The inner walls of the cavities were polished and gilded to decrease the surface losses.

The measurement scheme was conventional: a signal from a generator was fed into a sound generator and the fundamental branch of an amplifier. A lock-in amplifier, double screening of the input circuits, compensation of the input capacitance, and an autonomous power supply for the preamplifier made it possible to achieve voltage sensitivities 3×10^{-9} V in the 1 Hz band.

Piezoceramic sensors served as the first-sound generator and detector. A gold or copper thin-film heater was used to generate second sound. A ruthenium oxide thin-film bolometer with sensitivity 6.7 K^{-1} served as a second-sound detector. The bolometer made it possible to measure confidently the amplitude ΔT of the temperature oscillations, induced by second sound, down to 10^{-6} K.

It is well known that the polarizability is an important electric characteristic of a dielectric. The polarizability can be measured by placing the dielectric between the plates of a flat-plate capacitor. A special feature of the experiments was that the cavity and the capacitor used for measuring the polarizability of He II were combined in one apparatus: the first- and second-sound cavities also functioned as capacitors for detecting electric induction (displacement) in the He II. In the experiments an electrode placed at the location of the bolometer served as one plate of the capacitor and the cavity housing served as the other plate. The magnitude of the induced charge divided by the input capacitance, $\Delta U=\Delta Q/C_{\text{in}}$, determined the potential difference of the capacitor. A gold film, solid brass, and ruthenium oxide were used for the measuring electrode in different experiments.

Thus, changing the sensors at the ends of the cavities made it possible to perform measurements of the sound amplitude and to observe the electric properties according to the magnitude of the charge induced on the electrode.

TABLE I. Characteristics of the series of experiments

Series No.	Sound generator	Sound detector	Quantity recorded	1.05 mm cavity	28 mm cavity
1	heater	bolometer	ΔT	+	+
2	heater	electrode	ΔU	+	
3	capacitor	bolometer	ΔT		+
4	capacitor	electrode	ΔU		+
5	piezoelectric sensor	piezoelectric sensor	ΔP	+	
6	piezoelectric sensor	electrode	ΔU	−	

Note: The measured quantities ΔT and ΔU are, respectively, the amplitude of the temperature oscillations and the amplitude of the oscillations of the potential on the electrode in a second-sound wave, ΔP is the amplitude of the pressure oscillations in a first-sound wave, the + and − signs indicate whether or not the corresponding amplitude is observed in the experiments.

3. EXPERIMENTAL RESULTS

The series of experiments performed with two cavities using different sound generators and detectors are summarized in Table I.

After the liquid helium condensed in the measurement chamber, the cavities were filled through a slit at the top, and the temperature was stabilized, the amplitude–frequency curves of the measurement apparatus were measured for each series of experiments.

1. Figure 1a shows typical resonance curves of the temperature oscillations ΔT which ordinarily appear when second sound propagates in He II (see Table I, series No. 1). The data obtained for the second-sound velocity and absorption (determined from the width of the resonances) agree very well with the published values.[1,2]

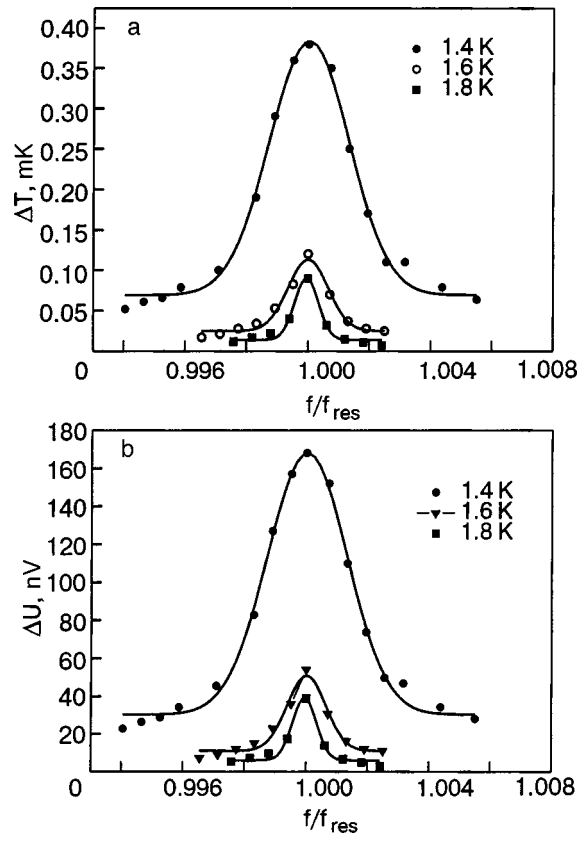

FIG. 1. Amplitude–frequency curves of the second-sound cavity: a) amplitude of the oscillations of the bolometer temperature (series No. 3); b) amplitude of the oscillations of the electric induction potential (series No. 4). Dots—experimental results, solid line—a fit of the Gaussian distribution to the experimental points.

An unusual result was obtained when the bolometer was replaced with an electrode sensitive to electric induction (displacement): sharp resonances of electric induction ΔU (Fig. 1b) appeared at the same frequencies as for ΔT (see Table I, series No. 2). The measurements that we performed above the λ point did not show a signal ΔU. This signal appeared only in the He II region, and the signal amplitude increased as temperature decreased.

To eliminate any possible thermo-emf, due to the Kapitsa thermal resistance, on the receiving electrode the film electrode was replaced with a solid brass electrode (individual experiments in series No. 2). Because of the higher heat capacity the thermal relaxation time was several orders of magnitude greater than f_{res}^{-1}, but the amplitudes ΔU did not change much. This showed unequivocally that there was no thermo-emf.

To perform comparative measurements, in some experiments in series Nos. 3 and 4 the bolometer was used to measure the temperature oscillations ΔT in a second-sound wave and the oscillations of the induced charge $\Delta Q = \Delta U C_{\text{in}}$. For this, it was sufficient to reconnect the output leads of the bolometer in an appropriate manner. In so doing, the opposite walls of the resonator remained parallel and the area of the detectors was the same.

The experiments showed that the electric induction signal is independent of the electrode material. The quality factors are the same for the $\Delta T(f)$ and $\Delta U(f)$ lines and equal to 700–4000 in the experimental temperature range.

Special experiments verified that the signal ΔU is not due to capacitive pickup or vibrations.

Ordinarily, the appearance of an electric displacement of a dielectric signifies that electric multipoles or their polarization are present in the dielectric. For example, electric polarization appears in solids in an electric field E_{ext} or in the presence of mechanical stresses. In our experiments electric induction of He II was observed in the presence of $V_s - V_n$ but with $E_{\text{ext}} = 0$. It is well known that He atoms do not possess a permanent electric moment. Consequently, the result obtained is unexpected.

2. The following experiments were performed to clarify the relation between the internal electric fields and the superfluid flows. An amplifier with a synchronous detector made it

possible to determine the polarity of the induced potential relative to the velocity vector of the superfluid component. It is well known that when an electric current flows through a heater the superfluid component always moves toward the heat source. This fact was used to tie the polarity of the induced potential to the velocity vector $\mathbf{V}_s$. It was found that when the superfluid component moves from the electrode toward the heater a positive charge is induced on the electrode. This became understandable after the phase change of the signal on passing into the measurement circuits and the amplifier channel was taken into account.

3. It was natural to search for the reverse effect — the generation of a second-sound wave as a result of artificial polarization of superfluid helium by an electric field.[1)] To this end the heater in the 28 mm long second-sound cavity was replaced with an electrode–grid capacitor. The grid was connected to the housing. The grid-wire diameter was 3–5 μm after etching, and the grid-wire spacing was 100 μm. When a potential was applied between the electrode and the grid the part of the liquid in a 0.6 mm long gap at the edge of the cavity ($\sim 2\%$ of the total length) became polarized. The presence of the grid, the small transverse cross section (3×1.4 mm), and the long length of the cavity reliably protected the bolometer from capacitive pickup.

It was found that a second-sound wave could be excited under such conditions (series No. 3). Figure 1 shows ΔT and ΔU versus the frequency of the exciting signal. It is evident that ΔT (series No. 3) and ΔU (series No. 4) behave approximately identically.

Measurements of the tangent of the loss angle of the second-sound source, which served as an alternative to the heater, showed that its real power component is too small to excite the cavity.

It was determined that the amplitudes of the alternating potential of the electrode and the temperature oscillations of the bolometer increased as the squared heater current for small values of the current (series Nos. 1 and 2). When the second method is used to excite a second-sound wave the amplitudes are proportional to the magnitude of the electric field (series Nos. 3 and 4).

The cause of the excitation of the wave process — a gradient of the electric field near the grid wires or the field strength in the gap — remained unclear.

4. A series of experiments was performed with ordinary sound to determine the influence of mechanical stresses on the electric properties of superfluid helium. The experiments performed with first sound (series Nos. 5 and 6) using a similar scheme[2)] showed that electric induction does not arise in this case even for high powers applied to the sound generator ($-$ sign, series No. 6).

In summary, the effect appears only when relative motion of the normal and superfluid components in He II is present. The experiments showed that the electric induction and the counter motion of the superfluid and normal components in a second-sound wave are reversible effects.

4. DISCUSSION

Figure 2 shows the relation between the measured values of ΔT and the corresponding values of ΔU under the same conditions: radiation power and temperature. It is natural to consider ΔT to be a characteristic of the thermal energy of the system and ΔU that of the electrical energy. It is evident that their ratio does not depend on temperature and is a constant. The tangent of the slope angle $\tan\alpha = \Delta T/\Delta U$ is 2.3×10^4 K/V to within $\pm 25\%$. We note that this value is close to $2e/k = 2.3188 \times 10^4$ K/V. Here e is the electron charge and k is Boltzmann's constant.

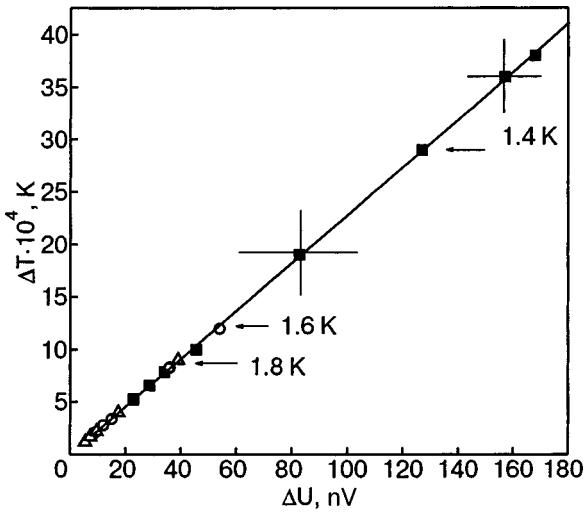

FIG. 2. Relation between the bolometer signal ΔT and the potential signal ΔU of the electric displacement of the cavity with the same power fed to the sound generator which are induced by a second-sound wave for different temperatures. The solid line is drawn through the points. $\tan\alpha = \Delta T/\Delta U = 2.3 \times 10^4$ K/V.

In summary, it has been established in this work that the observed phenomenon is due to the relative motion of the components of He II. The influence of the direction of $V_s - V_n$ relative to the surface on the effect remains unclear.[3)] The observed effect could be a consequence of flows which, according to the two-fluid hydrodynamics,[3] can arise along the surface on which heat is released or absorbed.

A more fundamental reason could be the existence of an as yet undetermined between the superfluid transition and the electric properties of helium. For example, the observed electric displacement and counter currents of the superfluid and normal components are a consequence of, on the one hand, some intra-atomic exchange processes and, on the other hand, ordering in the liquid over macroscopic distances. Two experimental facts support this point of view.

1. The measured dependence of the polarity of the signal induced on the electrode on the direction of V_s indicates that the macroscopic electric dipole formed in the liquid is oriented so that its positively charged end points in the direction of motion of the superfluid component (series Nos. 2 and 4).

2. Second sound in He II can be excited by several methods: thermal,[1] mechanical,[1] and electrical (this work).

It should be noted that at present there is no microscopic theory explaining the appearance of an electric multipole moment in helium atoms when they are in a liquid state below T_λ and relative motion of the superfluid and the normal component is present.

5. CONCLUSIONS

The experiments performed in this work have shown that the relative motion of the superfluid and normal components of He II in a second-sound wave is accompanied by the appearance of electric induction and that this process is reversible. Additional experiments and a corresponding theory are required to clarify the mechanisms which are responsible for the observed effects.

In closing, I thank V. N. Grigor'ev, A. M. Kosevich, É. Ya. Rudavskoĭ, and A. A. Slutskin for a discussion of the results.

*E-mail: rybalko@ilt.kharkov.ua

[1)]A. M. Kosevich pointed out that the effect could be reversible.
[2)]É. Ya. Rudavskoĭ suggested the experiment with first sound.
[3)]Professor V. N. Grigor'ev advanced this interesting suggestion.

[1] V. P. Peshkov, Zh. Eksp. Teor. Fiz. **18**, 857 (1948); **18**, 867 (1948).
[2] K. N. Zinov'ev, Zh. Eksp. Teor. Fiz. **25**, 235 (1953).
[3] L. D. Landau and E. M. Lifshitz, *Fluid Mechanics*, Pergamon Press, New York (1987) [Russian original, Nauka, Moscow (1986)].

Translated by M. E. Alferieff